

Master of Science Thesis

Investigation of the Effect of a Surface Protuberance on a High Speed Boundary Layer

Deepak Prem Ramaswamy

December 11, 2017

Investigation of the Effect of a Surface Protuberance on a High Speed Boundary Layer

Master of Science Thesis

For obtaining the degree of Master of Science in Aerospace Engineering
at Delft University of Technology

Deepak Prem Ramaswamy

December 11, 2017

An electronic version of this thesis is available at <http://repository.tudelft.nl>

Faculty of Aerospace Engineering · Delft University of Technology



Delft University of Technology

Copyright © Aerospace Engineering, Delft University of Technology
All rights reserved.

Cover Image : A cylindrical roughness element placed in the ST-15 test section with the Schlieren setup in the background.

DELFT UNIVERSITY OF TECHNOLOGY
DEPARTMENT OF AERODYNAMICS

The undersigned hereby certify that they have read and recommend to the Faculty of Aerospace Engineering for acceptance the thesis entitled **“Investigation of the Effect of a Surface Protuberance on a High Speed Boundary Layer”** by **Deepak Prem Ramaswamy** in fulfillment of the requirements for the degree of **Master of Science**.

Dated: December 11, 2017

Assessment committee:

Dr.ir. F.F.J. Schrijer

Dr.ir. B.W. van Oudheusden

Dr. F. Avallone

Preface

This thesis marks the end of my MSc life in TU Delft, which has been nothing but a roller-coaster. During the last two years, there were several moments of immense gratification and a sense of accomplishment. There were also some tough times during which I had the support and help of some great people. I would like to take this opportunity to acknowledge those, without whom this work would be far from complete.

Firstly, I would like to thank my family, especially my parents. The person I am today is a culmination of your constant and continuous support and love. I would also like to thank my supervisor Dr.ir. Ferry Schrijer for his support, encouragement and the friendly attitude throughout the length of my MSc study. Special mention goes to Nico van Beek, Peter Duyndam, Dennis Bruikman and Stefan Bernardy for their help during the time I spent in the laboratory. I would like to thank Nick for his help during the experimental campaign in ST-15 and Dr Avallone for letting me use the QIRT data from HTFD. I would also like to thank Dr.ir. Bas van Oudheusden, who, despite not being my direct supervisor, was always available for any quick questions.

I extend my sincere gratitude to my colleagues in the basement at the high speed lab for the all the engaging conversations and lunch time talk. Finally, life in Netherlands would not have been pleasant, if not for the wonderful people like Yeshwanth, Greeshma, Satya, Naina, Manju, Arun, Ram, Vishal, Dutta, Shubham, and numerous others who were like family away from home. Thank you for always being there for me.

Deepak Prem Ramaswamy
Delft, The Netherlands
December 11, 2017.

Table of Contents

Preface	v
List of Figures	xi
List of Tables	xvii
List of Symbols	xix
Summary	xxiii
1 Introduction	1
1.1 Background and Relevance	1
1.2 Thesis Scope and Outline	3
2 Flow Organisation around Isolated Protuberances	5
2.1 Boundary Layer Theory	5
2.1.1 Flat Plate Boundary Layer	5
2.2 Incoming Laminar Boundary Layer	7
2.2.1 Flow Separation	7
2.2.2 Boundary Layer Transition	11
2.3 Incoming Turbulent boundary layer	17

2.4	Research Aim and Objective	20
3	Experimental Methods	23
3.1	Schlieren Visualization	23
3.2	Oil Flow Visualisation	25
3.3	Infrared Thermography	26
3.3.1	Black Body Radiation	26
3.3.2	Radiation of Real Bodies	27
3.3.3	Atmospheric Transmittance	29
3.3.4	Infrared Camera	30
3.3.5	Calibration Procedure	32
3.4	Image Resection and Direct Linear Transformation	36
I	Effect of a Surface Protuberance in an Incoming Laminar Boundary Layer	39
4	Experimental Setup and Data Reduction Technique	41
4.1	The Hypersonic Test Facility Delft (HTFD)	41
4.1.1	Operating Principle	41
4.1.2	Tandem Nozzle	44
4.1.3	Free stream assessment and operation envelope	45
4.2	Wind Tunnel Model	46
4.3	QIRT Data Reduction	50
4.3.1	1D - Semi Infinite Model	51
4.3.2	Cook and Felderman Technique	52
4.3.3	Heat Flux normalisation	53
4.4	Experimental Configuration	54
4.5	Error Sources	55
5	Results and Discussions	57

5.1	Undisturbed Boundary Layer	57
5.2	Interpretation of Heat Transfer Topology	58
5.3	Centreline Stanton number Distribution	60
5.4	2D Heat Transfer Distribution	62
5.5	Upstream Separation Region	67
II Effect of a Surface Protuberance in an Incoming Turbulent Boundary Layer		73
6	Experimental Design	75
6.1	ST-15 Supersonic Windtunnel	75
6.2	Roughness Geometries	77
6.3	QIRT Test Setup	78
6.4	Heat Flux Data Reduction	82
6.4.1	Steady State Heat Transfer	83
6.4.2	Image Preprocessing	84
6.4.3	Non Uniformity Heating Correction (NUHC)	84
6.4.4	Transient Temperature analysis	87
6.4.5	Heat flux computation	88
6.4.6	Heat flux Normalisation	90
6.4.7	Uncertainty Analysis	91
6.5	Schlieren Setup	92
6.5.1	Shock Position Detection	93
7	Shock Unsteadiness and Surface Heat Transfer	97
7.1	Undisturbed boundary layer	97
7.2	Global Flow Features	99
7.3	Surface Heat transfer	100
7.3.1	Centreline Stanton number variation	101

7.3.2	2D Heat transfer Distribution	102
7.4	Upstream Unsteadiness	106
III	Conclusion	111
8	Conclusion and Recommendation	113
8.1	Effect of a Surface Protuberance in an Incoming Laminar Boundary Layer	113
8.2	Effect of a Surface Protuberance in an Incoming Turbulent Boundary Layer . . .	115
8.3	Scope for Future work	116
	Bibliography	117
A	Reference Temperature Method	125
B	Spectral Analysis	129

List of Figures

1.1	Aerodynamic heating of M-2 Lifting Body model tested at the Atmospheric Entry Simulator at NASA's Ames Research Center (Image reproduced from NASA gallery)	1
1.2	Protruding gap fillers on the orbiter during the STS-114 mission (Source: NASA Image ISS011-E-11074)	2
1.3	2D Surface Temperature map of Space Shuttle Discovery (STS-128) during re-entry, travelling at Mach 14.7 (Horvath et al., 2010)	3
2.1	Boundary Layer over a flat plate (redrawn from Anderson Jr (2010))	6
2.2	Schematic of flow separation due to a Forward Facing Step (Image reprinted from Kumar et al. (2014))	7
2.3	Flow-field near short and tall Protuberance (Kumar and Reddy, 2014)	8
2.4	Instantaneous snapshot of flow over a hemispherical bump at Mach 3.37. The stream-wise and span-wise planes show the density gradients portraying the complex 3D separation behaviour (Iyer and Mahesh, 2013)	9
2.5	Stream-wise and Span-wise planes showing the horse-shoe vortex system (Subbareddy et al., 2014)	9
2.6	Schlieren images of a 3D protuberance in an incoming laminar boundary layer at $M_\infty = 8.2$ and $Re_\infty/m = 9.35 \times 10^6$ for deflection angles of (a) $\alpha = 15^\circ$, (b) $\alpha = 30^\circ$, (c) $\alpha = 45^\circ$, (d) $\alpha = 60^\circ$, (e) $\alpha = 90^\circ$ and (f) $\alpha = 135^\circ$ (Estruch-Samper et al., 2010).	10
2.7	Mean velocity profile upstream of a cylindrical protuberance showing the system of vortices upstream (Top), Centreline Stanton number variation showing the heat transfer peak upstream (Bottom Left) and comparison of surface Stanton number variation with the centreline mean velocity profile showing the peak Stanton number occurring due to local central down wash (Bottom Right) (Avallone et al., 2016a).	11
2.8	Laminar to Turbulent boundary layer transition (redrawn from Masutti (2013))	11

2.9	A Roadmap for transition from Laminar to Turbulence (redrawn from Reshotko (2008))	12
2.10	Critical and Effective height of roughness elements (van Driest and McCauley, 1960)	13
2.11	Perturbation of the separated shear layer in Mach 3.37 flow (Iyer and Mahesh, 2013)	14
2.12	Isosurfaces of streamwise vorticity (clockwise rotation is represented by blue and anticlockwise in red) (Avallone et al., 2014)	15
2.13	Centreline Stanton number variation (Avallone et al., 2016b)	16
2.14	A Schlieren image showing the λ - shock system upstream of an asymptotic cylinder (Lash et al., 2016)	17
2.15	Fluctuation pressures at various points in the vicinity of the separation point upstream of a forward facing step (Kistler, 1964).	18
2.16	Instantaneous NPLS images showing the fine turbulent structures (Gang et al., 2016)	18
2.17	Convective heat transfer at different sweep back angles (Yu et al., 2012)	19
3.1	Schematics of a Z - type Schlieren system (Settles, 2001)	24
3.2	Oil flow pattern at Tunnel ON (left) and Tunnel OFF (right) conditions	25
3.3	Spectral hemispherical emissive power ($E_{b,\lambda}$) as a function of λ for different absolute temperatures (Kreith and Manglik, 2016)	27
3.4	Energy reflection, transmission and absorption by a real body (Astarita and Carlomagno, 2013)	28
3.5	Directional emissivity of dielectric and non-metallic materials (Schmidt and Eckert, 1935)	28
3.6	Atmospheric Transmissivity at different wavelengths. Measurements taken at 1 atm, 298.15K and at 25% humidity at a distance of 30m (Mayer, 1996)	29
3.7	Components of an IR acquisition system (Astarita and Carlomagno, 2013)	30
3.8	Cedip IR Camera	31
3.9	Radiation detected by the camera (Astarita and Carlomagno, 2013)	32
3.10	Layout of the Black body simulator (Schrijer, 2010)	34
3.11	Setup of the calibration procedure (Voogt, 2017)	34
3.12	QIRT Calibration Curves corresponding to HTFD (left (Avallone, 2015)) and ST15 (right) campaigns	35

3.13	Error in Temperature estimates due fluctuations in ambient conditions	36
3.14	Object and Image coordinate system (Goktepe and Kocaman, 2010)	37
3.15	Calibration target before (left) and after (right) the application of Direct Linear Transformation	38
4.1	The Hypersonic Test Facility Delft (redrawn from Schrijer and Bannink (2010)) .	42
4.2	Operating Principle of the HTFD (redrawn from Schrijer and Bannink (2010)) .	42
4.3	HTFD Tandem nozzle configuration (redrawn from Schrijer and Bannink (2010))	44
4.4	Vertical velocity components in the free-stream of Mach 7 configuration. The circle portray the outline of the optical access(redrawn from Schrijer and Bannink (2010))	45
4.5	5° ramp model (Avallone et al., 2016b)	47
4.6	Geometry of the Roughness elements	47
4.7	Definition of coordinate system	48
4.8	Boundary Layer profile calculated using Illingworth Transformation	48
4.9	Temperature map (left) and span wise Stanton number variation on the black line calculated using different data reduction procedures (Avallone et al., 2015) . . .	50
4.10	1D semi-infinite model (Schrijer, 2010)	51
4.11	Validation of Cook and Felderman (1966) script	53
4.12	HTFD Experimental Setup (Avallone et al., 2016b)	54
4.13	Transient Temperature response during a typical wind tunnel run	54
5.1	Undisturbed Boundary Layer corresponding to $Re = 8 \times 10^6 m^{-1}$ (Top left) $Re = 11 \times 10^6 m^{-1}$ (Top right) and $Re = 14 \times 10^6 m^{-1}$ (bottom)	58
5.2	Nomenclature of vortices adopted from Iyer and Mahesh (2013). SP - Symmetry plate; OSP - off - symmetry plane	59
5.3	2D Stanton number distribution for R14 D8 case showing the high heat flux due to upstream vortices (1), High heat flux due to central down wash (2), OSP vortex interactions (3), near uniform high heat flux region in the far wake (4). Flow is from left to right	60

5.4	Centreline Stanton number profile corresponding to $Re = 8 \times 10^6 m^{-1}$ (Top left) $Re = 11 \times 10^6 m^{-1}$ (Top right) and $Re = 14 \times 10^6 m^{-1}$ (bottom left) for all the roughness geometries	61
5.5	2D Stanton Number distribution corresponding to D4 (left) and D5.7 (right) cases for all the three Reynolds number. Cases (a,d), (b,e) and (c,f) correspond to a unit Re of $8 \times 10^6 m^{-1}$, $11 \times 10^6 m^{-1}$, $14 \times 10^6 m^{-1}$ respectively	63
5.6	2D Stanton Number distribution corresponding to D8 (left) and D11.2 (right) cases for all the three Reynolds number. Cases (a,d), (b,e) and (c,f) correspond to a unit Re of $8 \times 10^6 m^{-1}$, $11 \times 10^6 m^{-1}$, $14 \times 10^6 m^{-1}$ respectively	64
5.7	Spanwise variation of heat flux at $x^* = 10$ for D4, D5.7 (left) and D8, D11.2 (right) cases at unit $Re = 14 \times 10^6 m^{-1}$	65
5.8	Span wise variation of heat flux at $x^* = 10$ for D4 (left) and D8 (right) cases at two unit Reynolds number	65
5.9	Heat flux perturbation amplitude for all elements corresponding to $Re = 8 \times 10^6 m^{-1}$ (Top left) $Re = 11 \times 10^6 m^{-1}$ (Top right) and $Re = 14 \times 10^6 m^{-1}$ (bottom)	66
5.10	A 4 vortex system by D5.7 Cylinder at $Re = 8 \times 10^6 m^{-1}$ (left) and a 6 vortex system by D8 Cylinder at $Re = 14 \times 10^6 m^{-1}$ (right). Both span wise variations are plotted 3 diameters downstream of the cylinders	68
5.11	Peak heating and upstream separation region of D8 cylinder at $Re = 14 \times 10^6 m^{-1}$	69
5.12	Variation of upstream separation length	69
5.13	Empirical correlation predicting the upstream separation distance	70
6.1	ST-15 Supersonic Wind tunnel - Schematic (top) and a view (bottom left). The picture on the bottom right shows the Mach 2.0 nozzle and the test section (redrawn from Sun (2014))	76
6.2	Roughness elements used in the Investigation of Turbulent interactions	77
6.3	Printed Circuit board design showing the copper track arrangement (redrawn from Voogt (2017))	79
6.4	Makrolon [®] insulation slab (redrawn from Voogt (2017))	80
6.5	Cavity door outside (left) and inside (right) views (redrawn from Voogt (2017))	80
6.6	Schematic of QIRT Test Setup (Top View)	81
6.7	QIRT Test Setup in ST-15	82
6.8	Schematics of steady state heat transfer problem	83

6.9	Frames before (left) and after (right) the application of Image Preprocessing Routine	84
6.10	Non-uniform heating correction corresponding to $I = 0.7A$ (Top Left) and $I = 0.85A$ (Top Right) along with the spacial variance	86
6.11	Transient temperature response at different locations on the PCB (left) and extraction of steady state frames (right)	87
6.12	Sketch of the PCB (Voogt, 2017)	89
6.13	Schlieren setup in ST-15 showing the camera and knife edge (left) and a view through the test section with the light source in the background (right)	92
6.14	Image Processing Routine for Shock Detection	94
6.15	Processed Schlieren image (left) and the corresponding binary image (right) . . .	95
6.16	Sample position plot of the upstream separation region	95
7.1	Flat plate Undisturbed Boundary Layer	97
7.2	Flat plate Undisturbed Boundary Layer	98
7.3	Global flow features for H10 D15 Cylinder. Images are from Schlieren (Top) and Oil Flow visualisation (Bottom). Flow is from left to right.	99
7.4	Centreline heat transfer variation for H6 (Top left), H8 (Top Right) and H10 (Bottom) Cylinders	101
7.5	2D Heat flux distribution around H6 cylinder for diameters D1125 (Top left) and D15 (Top right) and D17 (bottom)	103
7.6	2D Heat flux distribution around H8 cylinder for diameters D15 (left) and D17 (right)	103
7.7	2D heat flux distribution around H10 D17 cylinder	103
7.8	Spanwise distribution of heat flux at different stream wise location for H10 D17 cylinder	104
7.9	Effect of height on Span wise heat flux distribution. Plots correspond to $x^* = 3$ (left) and $x^* = 7.5$ (right)	105
7.10	Schematics of the expected stream wise vortices in the wake. Red arrows denote the down wash and the blue arrows denote up-wash.	105
7.11	Upstream separation length for D17 cylinders	106
7.12	Probability density function of the upstream separation length for D17 cylinders .	107

7.13	Definition of the upstream separation region in heat transfer profile (top), Oil flow visualisation (bottom left) and Schlieren (bottom right)	108
7.14	Variation of upstream separation distance	108
7.15	Standard deviation of the oscillating shock. Dash lines shows the asymptotic case of Lash et al. (2016)	109
B.1	Power spectral density of Shock oscillations upstrem of H10 D17 cylinder	129

List of Tables

3.1	Technical Specification of IR Camera and Lens system	32
4.1	Error in Free stream quantities when $\gamma = 1.4$ (Schrijer and Bannink, 2010)	44
4.2	Free stream quantities for a Mach 7 configuration	46
4.3	Experimental Condition and Laminar Boundary Layer Properties	49
4.4	Roughness Element Geometry	49
6.1	Free stream and Boundary layer properties from the measurements of Giepmans et al. (2014)	76
6.2	Roughness element and Test characteristics	77
6.3	Detail of Schlieren Measurement Campaign	93
7.1	Comparison of mean undisturbed boundary layer Stanton number	98

List of Symbols

Abbreviations

BPR	Bad pixel replacement
CMOS	Complementary metaloxide semiconductor
DLT	Direct Linear Transformation
FOV	Field of view
HTFD	Hypersonic Test Facility Delft
IR	Infrared
LWB	Long Wave Band
MCT	Mercury Cadmium Telluride
NASA	National Aeronautics and Space Administration
NETD	Noise Equivalent Temperature Difference
NS	Navier-Stokes
NUC	Non-uniformity corrections
NUHC	Non-uniformity heating corrections
OSP	Off symmetry plane
PCB	Printed circuit board
PDF	Probability density function
PIV	Particle image velocimetry
QIRT	Quantitative Infrared Thermography
SP	Symmetry plane
SWB	Short Wave Band
T-S	Tollmien-Schlichting
TPS	Thermal Protection System

Greek Symbols

α	Thermal diffusivity
----------	---------------------

α_r	Absorptivity coefficient
δ	Velocity boundary layer thickness
δ^*	Displacement thickness
δ_T	Thermal boundary layer thickness
ϵ	Spectral emissivity coefficient for a grey body
ϵ_λ	Spectral emissivity coefficient
γ	Specific heat ratio
κ	Gladstone-Dale constant
λ	Wavelength of electromagnetic radiation
ρ	Density of the medium
ρ_r	Reflectivity coefficient
ρ_{cu}	Resistivity of copper
σ	Standard deviation
τ_r	Transmissivity coefficient

Other

a	Speed of sound based on the local conditions
c	Speed of light in the medium
C_h	Modified Stanton number
c_p	Specific heat at constant pressure
c_v	Speed of light in vacuum
D	Diameter of the protuberance
E_λ	Spectral hemispherical emissive power of a real body
$E_{b,\lambda}$	Spectral hemispherical emissive power of black body
H	Height of the protuberance
h	Convection heat transfer coefficient
h_{tp}	Height of the triple point
I	Current
IU	Digital output of Infra-red Camera
k	Thermal conductivity
L	Length of the storage tube of the HTFD
L_{sep}	Upstream separation region
n	Refractive index of a medium
p	Static pressure
P_0	Total pressure
Pr	Prandtl number
q_s	Surface heat flux

Re	Reynolds number
s_{cu}	Copper track spacing
St	Stanton number
T	Temperature
T_b	Temperature of black body
T_0	Total temperature
T_{aw}	Adiabatic wall temperature
t_{cu}	Copper track thickness
t_{test}	HTFD running time
u	Streamwise velocity
w_{cu}	Width of the copper tracks
(x,y,z)	Cartesian coordinate system

Subscripts

∞	Free-Stream conditions
e	Boundary layer edge conditions
w	Wall conditions

Summary

One of the major challenges that engineers face when designing a high speed vehicle is aerodynamics heating. While ideally the external surfaces are expected to maintain a smooth profile, this is not the case in most vehicles, which might be laden with discontinuities like steps, gaps, and other protrusions. These could alter the local flow field and could have a drastic impact on the heating and hence should be properly studied. In this thesis, the effect of large protuberances, when placed in both a laminar and turbulent boundary layer is experimentally investigated. In a laminar boundary layer, a protuberance could induce transition and also causes a large separation region with a peak heating upstream. While in a turbulent boundary layer, a protuberance could cause a highly unsteady shock wave boundary layer interactions. Cylindrical elements with height greater than or equal to the boundary layer height, placed on a flat plate were used as protuberances. Quantitative Infrared Thermography was used as the prime investigative tool, assisted by high speed Schlieren and oil flow visualisations.

For the laminar interactions, a series of high and low heat flux regions were observed in the wake of the protuberance due to the presence of stream wise vortices. A local peak due to flow reattachment was found downstream of the cylinder along the centreline, whose length from the cylinder trailing edge scaled with the height of the cylinder and was nearly invariant with the diameter and the flow unit Reynolds number. The span wise distribution of Stanton number revealed that the location of heat flux peak formed due to the symmetry plane counter rotating vortices, scaled with the diameter of the cylinder with their peak heating increasing with increasing in diameter. This revealed the possible dependency of the strength and location of the symmetry plane vortex pair with the diameter of the protuberance. The flow transition induced by the elements considered here, which was detected by identifying the turbulent wedge, moved upstream with increase in unit Reynolds number. Moving upstream, a presence of span wise vortex system was verified. A mean separation length was measured from the centreline heat transfer profiles and an empirical formulation was presented and shown to have good agreement with the current dataset along with recent literature.

For the turbulent interaction, direct heat transfer measurements were acquired downstream of the protuberance for the first time. A centreline high heat transfer was observed, with heating of 1.5 – 2 times the local turbulent case. A series of high and low heat flux regions were observed in the wake, dictating the possible presence of stream wise vortices. Similar to the laminar case, the location of reattachment heating was shown to scale with the height of

the cylinder. Additionally, span wise heat transfer profiles show that the wake width increases with increase in height, while remaining fairly constant for a given condition, throughout the length of the measurement domain. Time resolved Schlieren images captured upstream of the protuberance showed a very unsteady separation shock and a relatively steady bow shock wake, together forming the lambda shock system. Probability density functions generated for the upstream separation length revealed that both the mean and the standard deviation of the separation length increases with increase in height of the cylinder.

Chapter 1

Introduction

1.1 Background and Relevance

From the first powered flight of the Wright Flyer, to the famous Lockheed SR-71 Blackbird, there has been a constant thrust for air planes to achieve faster velocities, leading to its exponential growth. The current record for fastest velocity within the atmosphere is held by the NASA X43-A experimental aircraft, with a velocity of 10,617 km/hr (Mach 9.6) (Tartabini et al., 2006). However, one of the challenges that the vehicle needs to overcome when travelling at these velocities is aerodynamic heating.



Figure 1.1: Aerodynamic heating of M-2 Lifting Body model tested at the Atmospheric Entry Simulator at NASA's Ames Research Center (Image reproduced from NASA gallery)

High speed vehicles and re-entry crafts take special precautions to protect them from the adverse effects of the sustained high temperature loads. When cruising at twice the speed of sound, the Concorde is heated to a maximum of about $393K$ (Doyle, 1969) and hence a cooling system had to be devised to maintain a pleasant environment inside the vehicle. This effect only becomes severe for re-entry vehicles which would disintegrate in the atmosphere if not for their thermal protection system (TPS).

Ideally, high speed vehicles are expected to maintain a smooth outer profile. However, in reality, the surface of the vehicles are laden with discontinuities like rivets, cables and other localised imperfections which affects the state of the boundary layer in the immediate vicinity. Thus proper understanding of the effect of such surface discontinuities is essential to estimate the severity of the consequences.

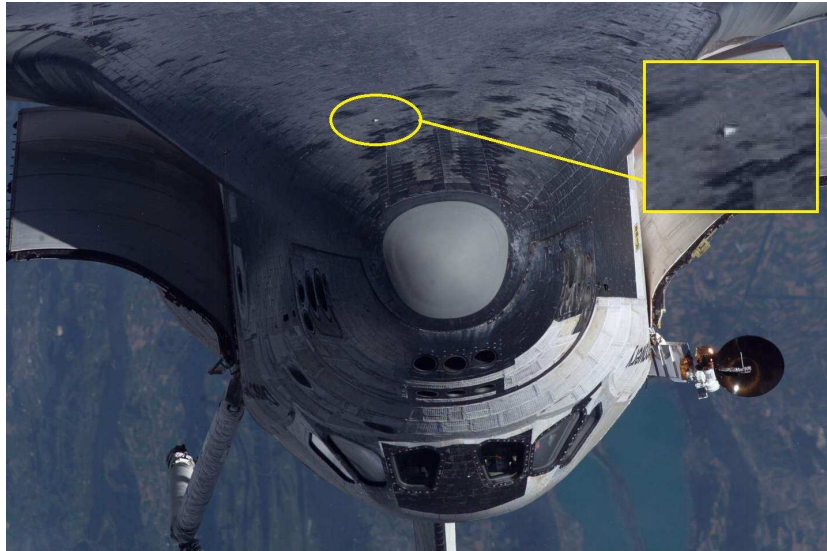


Figure 1.2: Protruding gap fillers on the orbiter during the STS-114 mission (Source: NASA Image ISS011-E-11074)

The importance of understanding the consequences was highlighted during the space shuttle mission STS-114. During its approach to the International Space Station, on July of 2005, NASA Science Officer and Flight Engineer John Phillips took a picture of the Shuttle Discovery as it performed a back flip, an usual manoeuvre carried out to enable assessment of the shuttle's heat shield. Later analysis of the pictures revealed that a gap filler had become dislodged during the ascend phase and is now protruding out of the surface (see Fig.1.2). The exact consequence of this protrusion on the aerodynamic and heat loads during re-entry were unclear at that time and hence it was decided to conduct a space-walk to remove the gap filler. Had there been better understanding of the the precise effect of such a protuberance on the boundary layer, this space-walk could have been avoided (Wheaton and Schneider, 2012).

The relevance of understanding the effects of a surface protuberance or a roughness is not only limited to re-entry vehicles. In high speed air-breathing vehicles like NASA's X-43 (Hyper-X), to prevent unwanted flow separation in the intake of the scramjet, a turbulent flow is desired, which is typically ensured by forcing transition using boundary layer trips (Berry et al., 2001). However, laminar to turbulent transition has a significant impact. The heat flux associated with a turbulent boundary layer could be nearly three times as high as a similar laminar boundary layer (Anderson Jr, 2006). So, to prevent unwanted heating due to early transition, accurate control of transition and hence precise knowledge of the mechanism of forced transition induced by the boundary layer trips is essential. This can also be extended to re-entry vehicles where the accurate estimation of the state of boundary layer could have a drastic impact on the design of the thermal protection system.

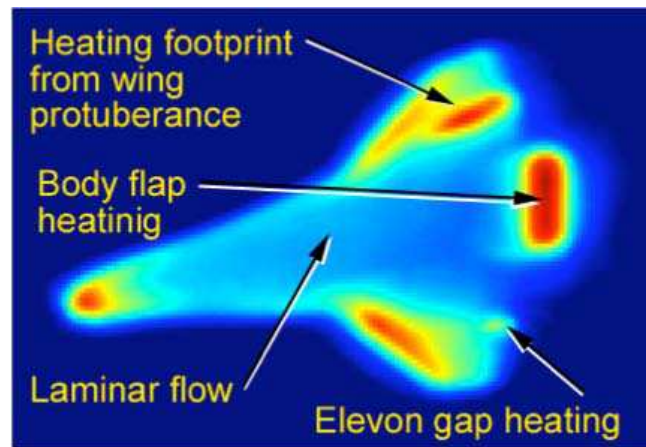


Figure 1.3: 2D Surface Temperature map of Space Shuttle Discovery (STS-128) during re-entry, travelling at Mach 14.7 (Horvath et al., 2010)

The impact of surface roughness on the state of the boundary layer can be observed directly from in-flight temperature measurements of Horvath et al. (2010). They conducted quantitative thermal imaging of the Space Shuttle orbiters during its re-entry into the atmosphere to obtain a unique in-flight global temperature distribution on the windward side of the Shuttle at high Mach numbers. On some of those missions, a modified tile with a protuberance was installed onto the port wing to deliberately disturb the incoming flow and study its effect. The increased heat loads on the surface because of the protuberances is visible in Fig.1.3. The high heat loads, if not properly predicted, could result in the damage of the TPS and could potentially lead to structural breakup. Several engineering correlations were developed based on flight data and wind tunnel tests to predict forced boundary layer transition due to surface protuberances. But, due to the limited number of geometrical and flow parameters that were used in the correlation and the lack of physics involved in their development, there is a question of accuracy in predicting transition. This results in a conservative policy of designing an oversized TPS with a strong safety margin, leading to additional vehicle mass and reduced performance (Tirtey et al., 2011).

1.2 Thesis Scope and Outline

Owing to the reasons stated in the previous section, investigating the effect of a surface protuberance on the high speed boundary layer forms the prime focus of this thesis project. This study aims to improve the understanding of influence of geometry and flow parameters on the surface heat transfer profiles. The investigation carried out is split into two parts, respectively for interaction of a surface protuberance with an incoming laminar and an incoming turbulent boundary layer. While the initial plan was to focus primarily on the interactions in an incoming laminar boundary layer, this research plan was modified owing to the unexpected technical problem with the Hypersonic test facility, rendering it inoperable. Quantitative Infra-red Thermography (QIRT) forms the primary tool for the investigation carried out in this thesis, assisted by Schlieren and Oil flow visualisations.

It has to be highlighted here that, in general, a roughness on the surface of a vehicle can be

classified into two types. If the roughness is spread across the surface of the vehicle, it can be termed as a *distributed* roughness. On the other hand, if the surface roughness is isolated, like steps, gaps, protrusions and other localised imperfections in an otherwise smooth surface, it can be termed as an *isolated* or *discrete* surface roughness. The scope of this thesis is limited to such isolated surface roughness/protuberances and its impact on the convective heat transfer. A brief outline of the the thesis is as follows.

Since the investigations were carried out in two parts, respectively for interactions in an incoming laminar and turbulent boundary layers, the thesis report is also split in two part. Chapter 2 provides a brief description of the fundamentals of boundary layer theory and also discusses some of the most relevant literature pertinent to this study. Following the discussion, the research aims and objectives are also proposed. In Chapter 3 the principle behind the various experimental methods and techniques used in this investigation is discussed in detail. Chapter 4 and 5 together form the first part of the study constituting the interactions in a laminar boundary layer. While Chapter 4 discusses the flow facility and the data reduction technique applicable to this part, Chapter 5 discusses the results of the experiments. Following that, Chapter 6 introduces the test conditions, flow facility and the data reduction technique pertinent to the experiments carried out to investigate the interaction in a turbulent boundary layer. The results of the experiments are discussed in Chapter 7. Together they form the second part of the thesis. Finally, in Chapter 8 the main findings are summarised, along with recommendations for future work.

Chapter 2

Flow Organisation around Isolated Protuberances

In this chapter, an introduction to the boundary layer theory is provided along with an overview of the state-of-the-art literature elaborating the main flow topology around isolated protuberances. While Section 2.2 mainly focuses on literature with a laminar boundary layer inflow, Section 2.3 focuses on the interactions of isolated protuberances with an incoming turbulent boundary layer. Finally, the research aim and objectives are proposed and discussed.

2.1 Boundary Layer Theory

The concept of boundary layer was first introduced by Ludwig Prandtl in 1904. He defined boundary layers to be a thin layer adjacent to the surface of a solid body, where viscosity effects are dominant. Due to the no-slip condition, the velocity of the fluid at the surface of the body is zero. This velocity then increases in the wall normal distance and reaches the freestream velocity at some vertical distance from the wall. This distance is termed as the boundary layer thickness. Since all the experiments were conducted on a flat plate boundary layer, it is discussed in detail in the following section

2.1.1 Flat Plate Boundary Layer

Fig.2.1 shows an illustration of the flat plate boundary layer. As stated earlier, due to the no-slip condition, the velocity adjacent to the surface of the flat plate is zero and increases to match the velocity at the edge of the boundary layer (u_e). A typical velocity profile of the boundary layer is shown and the resulting thickness of the profile, given by the parameter δ is the velocity boundary layer thickness, or just boundary layer thickness. Similarly, the temperature of the fluid adjacent to the flat plate will also be equal to the temperature of the flat plate surface, and is termed as the wall temperature (T_w). This results in a temperature profile in the wall normal direction, until it reaches $T = 0.99T_e$ at particular thickness δ_e . This corresponds to the thermal boundary layer thickness (δ_T). Both the velocity and the

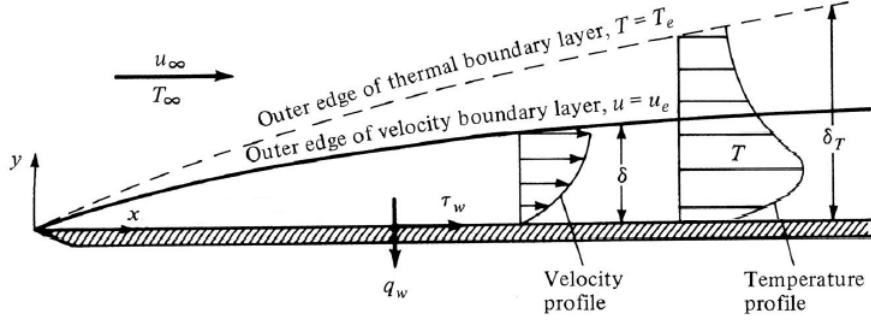


Figure 2.1: Boundary Layer over a flat plate (redrawn from Anderson Jr (2010))

thermal boundary layer increases monotonically, starting from the leading edge of the flat plate, as shown in the figure. The relative thickness depends on the Prandtl number, which is a ratio of the viscous diffusion to thermal diffusion given by Eqn.2.1. At a Prandtl number equal to one, the velocity and the thermal boundary layer thickness will be equal.

$$Pr = \frac{c_p \mu}{k} \quad (2.1)$$

The consequence of the gradients in velocity and temperature at the wall is the presence of surface shear stress (τ_w) and wall heat transfer (q_w), given by the equations:

$$\tau_w = \mu \left(\frac{\partial u}{\partial y} \right)_w \quad q_w = -k \left(\frac{\partial T}{\partial y} \right)_w \quad (2.2)$$

where, μ and k are viscosity and thermal conductivity respectively. Additional integral equations can also be defined, by comparing the boundary layer flow with the inviscid flow near the surface. The displacement thickness, given by Eqn.2.3 represents the vertical displacement that the flow has to undergo to accommodate the low velocity boundary layer flow.

$$\delta^* = \int_0^\delta \left(1 - \frac{\rho u}{\rho_\infty u_\infty} \right) dy \quad (2.3)$$

Similarly, a momentum thickness can be defined, given by Eqn.2.4, which represents the vertical shift that the flow has to undergo to accommodate the momentum deficit caused due to the boundary layer flow.

$$\theta = \int_0^\delta \frac{\rho u}{\rho_\infty u_\infty} \left(1 - \frac{u}{u_\infty} \right) dy \quad (2.4)$$

For an incompressible flow, the Blasius similarity gives an exact solution to the flat plate laminar boundary layer equations and has also been verified by experiments (White, 1991). For the compressible flow, density becomes a variable and hence the Blasius solution with the Illingworth transformation is used to estimate the boundary layer thickness along the flat plate. Detailed derivations of boundary layer governing equations and the application of Illingworth transformation can be found in White (1991). Turbulent boundary layers, once developed is much thicker and disorderly. They are characterised by a higher skin friction

and surface heat flux distribution. While the regime is quite complex to quantify exactly, [van Driest \(1951\)](#) utilised the governing equation to arrive at expressions for skin friction and surface heat flux on a flat plate with a compressible turbulent boundary layer, which are still being used widely. Now that the basic boundary layer properties are revisited, the state of the art literature relevant to the present investigation will be discussed in the rest of this Chapter.

2.2 Incoming Laminar Boundary Layer

In the following two sections, the literature on the effect of protuberance when placed on an incoming laminar boundary layer will be discussed. Generally, the literature on this is divided into two aspects - the upstream separation region and the downstream transition to turbulence. A detailed analysis of the work carried out on both these areas will be presented.

2.2.1 Flow Separation

A flow separation phenomenon is generally detrimental in nature since the surface discontinuity would lead to local non-uniformities in pressure and heat flux on the wall. This is particularly concerning in high speed flows, since the flow separation and re-attachment may lead to potential high heat flux regions and hence may present limitations on the operational envelope of the vehicle. Thus a proper understanding of its effect on the vehicle surface is essential.

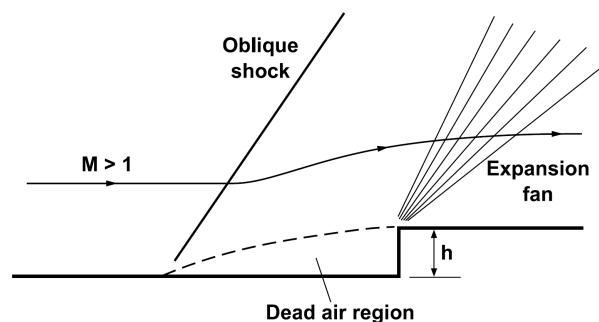


Figure 2.2: Schematic of flow separation due to a Forward Facing Step (Image reprinted from [Kumar et al. \(2014\)](#))

[Lighthill \(1953\)](#) provided a nice description of the separation mechanism in a supersonic flow. When a boundary layer encounters a positive pressure gradient due to, for instance, a surface protrusion, it leads to thickening of the boundary layer. The upward curving of the boundary layer results in a slight further increase in pressure gradient upstream of the thickening, leading to more thickening. This process repeats, until the thickening decays out at some upstream location. If the initial pressure gradient is large enough, for instance, due to a larger surface protrusion, then this leads to local separation of the boundary layer leading to a *dead-air* region downstream ([Krechethikov and Lipatov, 2005](#)). In such a case, a separation (oblique) shock wave is created. A schematic of such a flow separation due to a forward facing step can be seen in Fig.2.2.

The flow separation phenomenon only gets complex when a three dimensional effect is introduced. In the literature, a three dimensional protuberance is classified into two main categories (Hung and Clauss, 1980) (Hung and Patel, 1984) (Dolling and Bogdonoff, 1981) based on its height (H) and Diameter (D) as seen in the Fig. 2.3. A protuberance can be considered as short, if $H < D$. In this case, the height of the protuberance will be in the order of the local boundary layer height (δ). The separation shock, which forms upstream of the roughness element will deflect some proportion of the boundary layer over the element and a recirculation region would form at the base of this short roughness element. On the contrary, if the height of the roughness element is greater than two times its diameter ($H > 2D$), then it can be classified under Tall or Large protuberance. The height in this case is many times the boundary layer thickness and at least one order of magnitude larger. Since most of the protuberance is exposed to the external supersonic flow, a strong bow shock wave is created upstream of the element, leaving it exposed to predominately subsonic flow. The pressure and heat loads in this case are relatively high. However, since short protuberances are sometimes unavoidable on practice, the scope of this work will also be restricted to the same.

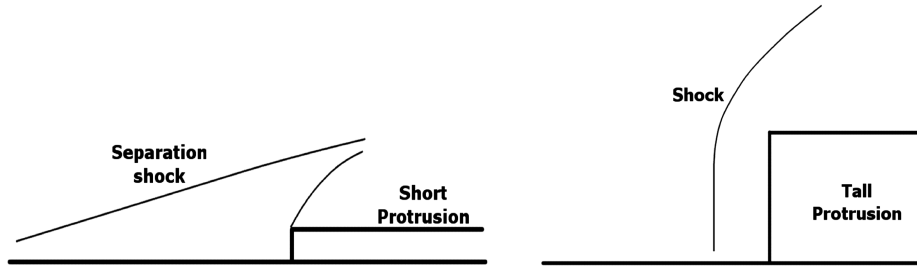


Figure 2.3: Flow-field near short and tall Protuberance (Kumar and Reddy, 2014)

The separation region upstream features a complex system of shocks and vortices. Flow visualisation experiments carried out by Baker (1979) in the low speed environment showed the existence of a horse-shoe vortex system with the number of upstream span wise vortices, heavily dependent on the Reynolds number. A similar vortex system was also observed in the recent computations of Iyer and Mahesh (2013) and Subbareddy et al. (2014) in the high speed regime. Iyer and Mahesh (2013) performed a DNS study of a hemispherical bump for the conditions of Danehy et al. (2009). The three dimensional separation region in the upstream region can be seen in their instantaneous snapshots shown in Fig.2.4

When they analysed the upstream separated region, an unsteady 6 vortex system was identified in the lowest Mach number case. The centreline Stanton number plot showed a peak in the regions between the vortices, where there is a central down wash. Of the three major sources of unsteadiness discussed by the authors, two of them - unsteady vortex system and shock induced unsteadiness, lie in the upstream region. Turbulent kinetic energy possessed the highest value near the vortex system, making it one of the major sources of unsteadiness in the system.

A similar case was also observed from the computations of Subbareddy et al. (2014) for a cylindrical roughness element of $H/\delta > 1$ and corresponding to the condition of the experiment conducted by Wheaton and Schneider (2012). However, while the computations of

and [Hung and Patel \(1984\)](#) performed one of the earliest parametric study experiments to investigate the interference heating due to a three dimensional cylindrical element at Mach 5.3. They observed an increase in peak heating with its height, until the protuberance becomes large. The hypersonic interference heating was also extensively investigated more recently by [Estruch-Samper et al. \(2010\)](#) from Mach numbers ranging from $M = 8.2 - 12.3$, from which a semi-empirical correlation to predict the peak heating was formulated. An assessment of the shock system was also made at different deflection angles of the protuberance. They observed a peak heat flux to the side of the element for flows which are unseparated and for flows which does undergo separation, they found peak loading just upstream. The separation behaviour is also heavily influenced by the deflection angle of the protuberance. Fig.2.6 shows the Schlieren images of [Estruch-Samper et al. \(2010\)](#) showing conditions which trigger separation. Separation shock can be clearly seen in protuberances with higher deflection angles in the image. In another study, [Estruch-Samper \(2016\)](#) investigated the reattachment heating upstream of a short compression ramp in the same facility. Based on the results obtained, he concluded that the re-attachment heating increases with increase in the separation length. This highlights the importance of studying the separation distance upstream of a protuberance.

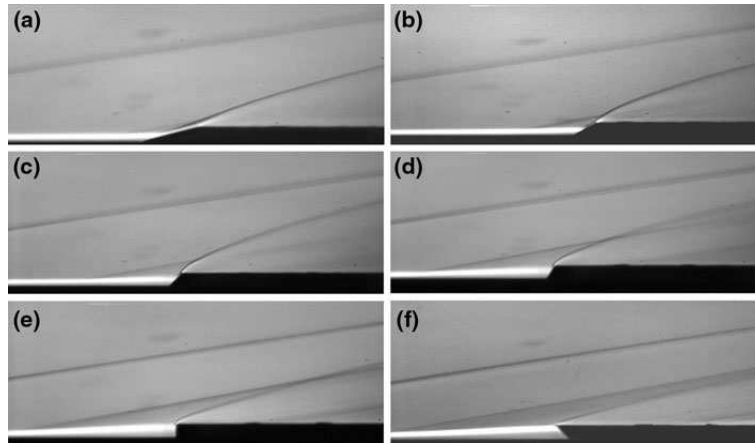


Figure 2.6: Schlieren images of a 3D protuberance in an incoming laminar boundary layer at $M_\infty = 8.2$ and $Re_\infty/m = 9.35 \times 10^6$ for deflection angles of (a) $\alpha = 15^\circ$, (b) $\alpha = 30^\circ$, (c) $\alpha = 45^\circ$, (d) $\alpha = 60^\circ$, (e) $\alpha = 90^\circ$ and (f) $\alpha = 135^\circ$ ([Estruch-Samper et al., 2010](#)).

[Kumar et al. \(2014\)](#) performed a similar study on 3D protuberances of various heights at Mach 5.7 and Mach 8.2 and quantified the length of separation to be approximately between 10.5 - 12 times the protuberances height in a flat plate, and between 9 - 10.5 times the height for a cone. However, even though a 3D protuberance was used, an analysis on the effect of width on the upstream separation region was not provided.

While the existence of the upstream vortex system have been long known, its experimental confirmation was later provided by [Avallone et al. \(2016a\)](#) who utilised Particle Image Velocimetry (PIV) and Quantitative Infrared Thermography (QIRT) to investigate the separation region upstream of a roughness element in an incoming laminar boundary layer. By utilizing the measurement techniques to characterise the flow and the wall heat flux in a similar environment, the exact relation between the vortex system and the wall heat flux was clarified as shown in Fig.2.7. The centreline Stanton number peak observed, was attributed

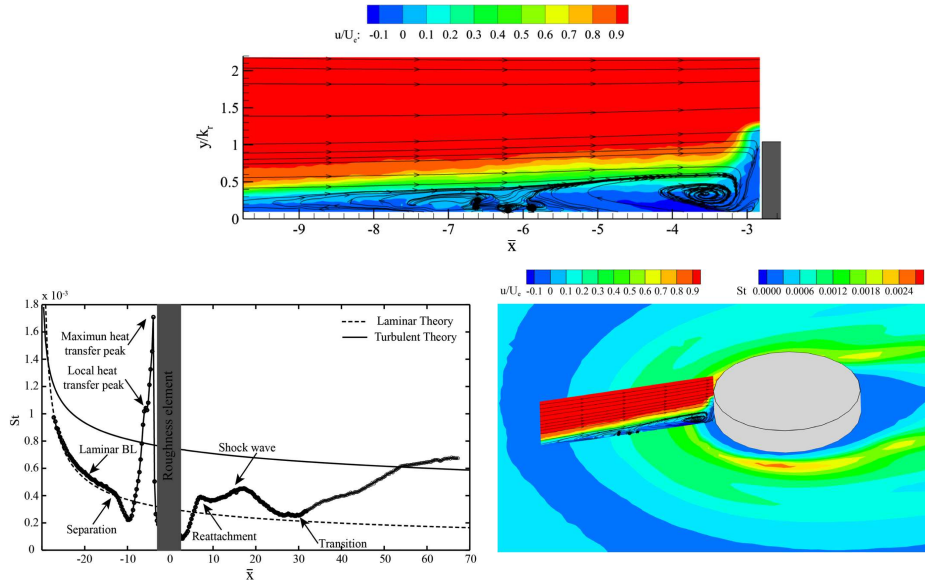


Figure 2.7: Mean velocity profile upstream of a cylindrical protuberance showing the system of vortices upstream (Top), Centreline Stanton number variation showing the heat transfer peak upstream (Bottom Left) and comparison of surface Stanton number variation with the centreline mean velocity profile showing the peak Stanton number occurring due to local central down wash (Bottom Right) (Avalone et al., 2016a).

to the large primary vortex which entrains the high momentum fluid toward the wall causing a local central down wash. Turbulent kinetic energy distribution calculated using the PIV velocity vectors, showed a region of high unsteadiness near the vortex system.

2.2.2 Boundary Layer Transition

A large enough protuberance placed in a laminar boundary layer has the potential to accelerate the transition process (Reshotko, 2001). In this section, the impact of the presence of a surface protuberance on the boundary layer transition downstream of the element will be discussed.

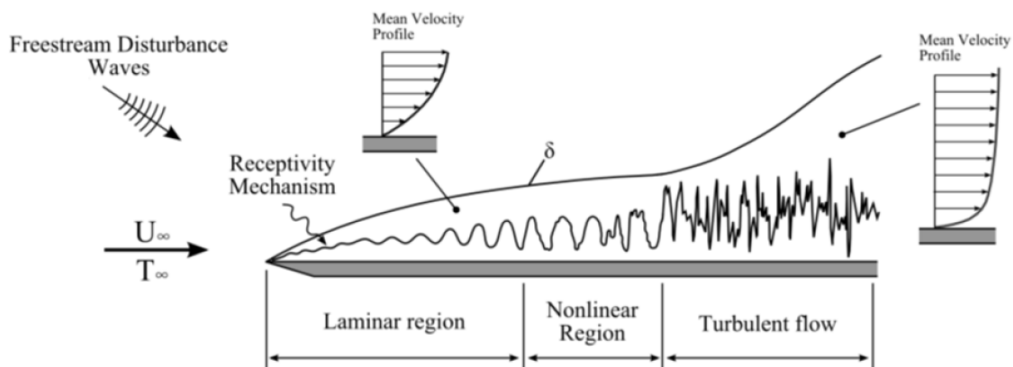


Figure 2.8: Laminar to Turbulent boundary layer transition (redrawn from Masutti (2013))

An understanding of how a laminar boundary layer undergoes transition to turbulent boundary layer is essential before embarking into transition induced by an external roughness element. The following description, provided by Reshotko (2008) gives a qualitative illustration of transition from laminar to turbulent boundary layer. It is schematically shown in Fig. 2.8.

Any disturbances in the free-stream (e.g. acoustic waves) enter the boundary layer as steady and/or unsteady fluctuations of the basic state. This mechanism, called as *receptivity* by Morkovin (1969), provides the vital initial conditions of amplitude, frequency, and phase for the breakdown of laminar flow. A variety of these instabilities can occur either independently or as a combination and is heavily influenced by parameters such as the Reynolds number, wall roughness, curvature etcetera. Linear stability theory utilises a linearised, unsteady NS equations to describe the initial growth of these instabilities. This growth is weak though. However, as the amplitude of the disturbances grows, 3D non-linear interactions starts to occur as secondary instabilities, which is very rapid and eventually breaks down to turbulence.

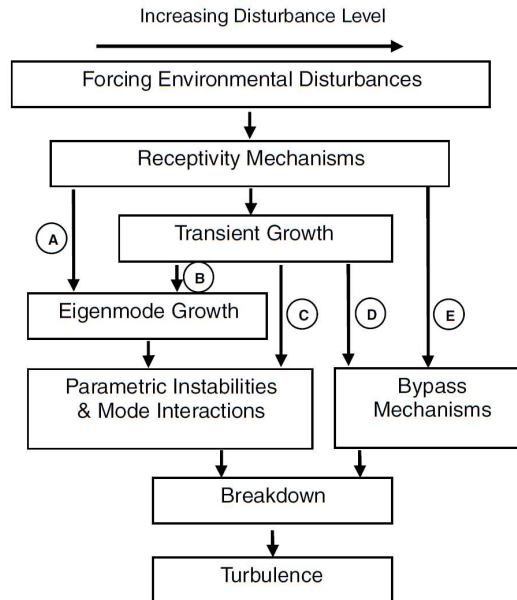


Figure 2.9: A Roadmap for transition from Laminar to Turbulence (redrawn from Reshotko (2008))

Until about a couple of decades ago, the main view of transition from laminar to turbulent was thought to be through the slow linear amplification of disturbances, initialised by the receptivity process and growing exponentially (Tollmien-Schlichting waves). This is followed by the secondary instability, leading to further non-linearity and finally, a complete breakdown to turbulence (Reshotko, 2001). However, Morkovin (1985) proposed a non-linear *Bypass transition* where the transition to turbulence could not be attributed to the 'T-S path'. One candidate mechanism for bypass transition is transient growth, which Reshotko (2001) argues that it could be a significant factor in transition for T-S stable flows. The consequence of this has led to five possible paths for a flow to undergo transition from laminar to turbulent and is shown in Fig.2.9. Reshotko (2008) provides a detailed discussion of each of the five path, which is briefly summarised as follows.

- *Path A* is the traditional path to turbulence in low disturbance environment, where the transition is due to T-S, Görtler or cross-flow mechanisms as described earlier.
- *Path B* scenario is the one where a disturbance's amplitude is first increased by transient growth, thus providing higher initial amplitude for the growth of eigenmodes, followed by region of exponential decay.
- *Path C* corresponds to transition in the absence of eigenmode growth. This path can be included to the previously classified *Bypass transition* case.
- *Path D* concerns with transition in internal flows at elevated turbulence level.
- *Path E* represents a case where the forcing possesses a very large amplitude without any linear regime and hence the resultant disturbance levels are very large.

For any type of the paths discussed earlier, it is essential to understand the process of receptivity, by which the disturbances enter the boundary layer and provides the initial conditions to determine the growth (White et al., 2005). But quantifying the initial input forcing for transient growth still remains a challenge (Sharp, 2014). However, it is a known fact that the primary effect of a surface roughness is to increase the magnitude of any perturbations in the flow (Klebanoff et al., 1955) and hence the presence of a roughness will always move the transition location forward with respect to the smooth wall transition location.

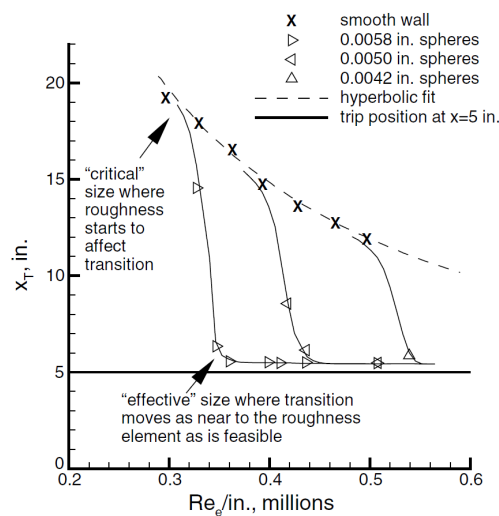


Figure 2.10: Critical and Effective height of roughness elements (van Driest and McCauley, 1960)

One of the classical examples in literature portraying the effects of roughness elements on a boundary layer was the experiment carried out by van Driest and McCauley (1960). They made measurements on a cone with an half angle of 5 degrees, with azimuthally placed spherical roughness elements and at a boundary layer edge Mach number of $M_e = 1.9$. They plotted the location of transition point, with respect to unit Reynolds number based on conditions at the edge of the boundary layer (see Fig. 2.10). Analysing the nature of the shift in the transition location, two types of transitions conditions can be defined. The transition location begins to deviate from the smooth wall condition at a particular height as seen in the

figure. This corresponds to the *critical* condition. However, as the height of the roughness element is further increased, the transition point moves closer to the trip position and at a particular *effective* height, it reaches the near wake region. It has to be noted that, both the critical and the effective trip heights are dependent on various factors like the type and shape of the trip, free-stream noise, etc (Choudhari et al., 2010).

In addition to height of the roughness element factors such as Mach number, wall temperature, nose bluntness, real-gas effect, wall curvature, Reynolds number based on local boundary layer momentum thickness (Re_θ), etc. also influence in various levels. This dependencies on a number of parameters makes high-speed boundary layer transition one of the unsolved problems even after extensive experiments and computations for close to two decades (Schneider, 2008a). However, with the advent of new experimental techniques and high fidelity computations, it is now possible to peer into the wake of the roughness elements to understand the flow topology and surface heat transfer rates.

Danehy et al. (2009) performed one of the earliest experiments on boundary layer transition due to a hemispherical roughness element for Mach numbers ranging from 3 to 8, using non-intrusive Nitric Oxide planar laser-induced fluorescence (NO PLIF). They reported the existence of cork-screw based structures downstream of the roughness element, later identified to be stream wise vortices by other researchers. However, their analysis was mostly qualitative and does not provide any quantitative analysis of the vortices. Non-intrusive quantitative measurements were quite difficult to procure in high speed compressible environment at that time. This left some researchers to use conventional techniques like hot-wire or Pitot measurements. Sharp and White (2014) took measurements on the Texas A&M Mach 6 Quiet Tunnel and observed roughness induced transient growth in the hypersonic environment. Though this measurement made the first such observation in the hypersonic domain, it is still intrusive in nature and the probe used might alter the local flow field.

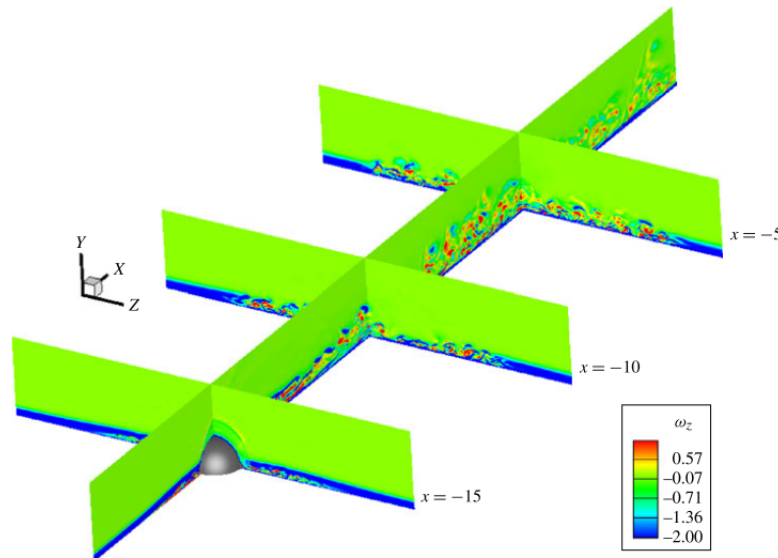


Figure 2.11: Perturbation of the separated shear layer in Mach 3.37 flow (Iyer and Mahesh, 2013)

While developments were being made to non-intrusive measurement techniques, advancements in high-fidelity computational techniques have enabled researchers to analyse the transition phenomenon in elaborate detail. [Iyer and Mahesh \(2013\)](#) performed an extensive DNS analysis on the conditions of [Danehy et al. \(2009\)](#) and were able to qualitatively and quantitatively validate their computation, which enabled them to continue on with a much through analysis. For a $H/\delta > 1$, the isolated hemispherical bump forced transition for the two lower Mach numbers, $M = 3.37$ and $M = 5.26$, while the $M = 8.23$ flow did not undergo transition. This is in accordance to the stability effect of Mach number. The vortices formed upstream wrap around the roughness element as discussed in the earlier section and forms into a system of counter rotating stream wise vortices in the wake region. These stream-wise vortices perturb the shear layer and depending on the strength of the vortices, stability, etc the shear layer may finally break down, leading to turbulence. Small hairpin-shaped vortices are eventually observed denoting transition to turbulence. Fig. 2.11 shows the perturbation of the shear layer in Mach 3.37 flow, where the perturbations can be seen growing in the stream-wise and span-wise directions. A similar DNS simulation performed by [Subbareddy et al. \(2014\)](#) also showed the shear layer breaking down to form hairpin-vortices and eventually transition.

Analysis of isolated roughness induced transition using high fidelity computations continued further. [Choudhari et al. \(2010\)](#) studied the Laminar-Turbulent transition behind a diamond trip on Mach 3.5 flow. They observed a series of high and low speed streaks, similar to what [Fransson et al. \(2004\)](#) observed in low-speed flows. The low and the high-speed streaks are formed due to the streamwise vortices moving the high momentum fluid towards the wall and low-momentum fluid away from the wall.

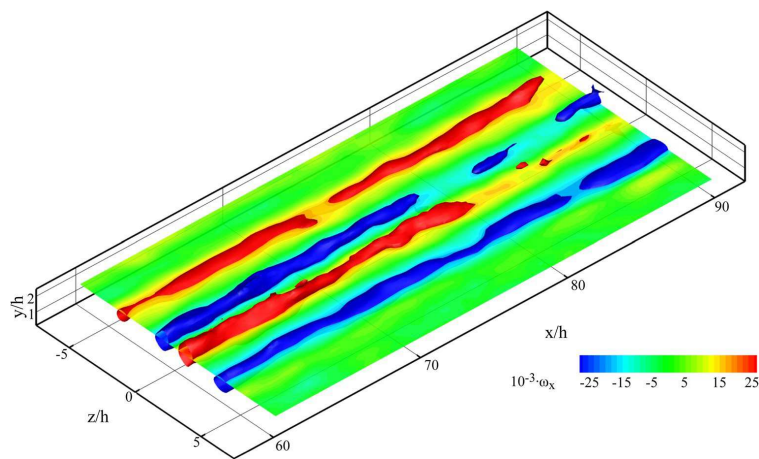


Figure 2.12: Isosurfaces of streamwise vorticity (clockwise rotation is represented by blue and anticlockwise in red) ([Avallone et al., 2014](#))

With the improvements made to advanced laser diagnostics, researchers were able to quantitatively study the wave flow behind a roughness element in a hypersonic environment. [Avallone et al. \(2014\)](#) and [Ye et al. \(2017\)](#) performed Tomographic PIV to study the three dimensional flow organisation behind a cylindrical and micro-ramp element respectively and experimentally verified the occurrence of counter-rotating stream wise vortices downstream as can be seen from the isosurface of stream wise vorticity in Fig. 2.12. Maximum streamwise velocity fluctuations were found near the vicinity of the stream wise vortices in both cases.

Another experimental method to investigate the flow organisation in the wake region non-intrusively is to study the footprint of the flow on the model surface. Traditional techniques involve the usage of oil flow visualisation (Whithead, 1969) or fluorene sublimation (Hicks and Harper, 1970). However, since one of the main consequences of boundary layer transition in high speed flows is the high thermal loading on the surface, several heat flux measurements were also taken. Tirtety et al. (2011) employed Quantitative Infra-red Thermography (QIRT) to study the surface heat transfer rates for different roughness elements and concluded the existence of strong flowfield similarities. They concluded that the roughness elements act as vortex generators, which amplifies the disturbances leading to transition downstream. Avallone et al. (2016b) performed a similar experiment on cylindrical and diamond shaped roughness elements and provided some evidence connecting the surface heat transfer with the flow-field topology and hence successfully predicted the location of transition location for different roughness elements. Fig. 2.13 shows the variation of the centreline Stanton number, downstream of three different roughness elements as reported by Avallone et al. (2016b). For all the roughness elements, they associated the transition location as the point where the slope of the Stanton number starts to diverge. This was reported based on the study of evolution of the wake width downstream of the roughness elements and comparing them with velocity fluctuations measured using Tomo-PIV. QIRT was also employed by Ye et al. (2016), who studied the heat flux distribution downstream of cylinder and micro ramp geometries at Mach 6.48 flow and observed the upstream motion of transition location with increase in roughness height based Reynolds number (Re_H).

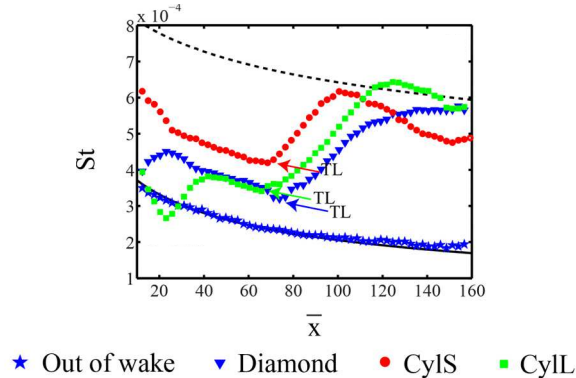


Figure 2.13: Centreline Stanton number variation (Avallone et al., 2016b)

Irrespective of the decades of investigation being made in the field of high speed boundary layer transition, a physics based model is still far from development (Schneider, 2008b). Some researchers believe that the transient growth theory (Reshotko and Tumin, 2004) or the secondary instability theory (Choudhari et al., 2009) could be a good candidate mechanism to compute the growth of amplification of disturbances downstream of the roughness element. Since that's still under the process of being established, researchers have adopted some empirical and semi-empirical correlation to try to predict transition. Reda (2002) has provided an extensive review of various correlations used to predict transition. Some of the well known correlations are the Shuttle criterion (Berry et al., 1998), PANT correlation (Wool, 1975), van Driest and Blumer (van Driest et al., 1967) etc. Some of them attempted to consider as much physics as possible in their correlation. However, the relations might not be entirely reliable

outside of the dataset they are generated from, which is one of the reasons why a purely physics based model to predict transition is essential. A larger experimental and computational dataset, with analysis of the effect of the various parameters on the wake topology and transition could potentially help develop a theory based on physics.

2.3 Incoming Turbulent boundary layer

While the effect of protuberance in a laminar boundary layer is interesting to investigate, most boundary layers are turbulent in nature when they meet a surface protuberance. Hence extensive research has also been carried out to understand that phenomenon. In this section, the most relevant literature on the effect of protuberance when placed on an incoming turbulent boundary layer will be discussed.

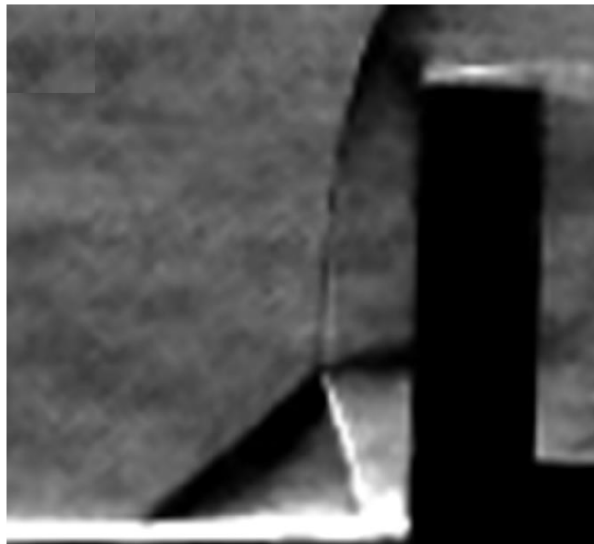


Figure 2.14: A Schlieren image showing the λ - shock system upstream of an asymptotic cylinder (Lash et al., 2016)

The literature on interaction of a protuberance in an incoming turbulent boundary layer is focused mainly on the associated cylinder induced shock wave boundary layer interactions upstream of the protuberance. Similar to the laminar case discussed earlier, the protuberance in a turbulent boundary layer can be either large or small. The flow field here is also characterised by a λ - shock system, with an inviscid bow and a separation shock wave. The oblique separation shock and the element is separated by an unsteady separation region. The intersection point of the λ - system is known as the *triple point* and its height is known as the *triple point height*, represented by h_{tp} . A majority of the literature published on cylinder induced shock wave boundary layer interaction focused on a special semi-infinite case. A surface protuberance is said to be semi-infinite, if the height of the protuberance has reached a certain 'asymptotic height' where, the scale of the interactions does not depend any more on the height of the element. After extensive analysis, Dolling and Bogdonoff (1981) have reported that this height is approximately 2-3 times h_{tp} . A sample Schlieren depicting the λ - system discussed above, is shown in Fig.2.14.

Accurate prediction of the extent of upstream separation region (L_{sep}) is essential to gain an idea of pressure and heat loads on the surface. A number of co-relation were reported in the 1960s and 1970s and concluded that the upstream separation region scaled with the diameter (Westkaemper, 1968) (Sedney and Kitchens, 1977). Westkaemper (1968) conducted experiments on a large collection of cylindrical protuberances with height, $H > \delta$ and provided correlation for the upstream separated region. He concluded that the L_{sep}/D is depended strongly on the aspect ratio H/D and quite weakly on the Reynolds number. However, compared to the laminar case, due to the relevance and practical interest, the upstream separation region of turbulent case in general was studied rather extensively.

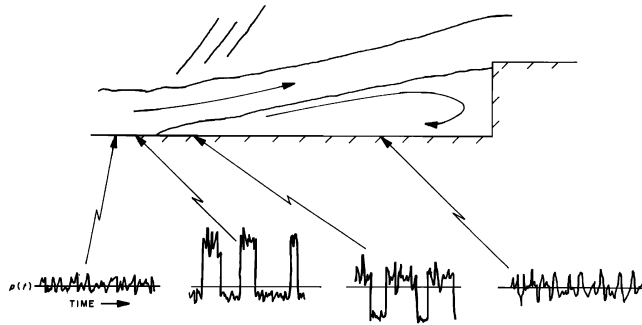


Figure 2.15: Fluctuation pressures at various points in the vicinity of the separation point upstream of a forward facing step (Kistler, 1964).

Bogdonoff (1955) provided one of the earliest evidences of the shock wave turbulent boundary layer interactions by studying Schlieren and shadow-graph movies. Later, wall pressure measurements were also carried out by Kistler (1964) at various locations near the vicinity of the separation point upstream of a forward facing step. A qualitative comparison of wall pressure measurements at different locations is shown in Fig.2.15. One can clearly see that fluctuations of larger amplitude, with a step-rise like signal, dictating the passage of the shock. This provides convincing evidence that the separation shock is quite unsteady.

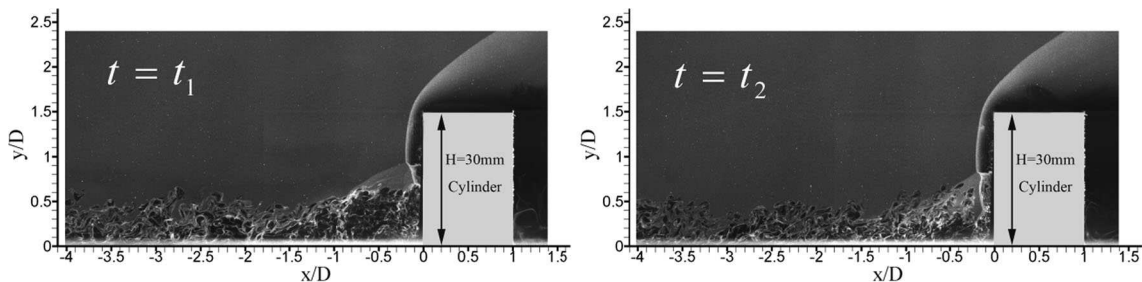


Figure 2.16: Instantaneous NPLS images showing the fine turbulent structures (Gang et al., 2016)

The techniques used by the above researchers to determine the upstream separation length were mostly limited to the mean separation length and hence the fluctuating components were not discussed. More recent and advanced measurement techniques have attempted to study this unsteady separation shock, focusing more on the upstream fluctuations. Gang et al. (2016) studied the fine structures of the cylinder induced shock wave boundary layer interac-

tions using a nano particle based planar laser scattering method (NPLS), an instantaneous picture of which is shown in Fig.2.16. On analysing a series of 500 images, they concluded that the triple point height fluctuation showed a normal distribution. Lash et al. (2016) utilised advances in high speed Schlieren coupled with digital image processing to study the unsteady shock system upstream of an asymptotic cylinder. While their technique is simple and novel, their analysis was mostly limited to an incoming transitional boundary layer and hence extensive analysis on an incoming turbulence boundary layer was not provided.

As stated in the earlier section, the unsteady region in the upstream region is quite detrimental since it may cause fluctuating pressure and heat load. A number of articles have been published analysing the aerodynamic heating of a rather large protuberance on a surface with a turbulent boundary layer (Evans and Smits, 1996) (Mee et al., 2002). However, most utilised a thin film heat-flux gauges and hence their positions are constrained. Moreover, it gets challenging to have a map of heat flux around the protuberance with such sensors. Also, most of the literature focused on regions upstream of a protuberance, where a high heat transfer is observed. However, it is still a question as to what is the effect of a surface protuberance on the heat transfer profiles downstream in the wake region. To the knowledge of the author, one of the only known measurement downstream of a cylindrical protuberance in a turbulent boundary layer was performed by Couch (1969) who studied the wake at Mach 2.49 and Mach 4.44. Based on his measurements, a higher surface shear stress was observed downstream of the cylinder, which indicates a possible high heat flux region.

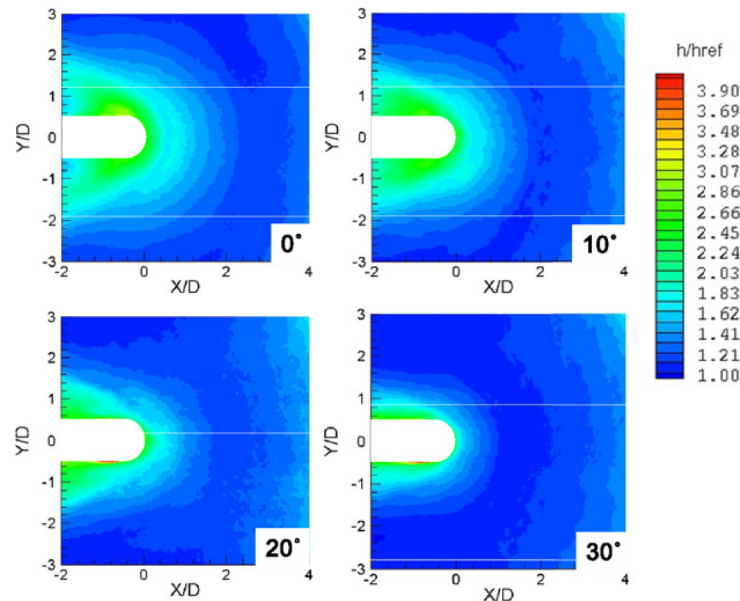


Figure 2.17: Convective heat transfer at different sweep back angles (Yu et al., 2012)

Quantitative Infrared Thermography (QIRT) has gained some interest in the past years in laminar-turbulent boundary layer transition in high speed flows (Avallone et al., 2016b) (Tirtety et al., 2011). Except for the study made by Yu et al. (2012), Infrared Thermography has not been applied to investigate the aerodynamic heating of a SWTBLI due to a cylindrical protuberance. Yu et al. (2012) investigated the heat transfer profiles around

asymptotic cylinders, at different sweep back angles, which is shown in Fig.2.17, based on which, they concluded that the sweeping of cylinder helps reduce the upstream separation region and hence decrease heat transfer in the vicinity, as can be seen in the figure. However their measurements are also rather limited with data presented for a cylinder of single diameter at various sweep angles. Thus with the advent of modern advances in measurement techniques, this phenomenon of cylinder induced shock wave turbulent boundary layer interaction and the associated wake can be investigated more thoroughly.

2.4 Research Aim and Objective

In the last few sections, some of the relevant research conducted to understand the effects of a surface protuberance on a high speed boundary layer was discussed. The research gave insights on the general flow organisation and surface feature evolution around a protuberance both in the laminar and the turbulent boundary layers. However, in the laminar part, further studies on the upstream separation region and the downstream wake region is essential and its influence on the diameter of the protuberance was not discussed to a great extent. While in the turbulent part, any influence of the surface geometry on the heat flux evolution on the surface needs to be investigated, especially in the wake region where a possible high heat flux region is expected. Also, it is interesting to note that almost all the study done on the effect of surface protuberance on a turbulent boundary layer was for a rather large element, which has already reached the asymptotic height. Data on short protuberances was very scarce. Based on these, the following research objectives can be identified.

- *The first research objective is to investigate the effect of geometry of isolated roughness elements in a hypersonic laminar boundary layer by determining its influence on upstream separation region and the downstream transition region through the analysis of the heat flux evolution on the surface using Quantitative Infrared Thermography.*
- *The second research objective is to investigate the effect of geometry on the upstream unsteadiness and to characterise the heat flux evolution around isolated surface protuberance in an incoming supersonic turbulent layer using Quantitative Infrared Thermography and High Speed Schlieren Photography*

To realise the research objectives, the following research question are framed.

1. What is the effect of geometry of the roughness element on the surface heat flux evolution around the protuberance placed in both laminar and turbulent boundary layer?
 - (a) Is there any geometrical scaling that can be identified for the heat transfer distribution?
 - (b) How influential is the diameter on the upstream separation region ?
2. What is the effect of geometry on the upstream instabilities in an incoming turbulent boundary layer?
 - (a) what is the relationship between the shock unsteadiness and the height of the protuberance for a 'non-semi infinite' case of the cylinder ?

The data for the laminar boundary layer analysis was obtained from the measurements made on the Hypersonic Test Facility Delft (HTFD), while the ST-15 supersonic tunnel was used for the turbulent interactions. QIRT was chosen because of its ability to produce a 2D heat transfer distribution, without affecting or influencing the flow field directly (non-intrusive in nature). More details on the flow facility and the operating principles of the measurement techniques will be found in the subsequent chapters.

Chapter 3

Experimental Methods

In this chapter the principle behind the different measurement and visualisation techniques utilised in this thesis will be discussed. Quantitative Infra-red Thermography (QIRT) will be used as the main investigative tool, assisted by Schlieren and Oil Flow visualisations.

3.1 Schlieren Visualization

Schlieren is an optical visualization technique used to visualize the density gradients in a flow. It is a prime source to qualitatively and sometimes quantitatively analyse a supersonic airflow for features like shock waves, expansion waves, boundary layers and other general flow topology. It relies on the relationship between the refractive index of a medium (n) and the speed of light in that medium (c), given by the expression:

$$n = \frac{c_v}{c} \quad (3.1)$$

where, c_v is the speed of light in vacuum. The refractive index is further related to the density of the medium by the Gladstone-Dale equation (Settles, 2001) given by:

$$n = 1 + \kappa\rho \quad (3.2)$$

where, κ is the Gladstone-Dale constant ($\kappa_{air} = 0.23cm^3/g$). The perfect gas state equation relates the pressure and temperature to the density through the equation:

$$p = \rho RT \quad (3.3)$$

Thus, it can be established that matter slows down light and the density of a medium (which is related to the pressure and temperature) establishes the speed of light in that medium. An inhomogeneous medium with gradients in density will hence refract and bend the light rays passing through it. If light rays are assumed to pass through the z - direction in a three dimensional right handed Cartesian coordinate system, the resulting curvature of light in the other two directions (x, y) are given by the expressions:

$$\frac{\partial^2 x}{\partial z^2} = \frac{1}{n} \frac{\partial n}{\partial x}, \quad \frac{\partial^2 y}{\partial z^2} = \frac{1}{n} \frac{\partial n}{\partial y} \quad (3.4)$$

Upon integrating these expressions the angular ray deflection (ϵ) in both the directions are given by:

$$\epsilon_x = \frac{1}{n} \int \frac{\partial n}{\partial x} dz, \quad \epsilon_y = \frac{1}{n} \int \frac{\partial n}{\partial y} dz \quad (3.5)$$

In a compressible flow field, features such as shock waves, expansion waves, boundary layers, etc., are sources of gradients in density and hence the local refractive index. Any light ray passing through will thus be deflected towards the region of higher density (given by equation 3.5) which can be visualised using a simple Schlieren setup. A schematic of a Z-type Schlieren setup is shown in Fig.3.1.

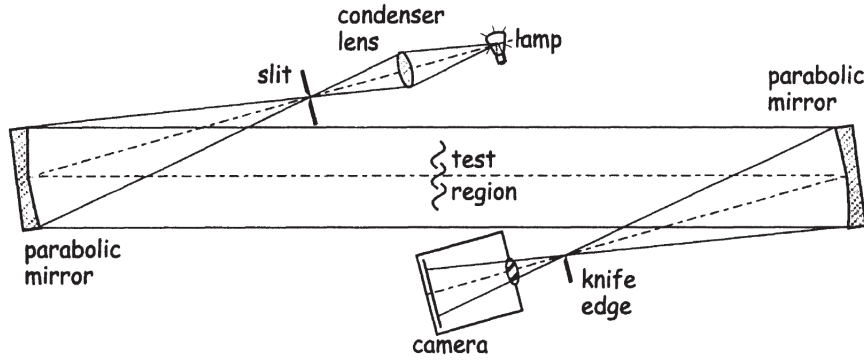


Figure 3.1: Schematics of a Z - type Schlieren system (Settles, 2001)

A continuous or a spark light source is focused onto a slit (or a pinhole), which is in turn placed at the focal point of the first parabolic mirror. The incoming light is now collimated by the first parabolic mirror and this beam now passes through the test section. A second parabolic mirror is placed on the other side of the test section which collects the light rays and focuses it onto a knife edge. The knife edge is used to block one half of the incoming light beam. This does not make any effect during tunnel-off condition. However, during the tunnel-on condition, density variations in the flow deflects the focal point in the direction dependent on the direction of density gradient in the flow. A horizontal knife edge configuration would be sensitive to the vertical gradients in the flow and a vertical knife edge configuration would be sensitive to the horizontal gradients in the flow. Depending on the orientation of the knife edge, the deflected light ray would either be allowed to pass or blocked by the knife edge, showing distinct white and dark regions on the image.

While historically, schlieren images were only used for qualitative analysis, recent advancements in camera performance and digital image processing have also provided the possibility to gather certain quantitative data out of this technique. An high speed imaging system would be able to capture the oscillating shock waves from which, time-resolved shock position data can then be obtained. More details on the arrangement and the data reduction procedure to determine the shock position from schlieren images will be provided in Section 6.5.

3.2 Oil Flow Visualisation

Oil flow visualisation techniques is one of the traditional methods to have a qualitative interpretation of the surface flow features in both subsonic and supersonic flows. It is a quick way for the experimentalist to examine the surface flow topology and is widely used owing to the wealth of information obtained at a relatively low cost. In this technique, a thin layer of oil mixed with a coagulating agent is applied on to the region of interest. The oil flow pattern formed during the wind tunnel run can be correlated to topological features in the boundary layer near the wall. The thin film of oil experiences pressure and shear forces during the wind tunnel run due to which, it is subjected to a small velocity. Squire (1961) determined the solution for the motion of a thin oil sheet on a surface, under the influence of a boundary layer. He concluded that the presence of oil has very minimal effect of the state of the boundary layer, provided that the oil viscosity is much greater than the the working fluid, i.e. air. Based on his solutions, it can also be stated that the oil flow pattern depict the surface streamlines, expect near points of large pressure gradient like separation point. Under such cases, the oil tends to accumulate just upstream of the true separation point.

In this investigation, oil flow analysis is used to determined the general surface features around the protuberance in addition to the upstream separation distance. Since there is a 5% ambiguity in the exact location of the separation point (Squire, 1961), this is not utilised as a primary tool to measure the separation length, but rather to augment the data collect by other means. For the visualisation reported in this thesis, the Shell Tellus type 22 oil and TiO_2 particle (Sachtleben UV-TITAN L-530, 30nm crystal size) mixture was used. A few drops of oleic acid were added to make sure that the viscosity of the mixture was suitable for the operation. Also, usually the oil flow is visualised and photographed only after the wind tunnel is off. However, any shock waves that emanate due to the sudden tunnel off condition may wipe out a portion of oil and thus may affect the oil flow pattern. Hence it is necessary to investigate the effect of the tunnel condition on the oil flow pattern.

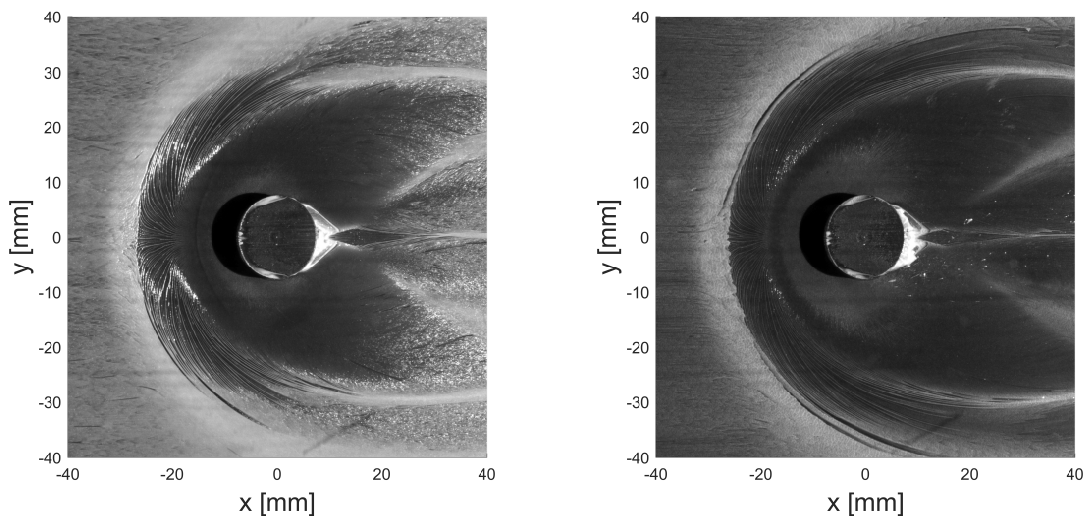


Figure 3.2: Oil flow pattern at Tunnel ON (left) and Tunnel OFF (right) conditions

This is achieved by mounting a LaVision Imager LX camera with a CCD chip of 1624×1236 pixels near one of the optical access and constantly recording the transient oil flow patterns around the elements in the opposite tunnel wall. Fig.3.2 shows the effect of the tunnel condition on the oil flow pattern. Notice that once the wind tunnel is OFF, a large portion oil has been wiped off, leaving only the outlines. On the other hand, the tunnel ON image has clear skin friction lines in the upstream region. Recording transient oil flow pattern is important to verify whether the shock wave has significantly altered the oil flow pattern from the tunnel on and tunnel off conditions.

3.3 Infrared Thermography

Infrared Thermography (IR), is a powerful optical tool, used to estimate the convective heat flux or to evaluate the surface flow features in a non-intrusive manner (Carlomagno and Cardone, 2010). It can be used to assess the state of the boundary layer, locate the transition, separation and reattachment points, which are of quite some interest to aerodynamicists. In this section, the basic working principle of Infrared Thermography is provided along with the description of the IR camera and its calibration procedure.

3.3.1 Black Body Radiation

Transfer of heat, and hence energy, can occur in one of the following three forms: conduction, convection and radiation. Conduction and convection mechanisms require a material medium to occur. However, radiation occur by means of electromagnetic waves and hence do not require any material medium. Any material above absolute zero, emit electromagnetic radiation, which is dependent on the temperature of the material. However, in order to obtain a theoretical formulation, the concept of *black body* is used. A *black body* is a perfect absorber and emitter of radiation, irrespective of the wavelength of the radiation or the directionality. For such a body, the spectral emissive power can be defined, which is the radiation energy, per unit surface area for a given wavelength (λ) and denoted by $E_{b,\lambda}$. The Planck's law of radiation which provides an expression for this energy flux is given by (Astarita and Carlomagno, 2013):

$$E_{b,\lambda}(\lambda, T) = \frac{C_1}{\lambda^5 (e^{\frac{C_2}{\lambda T}} - 1)} \quad (3.6)$$

where, T is the absolute body temperature in *Kelvin* and C_1 and C_2 are the first and second radiation constants, given by $3.7415 \times 10^{-16} Wm^2$ and $1.4388 \times 10^{-2} mK$ respectively. It is quite clear from this expression that the emissive power is a function of the wavelength of the electromagnetic radiation and the absolute surface temperature. This expression is visualised in Fig.3.3, where the emissive power is plotted against the wavelength of the radiation from bodies at different temperatures. The dotted lines in the figure represent the locus of the maximum possible $E_{b,\lambda}$ for a given temperature. The emissive flux peaks at a particular wavelength λ_{max} . The relationship between this peak wavelength and the absolute surface temperature is provided by the Wien's displacement law (Astarita and Carlomagno, 2013), given by:

$$\lambda_{max} T = 2.898 \times 10^{-3} m \cdot K \quad (3.7)$$

As can be seen in Fig.3.3, the maximum wavelength, λ_{max} decreases with increasing in temperature.

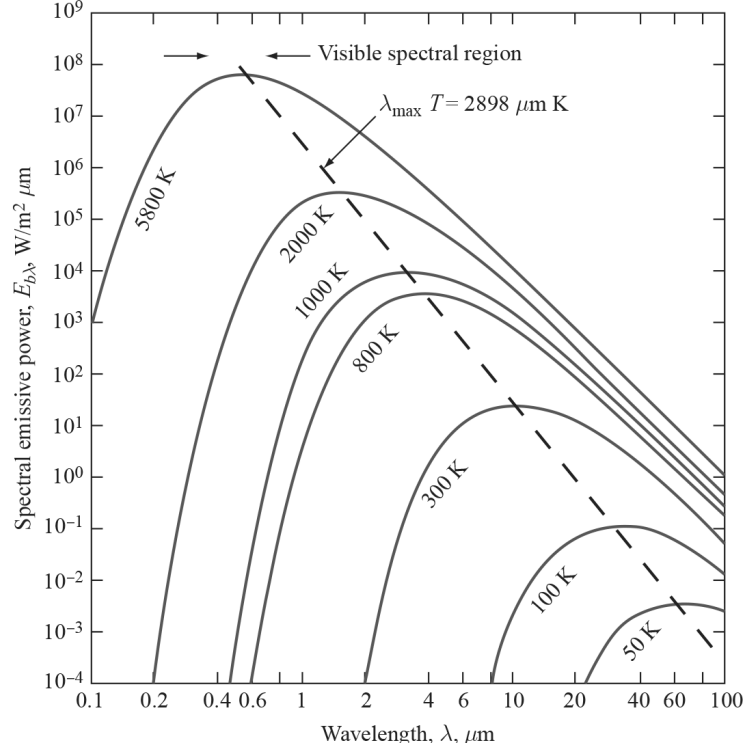


Figure 3.3: Spectral hemispherical emissive power ($E_{b,\lambda}$) as a function of λ for different absolute temperatures (Kreith and Manglik, 2016)

The Planck's law of radiation can be integrated over the entire range of wavelength to obtain the total emissive power of the black body (E_b). This expressive is basically the area under a given curve in Fig.3.3. The resulting expression is called the Stefan-Boltzmann law, given by:

$$E_b = \int_0^{\infty} E_{b,\lambda}(\lambda, T) d\lambda = \sigma T^4 \quad (3.8)$$

where, σ is known as the Stefan-Boltzmann constant, equal to $5.670 \times 10^{-8} W/(m^2 K^4)$. Notice that the total emissive power of the black body is only a function of the absolute body temperature.

3.3.2 Radiation of Real Bodies

Any real body interacts with the incident irradiation in three ways: a part of it may be absorbed by the body, some may be reflected with some may be transmitted through the body as shown in Fig.3.4. However, according to the conservation of energy:

$$\tau_r + \rho_r + \alpha_r = 1 \quad (3.9)$$

where, τ_r , ρ_r and α_r are the fraction of the irradiation transmitted, reflected and absorbed by the body and are termed as *transmissivity*, *reflectivity* and *absorptivity* coefficients respec-

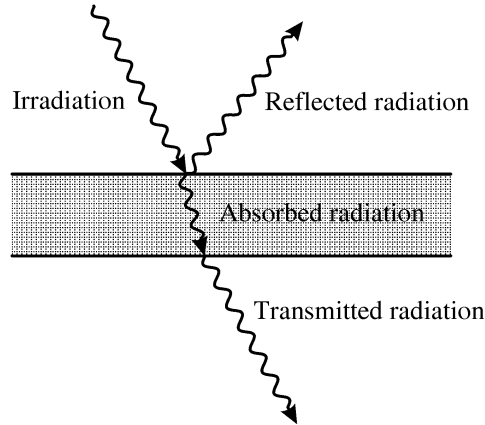


Figure 3.4: Energy reflection, transmission and absorption by a real body (Astarita and Carlomagno, 2013)

tively. A *black body* is conceived as a perfect emitter and absorber and hence, $\alpha_r = 1$ and hence there is no reflection or transmission involved. However, this may not be true for a real body, where the maximum spectral emissive power (E_λ) is only a fraction of the black body spectral emission ($E_{b,\lambda}$). Thus a spectral emissivity coefficient (ϵ_λ) is defined, given by:

$$\epsilon_\lambda = \frac{E_\lambda}{E_{b,\lambda}} \quad (3.10)$$

A body whose emissivity is independent of the wavelength can be considered as a *grey body*. Even if a real body does not satisfy this condition over the entire electromagnetic spectrum, a *grey body* approximation can often be made from the practical point of view since the spectral emissivity can have nearly a constant value in the IR band under consideration (Astarita and Carlomagno, 2013).

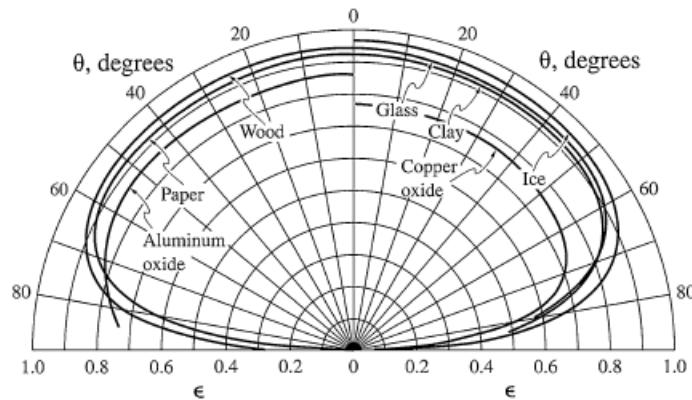


Figure 3.5: Directional emissivity of dielectric and non-metallic materials (Schmidt and Eckert, 1935)

The spectral emissivity can also be dependent on the viewing angle. The directional emissivity of several dielectric and non-metals is shown in Fig.3.5, where θ is the angle between the

direction of emitted beam and the normal to the surface. It can be seen that the dependence of direction on the value of ϵ is very small for θ less than 60° . Given this fact, the viewing angle during the Infrared measurements in this investigation is also maintained less than this angle.

3.3.3 Atmospheric Transmittance

In the previous section, it was assumed that the radiation travel through vacuum and the signature recorded by the camera would be unaffected during its transit from the surface of interest to the camera sensor. However, in real case, measurements are not usually taken in a vacuum environment and based on various factors, the environment has the tendency to reflect and absorb the radiation passing through it. In most practical cases, the measurements will be made in an air environment. The magnitude of the disturbances depend on factors like the distance between the sensor and the surface of interest, the state and composition of the surrounding, external particles in air etc. Assuming that there are no reflective particles floating around, the energy budget reduces to:

$$\tau_{air} + \alpha_{air} = 0$$

Also, assuming standard conditions, the effect of the state of the medium can also be neglected. Hence, the composition of air governs the wavelength of light that will be absorbed in the electromagnetic spectrum. With the exception of H_2O and CO_2 , these factors can also be neglected (Mayer, 1996). The H_2O and CO_2 molecules have the tendency to absorb some wavelengths in the IR spectrum, thus leading to decrease in transmissivity when operated in that regime. Fig.3.6 plots the transmissivity of air at different wavelengths.

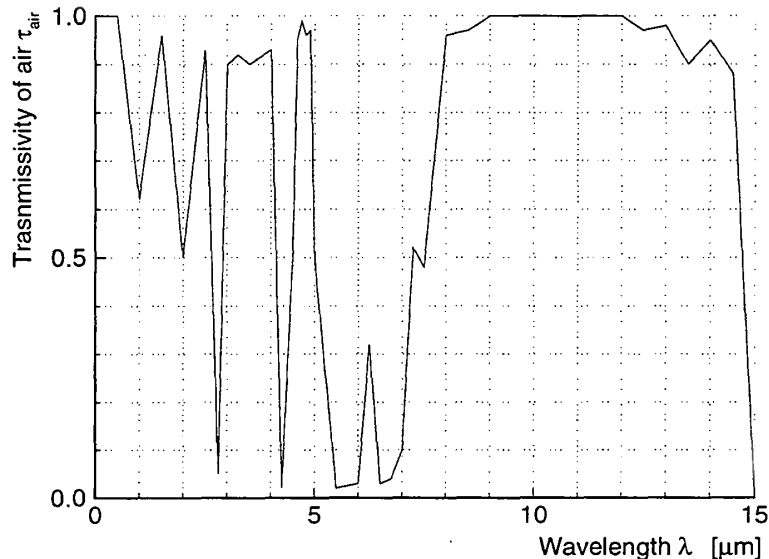


Figure 3.6: Atmospheric Transmissivity at different wavelengths. Measurements taken at 1 atm, 298.15K and at 25% humidity at a distance of 30m (Mayer, 1996)

The significant absorption of radiation for wavelengths upto $5\mu m$ are influenced by the CO_2 in the atmosphere while the absorption in the $5 - 8\mu m$ range are caused by the H_2O in the

air making it almost opaque. Thus, commercial sensors operate in the so called *atmospheric windows* which are regions of high transmissivity that fall into one of the two wave bands:

Short Wave Band	SWB	$3\mu m - 5\mu m$
Long Wave Band	LWB	$8\mu m - 12\mu m$

While this data represents the transmissivity from a distance of approximately $30m$, data collected by [Gebbie et al. \(1951\)](#) show a very similar trend of spectral transmittance of a $1km$ thick atmosphere. Since the laboratory experiments are carried out where the typical thickness of air is around $1m$, the spectral transmissivity is quite high in the wave band considered above and can be safely assumed to be equal to one ([Astarita and Carlomagno, 2013](#)).

3.3.4 Infrared Camera

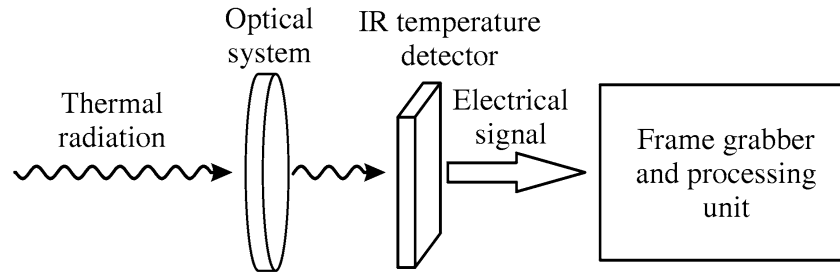


Figure 3.7: Components of an IR acquisition system ([Astarita and Carlomagno, 2013](#))

The schematics of a simple IR sensor is shown in Fig.3.7. It consists of an optical system which collects the incoming radiation and focuses it onto the temperature detector. Unlike a glass lens used in a typical camera, the material used here has to be transparent to the IR wavelengths. The temperature detector generates a proportional electrical signal which is then collected by Frame grabber for further processing.

The IR detector is one of the main components of the camera which converts the impinging radiation into an equivalent electrical signal. Based on their working principle, they are classified into two categories: thermal and quantum/photon detectors. In a thermal detector, the incident radiation changes one of the properties of the sensor, due to changes in the temperature of the detector. Examples of this type of detectors include bolometers (change in conductivity due to temperature change), pneumatic detectors (expansion of gas due to heating), thermopiles (voltage produced due to temperature increase) etc. A quantum detector on the other hand works on the principle of *photoelectric effect*, and is much more sensitive. These types of cameras are hence desirable for quantitative heat flux estimations.

For the investigations reported in this thesis, a CEDIP Titanium 530L measurement system is utilised (Fig.3.8). It consists of a quantum detector, which is an array of Mercury Cadmium Telluride (MCT). The detector consists of 320×256 pixels with a spectral response of $7.7 - 9.3 \mu m$ which falls under long wave band discussed previously. The maximum frame rate at full resolution is $250 Hz$. In order to obtain optimal performance and to reduce thermal noise, the sensor is cooled down to $77 K$ by a Stirling Cycle.



Figure 3.8: Cedip IR Camera

The Thermal sensitivity of a detector is measured in terms of Noise Equivalent Temperature Difference (NETD). It is defined as the time standard deviation of the random background noise, spatially averaged over all the pixels of a black body scene (Levesque et al., 2005). It is generally a function of the used black body temperature and is specified in mK by the manufacturer. The CEDIP Titanium 530L owing to its cooling system, has a relatively low NETD of $25mK$ making it very sensitive.

The sensitivity of the camera can be optimised for a particular temperature range by controlling the *Integration Time* which is basically the time duration that the detector is exposed to the incoming radiation for a single measurement. By knowing the required dynamic range of the temperature during the test, the integration time can be set accordingly for the detector to be most sensitive for that temperature range. The integration time was set to be equal to $400 \mu s$ and $205 \mu s$ for the laminar and turbulent interactions reported in this thesis respectively.

As stated earlier, the optics of the camera cannot be made out of conventional materials because of its opacity to IR wavelengths. The CEDIP Titanium 530L is equipped with a special LW 2.0 Jade lens with an average spectral transmissivity of 0.96 making it nearly transparent to the IR wavelength spectrum. A detailed technical specification of both the camera and lens system can be found in Table 3.1.

The Cedip camera is controlled by the *Altair* software which is used to set the acquisition frequency, integration time and the total number of images / duration of the recording. However, before making any measurement, a *non-uniformity correction* (NUC) has to be applied to camera. As stated earlier, the camera consists of 320×256 individual quantum detectors. As a result they suffer from a pixel to pixel gain and offset variation, resulting in a spacial noise called the fixed pattern noise (Orzanowski, 2016). The NUC procedure is carried out to correct for this non-uniformity and to ensure that all pixels deliver the same response. In addition to this, some pixels have extreme or abnormal responsiveness. When uniformly irradiated, measurements from these pixels diverge excessively from the average value and hence are labeled as *bad pixels* (Mudau et al., 2011). A *bad pixel replacement* (BPR) routine is also carried out to eliminate them from the image plane, by taking the weighted averages

Table 3.1: Technical Specification of IR Camera and Lens system

CEDIP Titanium 530L		LW 2.0 Jade	
Property	Value	Property	Value
Detector Material	MCT	Spectral band	7.5 – 10 μm
No. of Pixels	320 \times 266 pixels	Focal length	25 mm
Spectral Response	7.7 – 9.3 μm	F / number	2.0
Max. Frame Rate	250 Hz	FOV	21.7° \times 16.4°
Pitch	30 \times 30 μm	Transmissivity	0.96
NETD	25mK	Focus Range	0.5 - Infinity

of the radiation from the surrounding pixels. Hence, obviously, the only requirement for this routine to work is that the neighbouring pixels shouldn't be a *bad pixel*. Both these processes are carried out by the *Cirrus* software which is integrated with *Altair*.

3.3.5 Calibration Procedure

The Infra-red camera measures the radiation flux that impinges on its sensor. Calibration of the system is essential to map the known radiation flux of the object to its temperature. Modern IR camera are usually equipped with an inbuilt calibration routine to measure the temperature. However, in order to have an accurate estimate of the temperature of the body, taking into account all the environmental variables, accurate re-calibration of the camera is necessary before the experimental campaign. In this section, the calibration procedure described by [Astarita and Carlomagno \(2013\)](#) is summarised and the calibration curves that were generated are discussed.

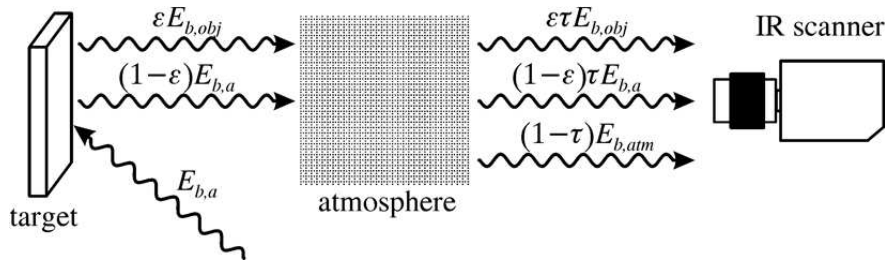
**Figure 3.9:** Radiation detected by the camera ([Astarita and Carlomagno, 2013](#))

Fig.3.9 shows a schematic of the radiation flux detected by the camera. The radiation emitted by the target object has two parts. One part is the radiation emitted by the target owing to its temperature, while another small part is the radiation emitted by the external ambient atmosphere that is reflected off the target object. A third part detected by the camera is the radiation emitted by the atmosphere that is captured by the detector without any reflections off surfaces. All these fractions has to pass through the ambient atmosphere and hence may be attenuated.

Let T_{obj} be the temperature of the target that needs to be measured. The radiation emitted because of the target being at T_{obj} is a fraction, ϵ of a radiation flux emitted by the black body at the same temperature ($E_{b,obj}$). This radiation has to pass through the atmosphere. If the transmissivity of the atmosphere is considered to be equal to τ , then the final portion of this emitted radiation that is collected by the camera detector will be equal to $\epsilon\tau E_{b,obj}$.

The ambient environment can be considered to be at a constant temperature, T_a . Given its large extension with respect to the viewing body, a constant temperature ambience can be considered as a black body emitting a radiation flux, $E_{b,a}$ (Astarita and Carlomagno, 2013). The target body can be assumed to be opaque and hence would possess a reflectivity coefficient equal to $(1 - \epsilon)$. Taking into account the attenuation of this radiation by the ambience on the way to the camera, the fraction of this radiation collected by the detector will be equal to $(1 - \epsilon)\tau E_{b,a}$.

The immediate atmosphere can be considered to be at a constant temperature T_{atm} and with no reflective particles in it, the emissivity would have a value equal to $(1 - \tau)$. Thus the radiation flux that is emitted by the atmosphere and directly reaching the camera sensor would be equal to $(1 - \tau)E_{b,atm}$.

Thus the total radiation that the camera detector detects due to all the sources considered above will be equal to:

$$E_{total} = \epsilon\tau E_{b,obj} + (1 - \epsilon)\tau E_{b,a} + (1 - \tau)E_{b,atm} \quad (3.11)$$

The output signal (IU) of the camera detector is linearly proportional to this radiation and hence, Eqn.3.11 can be written as:

$$IU = \epsilon\tau IU_{obj} + (1 - \epsilon)\tau IU_a + (1 - \tau)IU_{atm} \quad (3.12)$$

Planck's law can be used to approximate the radiation in terms of IU_{obj} to its associated temperature T_{obj} as:

$$IU_{obj} = \frac{R}{e^{\frac{B}{T_{obj}}} - F} \quad (3.13)$$

where, the constants R, B and F are functions of integration time. Using Eqn.3.13 and Eqn.3.12, the temperature of the body can be easily solved:

$$T_{obj} = \frac{B}{\ln \left(\frac{\epsilon\tau R}{IU - (1-\epsilon)\tau IU_a - (1-\tau)IU_{atm}} + F \right)} \quad (3.14)$$

Hence, it can be seen that, in order to have an accurate estimate of the object temperature, the ambient temperature also needs to be recorded with external thermocouples. As previously discussed, for measurements made at short distances, the atmospheric transmissivity can be safely assumed to be equal to one ($\tau = 1$). This reduces Eqn.3.14 to:

$$T_{obj} = \frac{B}{\ln \left(\frac{\epsilon R}{IU - (1-\epsilon)IU_a} + F \right)} \quad (3.15)$$

In order to determine the constants R , B and F , an in-house reference black body simulator was used. Though black bodies were theoretical concepts, a good approximation would be an isothermal cavity with a very small opening (Astarita and Carlomagno, 2013). The schematics of the black body used for calibration is shown in Fig.3.10.

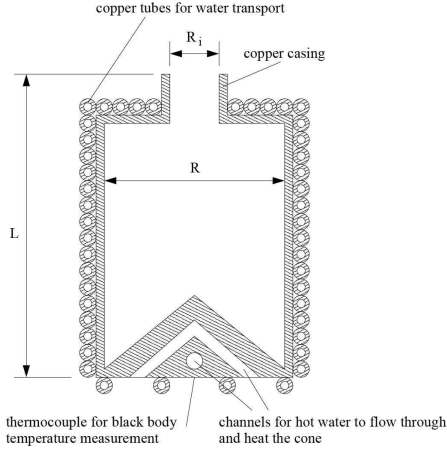


Figure 3.10: Layout of the Black body simulator (Schrijer, 2010)

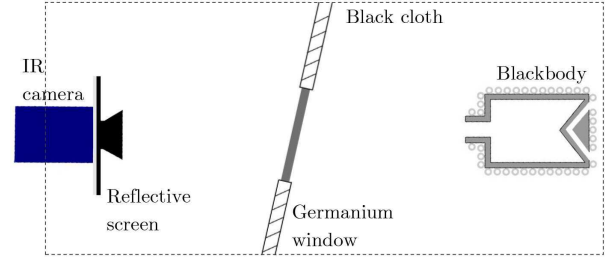


Figure 3.11: Setup of the calibration procedure (Voogt, 2017)

The black body consists of a cylindrical cavity of $R = 25mm$ with a narrow opening in the front ($R_i = 10mm$) and a cone at the back. The cylinder has a total length of $L = 200mm$. The cone shape prevents any direct reflection out of the black body. The inside of the cavity is painted black to increase the emissivity or absorptivity of the walls. The combination of a narrow opening along with the placement of the cone maximises the internal reflection of the radiation, thus increasing absorption making this geometry a near perfect absorber of any radiation entering the cavity. This cylinder is placed inside a wooden box of $350mm \times 280mm \times 250mm$ and filled with glass wool to minimise any heat loss. Kirchoff's law states that a perfect absorber is also a perfect emitter of radiation when heated. Based on the calculations of Mayer (1996), an apparent emissivity of 0.999 can be achieved for this geometry.

A direct correlation between the temperature and the radiation levels can be achieved by considering Eqn.3.15 discussed earlier. For a blackbody, the emissivity is close to one and hence the expression reduces to:

$$T_b = \frac{B}{\ln\left(\frac{R}{IU} + F\right)} \quad (3.16)$$

By changing the blackbody temperature in the range of interest, the digital readings in terms of IU from the camera can be recorded and a non-linear best fit of the n independent data points can be made to determine the calibration constants. A non-linear least-square approach from the Matlab Optimisation toolbox (MathWorks, 2016) was used to reduce the function,

$$\sum_{i=1}^n (T^i - T_b^i)^2 \quad (3.17)$$

thereby evaluating the constants. The calibration set-up is shown in Fig.3.11. The blackbody is heated using a Tamson TLC thermal bath. The temperature controlled water is allowed to flow through the hollow copper coil which is wound around the cavity as shown in Fig.3.10. Three J type thermocouples are placed at the positions corresponding to the inlet of the cavity, centre cone, and exit of the cavity respectively. The isothermal condition is ensured by monitoring the temperatures at these three locations. For all the data points there were recorded, the maximum temperature difference between three points were less than $\Delta T_b \leq 0.4K$. A germanium window ($\tau = 0.96$) which will be used as the optical access for measurements to be taken inside the wind tunnel is also included in the calibration process so that the reduced emissivity measured by the camera is also taken into account. The camera, when placed normally with respect to the black body cavity opening will suffer from unwanted reflections due to Narcissus effect (Lau, 1976) and hence was positioned approximately at an angle of 15° with respect to the germanium window. Finally, since two different facilities were used at different points of time for gathering the data, two different calibration curves are required. The integration times for the two calibration processes were $400\mu m$ and $205\mu m$ for the measures taken for laminar and turbulent interactions respectively. The final calibration curves obtained are shown in Fig.3.12.

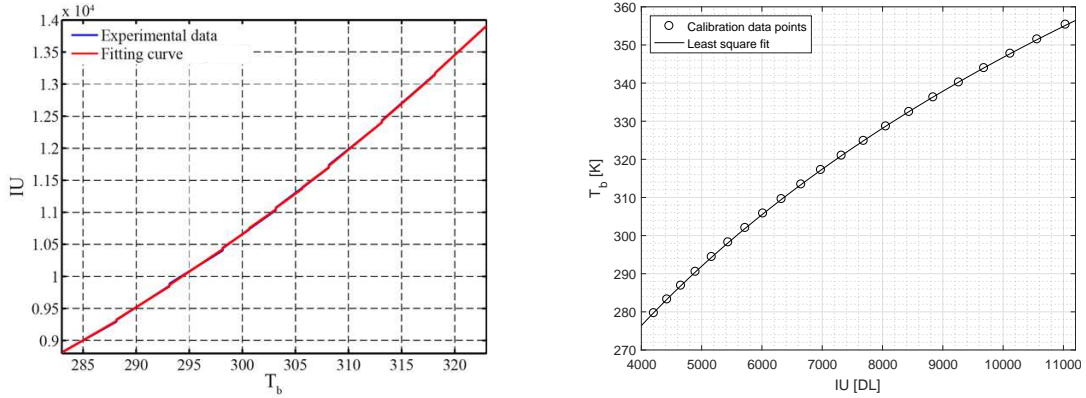


Figure 3.12: QIRT Calibration Curves corresponding to HTFD (left (Avalone, 2015)) and ST15 (right) campaigns

Effect of Ambient Conditions

Once the calibration constants are obtained from the procedure explained in the previous section, it can be substituted back into Eqn.3.15 to obtain the desired object temperature. The equation is again repeated here for convenience.

$$T_{obj} = \frac{B}{\ln \left(\frac{\epsilon R}{IU - (1-\epsilon)IU_a} + F \right)} \quad (3.18)$$

Note that this expression contains an IU_a term, which is part of the radiation due to that ambient environment being at a given temperature T_a . During the first campaign in the Hypersonic Test Facility Delft (HTFD), the ambient temperature was found to vary between 297.15 K and 300.15 K. The percentage error in the object temperature at these two extremities is shown in Fig.3.13

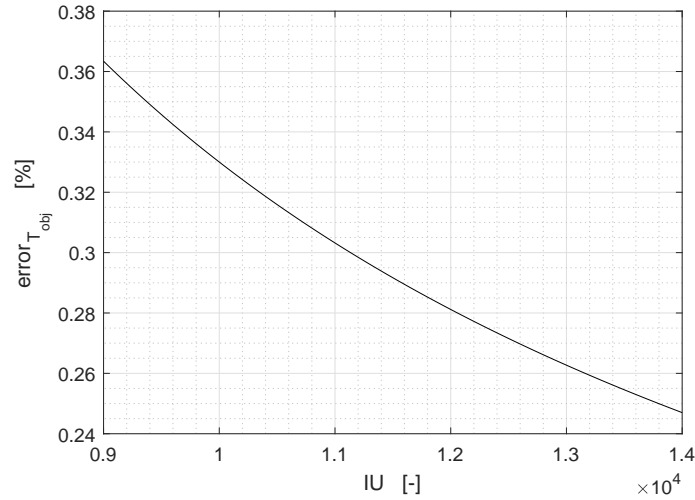


Figure 3.13: Error in Temperature estimates due fluctuations in ambient conditions

As can be seen in the figure, for the entire range of incoming radiation that would fall on the sensor, the error due to fluctuations in atmospheric temperature was found to be less than 0.35%. Hence, for simplicity, this effect was safely neglected for the measurements taken from ST-15.

3.4 Image Resection and Direct Linear Transformation

For all the experimental techniques discussed above, a digital camera forms an integral part of the measurement. While the property measured by the individual systems may differ (Light Intensity in case of Schlieren and Oil Flow and Radiation/Temperature in case of QIRT), all the resulting images require accurate mapping of the coordinates of each individual pixels onto its real world counterparts. Counting the individual pixels between two points in real space may not work since the objects in the real world are three dimensional in nature while the image space in terms of pixels is only two dimensional in nature. To accurately map the objects on the real space to the image space, the principle of photogrammetry was used. This involves modelling and calibrating the camera to determine the camera intrinsic and extrinsic parameters. Of the numerous techniques proposed in literature, a Direct Linear Transformation (DLT) technique developed by [Abdel-Aziz and Karara \(1971\)](#) yields the best results with the least complexity ([Chen et al., 1994](#)) and hence the same was used in this thesis to enable object to image coordinate transformation.

Consider a point O, given by the coordinates $[x, y, z]$ in the object space as shown in Fig.3.14, where N is the projection centre of the camera. The corresponding point in the image space can be given by the coordinates, $[u, v]$. All the objects that requires transformation in this thesis are 2D planar flat plates or sections. Though it is a 2D - 2D mapping, application of direct linear transformation will correct for any oblique angle viewing and de-warps the image irrespective of its orientation. According to [Abdel-Aziz and Karara \(1971\)](#), the relationship between the object and image coordinate system is given by:

$$u = \frac{L_1x + L_2y + L_3}{L_7x + L_8y + 1} \quad (3.19)$$

$$v = \frac{L_4x + L_5y + L_6}{L_7x + L_8y + 1} \quad (3.20)$$

where, $[L_1, L_2, \dots, L_8]$ are the DLT parameters which are functions of the camera intrinsic and extrinsic parameters. This eliminates the need to determine the parameters individually, making this approach very appealing.

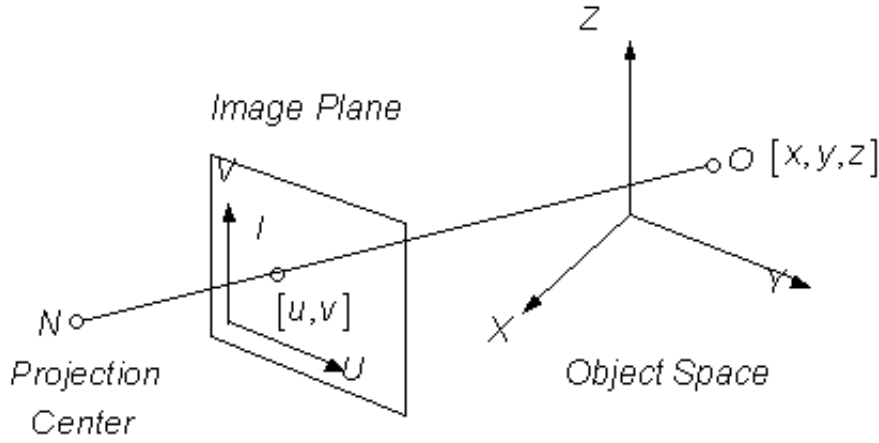


Figure 3.14: Object and Image coordinate system (Goktepe and Kocaman, 2010)

The DLT parameters can be estimated by rewriting Eqns 3.19 and 3.20 for atleast 4 known points in the object and the image space. If u_i and v_i correspond to the points, x_i and y_i , then we have:

$$\frac{1}{R_i} \begin{bmatrix} u_i \\ v_i \end{bmatrix} = \frac{1}{R_i} \begin{bmatrix} x_i & y_i & 1 & 0 & 0 & 0 & -x_i u_i & -y_i u_i \\ 0 & 0 & 0 & x_i & y_i & 1 & -x_i v_i & -y_i v_i \end{bmatrix} [\mathbf{L}] \quad (3.21)$$

where, $\mathbf{L} = [L_1, L_2, \dots, L_8]^T$ and $R_i = L_7x_i + L_8y_i + 1$. The DLT parameters can be estimated by solving for \mathbf{L} from Eqn.3.21. Once the parameters are calculated, Eqns 3.19 and 3.20 can now be re-written to obtain the object coordinates from the other unknowns as follows:

$$\frac{1}{R_i} \begin{bmatrix} u_i L_7 - L_1 & u_i L_8 - L_2 \\ v_i L_7 - L_4 & v_i L_8 - L_5 \end{bmatrix} \begin{bmatrix} x_i \\ y_i \end{bmatrix} = \frac{1}{R_i} \begin{bmatrix} L_3 - u_i \\ L_6 - v_i \end{bmatrix} \quad (3.22)$$

Specifying the pixel coordinates (u_i, v_i) and the calculated DLT parameters, Eqn.3.22 can be solved to determine the corresponding real world coordinates (x_i, y_i) . A calibration target was used for all the campaigns to record images with known co-ordinates from which the corresponding DLT parameters were estimated. This is then utilised to reconstruct and de-warp all the images measured during that campaign.

For the QIRT campaign in HTFD, a slotted aluminium plate flat plate was used as the calibration target and the effect of oblique angle viewing and the corresponding reconstructed image can be seen in Fig.3.15.

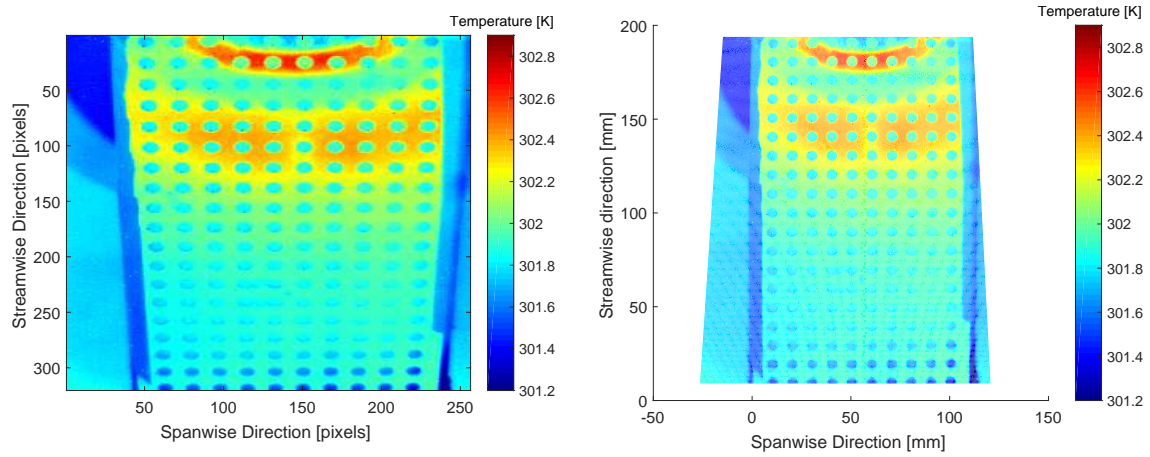


Figure 3.15: Calibration target before (left) and after (right) the application of Direct Linear Transformation

Part I

Effect of a Surface Protuberance in an Incoming Laminar Boundary Layer

Chapter 4

Experimental Setup and Data Reduction Technique

In this part of the thesis, the experiments conducted to investigate the interaction of a cylinder with a laminar boundary layer will be discussed. The measurements reported here were taken in the Hypersonic Test Facility Delft (HTFD) situated at the High Speed Laboratory of the Faculty of Aerospace Engineering. The flow facility and the associated free stream properties will be discussed in Section 4.1. Since the walls of the tunnel are turbulent in nature, new flat plate set-up has to be manufactured. The wind tunnel model used here was designed by [Avalone \(2015\)](#) and manufactured in-house. A description of the model used can be found in Section 4.2. Finally the data reduction technique used to calculate the heat flux is discussed in Section 4.3

4.1 The Hypersonic Test Facility Delft (HTFD)

The Hypersonic Test Facility Delft ([Schrijer and Bannink, 2010](#)) is a cold hypersonic facility based on the Ludwig tube concept ([Ludwig, 1955](#)), capable of producing high Reynolds number at low cost. The Ludwig tube concept is particularly appealing, owing to its relatively long duration time ($0.1s-0.2s$) compared to other short duration tunnels at a high free stream unit Reynolds number ($5-50 \times 10^6 / m$) ([Schrijer, 2010](#)). It was designed and manufactured by Hyperschall Technologie Göttingen (HTD). The various parts of the HTFD currently residing in the High Speed Laboratory of the Faculty of Aerospace Engineering can be seen in Fig.4.1.

4.1.1 Operating Principle

The principle elements of the HTFD are

- Storage tube, where air is stored at high pressure high temperature condition.
- A fast acting valve separates the storage tube from the rest of the tunnel. The tunnel

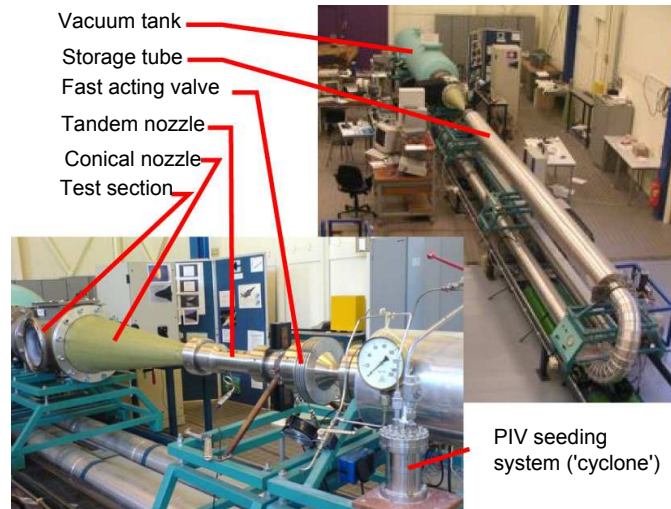


Figure 4.1: The Hypersonic Test Facility Delft (redrawn from Schrijer and Bannink (2010))

is armed and fired by actuating the valve.

- A convergent-divergent nozzle accelerates the fluid from the storage tube to reach the desired conditions in the test section. The expansion ratio determines the free stream Mach number in the test section.
- The test section, where the desired measurements are made. Optical access is made available in three sides of the test section.
- Vacuum Tank, where the flow is discharged. It sustains a very low pressure which is essential to have the desired flow conditions.

The tunnel is fired by actuating the fast acting valve. The valve opens very quickly and hence the expansion wave travelling upstream can be considered as a centred expansion wave (Wolf et al., 2007) as seen in Fig.4.2.

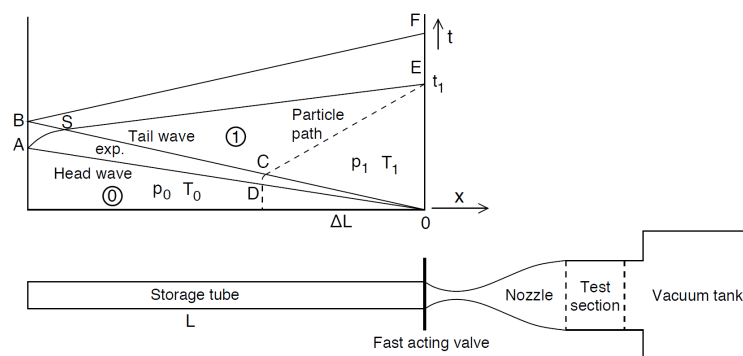


Figure 4.2: Operating Principle of the HTFD (redrawn from Schrijer and Bannink (2010))

The first and the last characteristic expansion waves are denote by OA and OSB respectively. Once they reach the end of the storage tube, they reflect back towards the fast acting valve through the path AE and BF. Constant storage tube condition are maintained until the reflected expansion wave reach the fast acting valve and hence this time corresponds to the testing time of the facility. Using simple wave theory, [Schrijer and Bannink \(2010\)](#) were able to derive the relations to determine the conditions in the storage tube which enabled them to determine the wind tunnel run time through the expression:

$$t_{test} = \frac{L}{a_0} \frac{2}{M_1 + 1} \left(1 + \frac{\gamma - 1}{2} M_1^2 \right)^{\frac{\gamma+1}{2(\gamma-1)}} \quad (4.1)$$

where, the subscripts 0 and 1 denote the condition upstream and downstream of the centered expansion waves respectively, M is the Mach number and a speed of sound based on local conditions, γ is the specific heat ratio and L is the length of the storage tube. The Mach number, M_1 is determined by ratio of the storage tube diameter (d_{tube}) to the diameter of the first throat (d^*) given by the following relation.

$$\left(\frac{d_{tube}}{d^*} \right)^2 = \frac{1}{M_1} \left[\frac{2}{\gamma + 1} \left(1 + \frac{\gamma - 1}{2} M_1^2 \right) \right]^{\frac{\gamma+1}{2(\gamma-1)}} \quad (4.2)$$

For a free-stream Mach number less than 9, a tandem nozzle set-up is used where the Mach 9 nozzle is used as the first (throat) nozzle and an appropriate second nozzle (throat) is then used. The Mach 9 nozzle determines the stagnation conditions for the second nozzle. Substituting $d_{tube} = 48.25mm$ and $d^* = 19.35mm$ for the Mach 9 nozzle configuration yield $M_1 = 0.09$. This is then utilised to calculate the run time of the tunnel, $t_{test} \approx 100ms$.

A low static temperature will be reached in the test section of the HTFD, due to the expansion of air. Hence, to avoid any possible condensation effects, the air in the storage tube is heated prior to its operation ([Schrijer and Bannink, 2010](#)). However, as the HTFD is designed to be cost effective during its operation, only a part of the storage tube is heated. This length (ΔL) can be computed by considering the most upstream particle that may enter the test section during the run time of the tunnel. [Schrijer and Bannink \(2010\)](#) provide a relation considering the particle path DCE in Fig.4.2 as follows.

$$\Delta L = M_1 \frac{a_1 - u_1}{a_0} 2L \quad (4.3)$$

For the total length of the storage tube, $L = 29m$, the length of the most upstream particle would be $\Delta L = 5.2m$. Hence, only the first six metres of the storage tube is heated to avoid any issues related to condensation in the free stream. The temperature in the hot section is heated to a maximum of $T_{hot} = 773K$, limited by safety regulations. Due to the temperature difference between the heated and the non-heated parts of the storage tube, reflection of the expansion waves would occur. The effect of this was reduced by [Schrijer and Bannink \(2010\)](#) by setting an appropriate temperature to the cold section of the tube, given by the tube cross sections as follows:

$$\frac{d_{hot}}{d_{cold}} = \left(\frac{T_{cold}}{T_{hot}} \right)^{\frac{1}{4}} \quad (4.4)$$

Based on the known values, the temperature of the cold tube was hence set to $T_{cold} = 375K$ as estimated by Eqn.4.4. Due to the high temperatures involved here, it is essential to study the effects of high temperature on the flow field, especially since the specific heat ratio (γ) may not be constant. However, [Schrijer and Bannink \(2010\)](#) argue that the decrease in the value of γ for the temperature range in the storage tube is relatively small from $\gamma = 1.4$ and hence, the medium can be considered calorically perfect. The error in the free stream quantities, when γ is assumed to be a constant value of 1.4 for a Mach 7 flow field is given in Table 4.1.

Table 4.1: Error in Free stream quantities when $\gamma = 1.4$ ([Schrijer and Bannink, 2010](#))

M	ϵ_M	ϵ_u	ϵ_T	ϵ_p	ϵ_ρ
7	-0.5%	1.1%	3.1%	1.1%	-2.0%

4.1.2 Tandem Nozzle

The HTFD was designed to operate at a range of Mach numbers. For $M > 9$, the first throat section is attached directly to the 15° conical nozzle. But, for small Mach numbers, a second throat is essential. Fig.4.3 shows the tandem nozzle configuration. The two throats are separated by a settling chamber. The first nozzle accelerates the flow to supersonic velocity, where it is slowed down by a normal shock wave. The conditions downstream of the normal shock forms the stagnation conditions of the second throat, which then accelerates the flow to the desired Mach number in the test section.

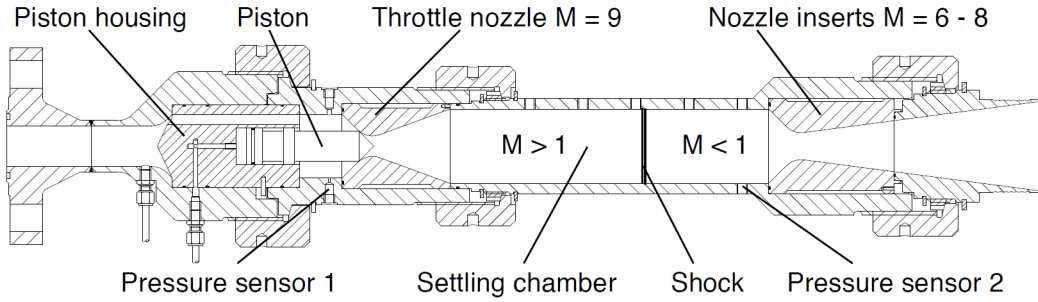


Figure 4.3: HTFD Tandem nozzle configuration (redrawn from [Schrijer and Bannink \(2010\)](#))

The shock in the settling chamber results in a total pressure loss, which is determined by the expression:

$$\frac{p_{t,2}}{p_{t,1}} = \left(\frac{d_1^*}{d_2^*} \right)^2 \quad (4.5)$$

where, $p_{t,1}$ is the total pressure in the storage tube (downstream of the expansion wave) and $p_{t,2}$ is the total pressure in the free stream. Pressure measurement taken by [Schrijer and Bannink \(2010\)](#) revealed that the pressure ratio is only slightly lower than that what the theory predicted. Downstream of the throat, the nozzle conical section has a length of $1.18m$

for the Mach 7 nozzle. The free stream Mach number is determined by the area ratio of the nozzle. However, since the nozzle wall is subjected to a thick boundary layer, corrections have to be made. Planar PIV measurements carried out by [Schrijer and Bannink \(2010\)](#) revealed a boundary layer displacement thickness of $\delta^* = 11\text{mm}$. This effective reduction in the area ratio results in a Mach number reduction from 7 to 6.7.

4.1.3 Free stream assessment and operation envelope

The flow entering the test section continues to diverge and expand due to the outflow from the conical nozzle. Hence the Mach number obtained in the free stream will be higher than what's predicted by the area ratio. After correcting for the boundary layer displacement thickness, the Mach number in the free stream is computed to be equal to 7.5. The discontinuity between the nozzle and the test section walls also induces shock waves, with a shock angle of $\theta = 14^\circ$ with respect to the free stream. The vertical velocity components from the stereo-PIV measurements of ([Schrijer and Bannink, 2010](#)) in the test section is shown in Fig.4.4 where shock wave and the diverging flow are clearly seen. Assessment made from the PIV information reveal the presence of an undisturbed region of $200 \times 200\text{mm}^2$ with a free stream stream wise velocity equals to 1033m/s .

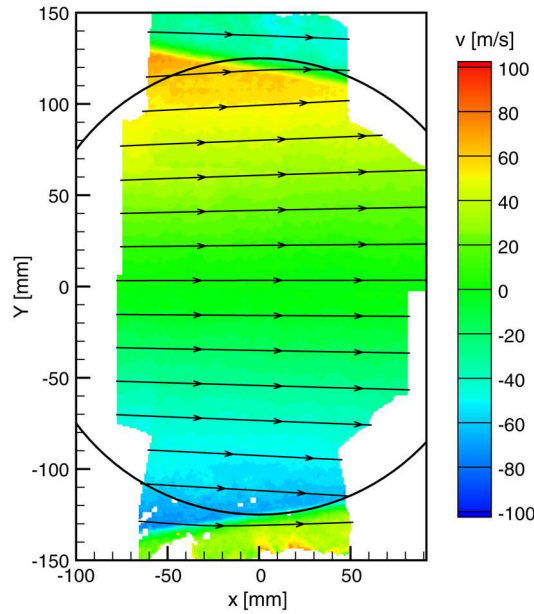


Figure 4.4: Vertical velocity components in the free-stream of Mach 7 configuration. The circle portray the outline of the optical access (redrawn from [Schrijer and Bannink \(2010\)](#))

The free stream total and static temperatures can now directly be determined by the known values of Mach number and free stream velocity as follows:

$$T = \frac{(|V|M)^2}{\gamma R} \quad (4.6)$$

where, R is the specific gas constant and for dry air equal to $R = 287\text{JKg}^{-1}\text{K}^{-1}$. The total

temperature is given by,

$$T_t = T + \frac{|V|^2}{2c_p} \quad (4.7)$$

A significant discrepancy was observed between the calculated and measured total temperatures. This discrepancy is attributed to the heat transfer loss in the fast acting valve and the tandem nozzle. Pressure measurements made by (Schrijer and Bannink, 2010) also show good agreement with theory. The unit Reynolds number can now be determined, knowing the measured free stream static pressure and temperature, and the density and viscosity determined by Ideal gas law and Sutherland's law of viscosity respectively. The free-stream properties of a Mach 7 nozzle configuration is summarised in Table 4.2.

Table 4.2: Free stream quantities for a Mach 7 configuration

Velocity	$ V = 1033m/s$
Mach	$M = 7.5$
Static Temperature	$T = 47K$
Total Temperature	$T_t = 579K$
Total enthalpy	$H_0 = 0.56MJ/Kg$

4.2 Wind Tunnel Model

Since the boundary layer in the walls of the HTFD are turbulent in nature, a new wind tunnel model was designed and manufactured by Avallone (2015). The resulting design was a 5° ramp which is $200mm$ long and $110mm$ wide and is installed into the centre of the test section using a sting from the rear (see Fig.4.5). It is made of Makrolon[®], a polycarbonate material characterised by a relatively low thermal conductivity ($k = 0.20W/mK$) and a high surface emissivity ($\epsilon = 0.88$). These properties makes the material very suitable for Infrared Thermographic applications. In addition to this, the material can withstand a temperature upto $393K$ without any considerable change in its properties (Avallone et al., 2016b), which is much higher than the highest temperature achieved during the run. The model was placed at an angle of attack of zero, which respect to the centre of the wind tunnel, with an uncertainty of approximately $\pm 3^\circ$. The leading edge of the wedge was accurately finished with a radius of $50\mu m$ to prevent any possible leading edge instabilities, so that a fresh laminar boundary layer develops over it.

The roughness elements used in this study all have a height of $H = 2mm$. They are cylindrical shapes, having diameter equal to $D = 4mm$, $D = 5.7mm$, $D = 8mm$ and $D = 11.2mm$ and will be labelled as D4, D5.7, D8, and D11.2 respectively for the remainder of this part of the thesis. (Fig.4.6).

The roughness elements are mounted at a distance of $x_r = 60mm$ from the flat plate leading edge and right at the centre of the model. The global coordinate system, x and y are based on the dimensions of the flat plate, with x ranging $0mm \leq x \leq 200mm$ along the length of the plate and y ranging between $-55mm \leq y \leq 55mm$ along the span of the plate. However,

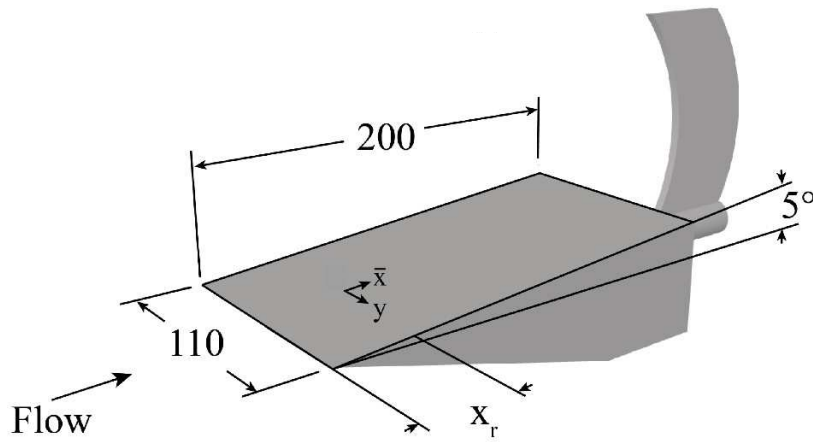


Figure 4.5: 5° ramp model (Avallone et al., 2016b)

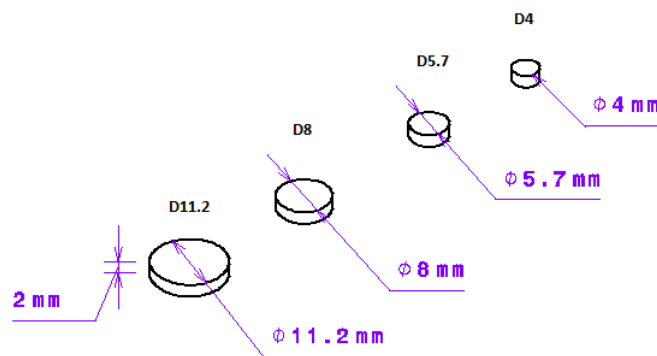


Figure 4.6: Geometry of the Roughness elements

two separate non-dimensionalised coordinate systems are defined with respect to the element, the application for which depends on the particular investigation. The coordinates of all 2D figures of the heat flux distribution around the element, is scaled with height and have their origin at the centre of the element as shown in Fig.4.7. The non-dimensionalised coordinates, \bar{x} and \bar{y} are given by:

$$\bar{x} = \frac{x - x_r}{H} \quad \bar{y} = \frac{y}{H} \quad (4.8)$$

In Eqn.4.8, $x_r = 60\text{mm}$ is the distance from the leading edge of the model and on its centreline, where the cylinder was placed. A second coordinate system, x^* and y^* is also shown in Fig.4.7, where the origin is now shifted to the trailing edge of the cylinder and is hence specific to the geometry of the cylinder. This particular coordinate system will be useful when studying and comparing the wake development behind the cylinders of different geometries. The second non-dimensionalised coordinate are given by:

$$x^* = \frac{x - (x_r + D/2)}{H} \quad y^* = \frac{y}{D} \quad (4.9)$$

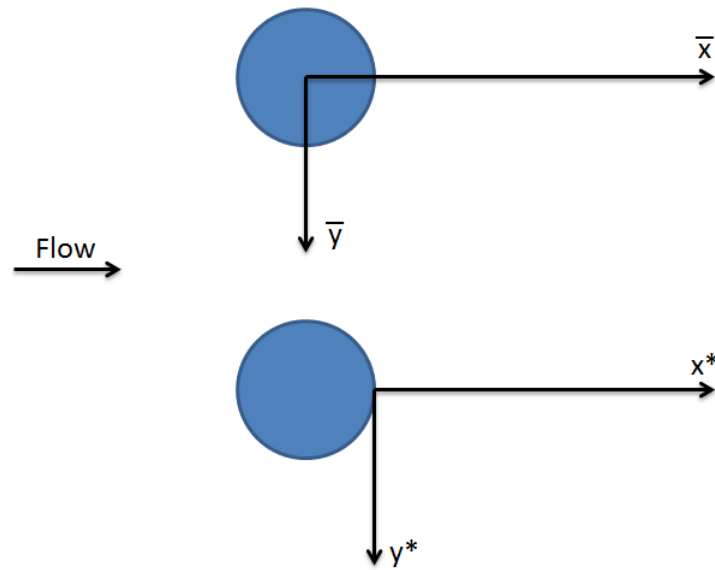


Figure 4.7: Definition of coordinate system

For the measurement acquired from HTFD in this thesis, the Mach 7 nozzle was used and the results reported in this section of the thesis correspond to three different Reynolds number. Since the total temperature and Mach number are fixed quantities, the Reynolds number is changed by changing the total pressure in the storage tube. An unit Reynolds number of $8 \times 10^6 \text{ m}^{-1}$, $11 \times 10^6 \text{ m}^{-1}$, $14 \times 10^6 \text{ m}^{-1}$ were calculated downstream of the leading edge shock, for the freestream total pressure of 1.7 MPa , 2.2 MPa and 2.8 MPa respectively. The results corresponding to these three conditions will hence be labelled as Re8, Re11 and Re14 respectively in the increasing order of Reynolds number.

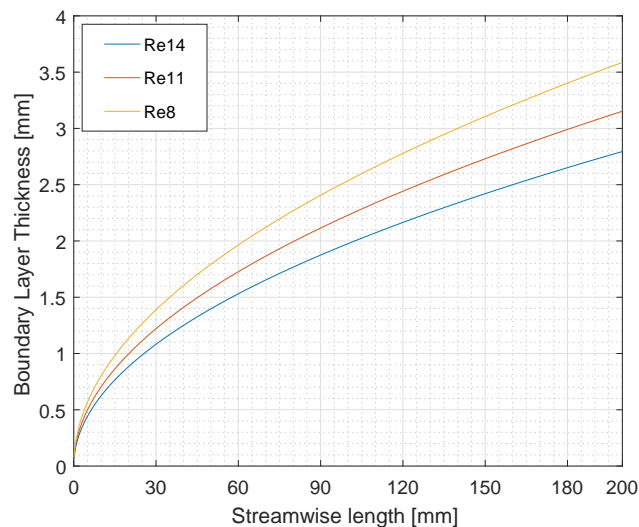


Figure 4.8: Boundary Layer profile calculated using Illingworth Transformation

The undisturbed laminar boundary layer properties also needs to be evaluated at the location of the roughness element ($x_r = 60mm$), for which the Blasius equation using Illingworth transformation is solved using the ‘shooting’ technique (Anderson Jr, 2006). The resulting boundary layer profile for the three Reynolds number can be seen in Fig.4.8. The other local properties evaluated at the location of the roughness element include the momentum thickness (θ), displacement thickness (δ^*), Reynolds number based on the boundary layer edge conditions and momentum thickness (Re_θ), roughness height based Reynolds number (Re_H) and the ratio of roughness height to local boundary layer height (H/δ). A summary of the free stream conditions and the boundary layer properties at the position of the roughness element can be found in Table 4.3, while Table 4.4 provides a summary of the geometrical details of the elements. Each of the four roughness elements were installed onto the ramp model and tested at three different Reynolds number resulting in 12 test cases which was used to make a comparative study later in this part of the investigation.

Table 4.3: Experimental Condition and Laminar Boundary Layer Properties

Parameter	Re8	Re11	Re14
M_∞	7.5		
U_∞ [m/s]	1030		
T_0 [K]	579		
P_0 [MPa]	1.7	2.2	2.8
Re [m^{-1}]	8×10^6	11×10^6	14×10^6
x_r [mm]	60	60	60
δ_{99} [mm]	2	1.7	1.5
θ [mm]	0.24	0.21	0.18
δ^* [mm]	0.62	0.54	0.47
Re_θ	1920	2310	2520
Re_H	16000	22000	28000
H/δ	1	1.17	1.33

Table 4.4: Roughness Element Geometry

	Height (H) [mm]	Diameter (D) [mm]
D4	2	4
D5.7	2	5.7
D8	2	8
D11.2	2	11.2

4.3 QIRT Data Reduction

For a typical heat flux measurements, the temperature difference between the model and the wind tunnel flow is used as the driving potential. An appropriate physical model can then be applied to determine the convective heat flux (Carlomagno and Cardone, 2010). The data reduction procedure to estimate the convective heat transfer was categorised into one of the three classes by Walker and Scott (1998). The first class belongs to analytical techniques which utilised a closed form solution to the conduction equation. The second class belongs to Direct numerical techniques, which offer more flexibility with their ability to consider materials of different thermal properties. The third class consists of inverse heat conduction procedures based on least square minimization which the authors argue to be robust and stable and can be extended to multidimensional problems. However this results in increased complexity and computational cost (Avallone et al., 2015). In addition to that, many applications which make use 1D heat equation can affect accuracy especially in case of high spacial gradients. However, because of the use of Makrolon[®] and owing to its favourable thermal properties, the use of 1D analytical techniques can be justified.

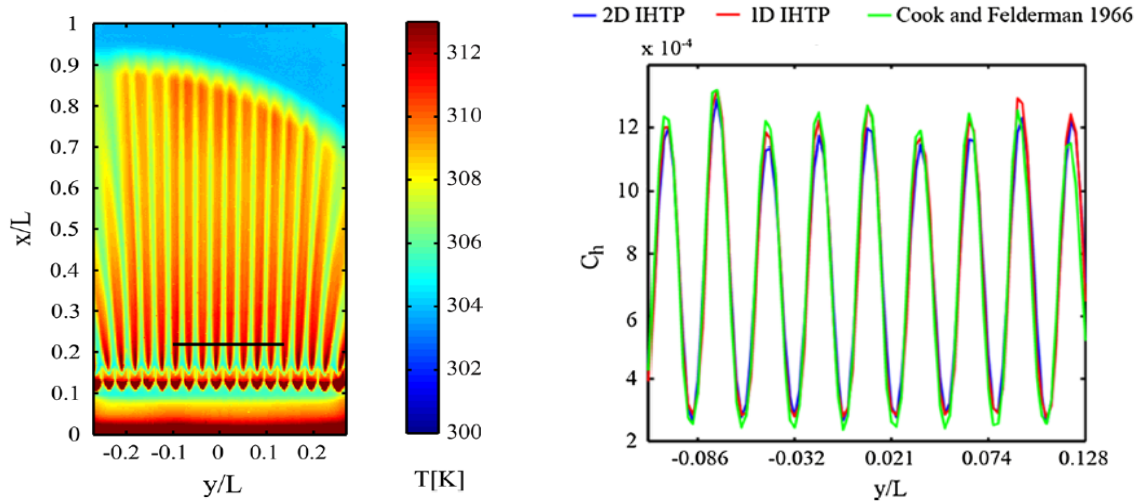


Figure 4.9: Temperature map (left) and span wise Stanton number variation on the black line calculated using different data reduction procedures (Avallone et al., 2015)

Avallone et al. (2015) performed heat transfer measurements using the same model and test facility under the same conditions (unit $Re = 14 \times 10^6 m^{-1}$). In order to develop stream wise vortices which would have large span wise temperature gradients, they place zigzag strips at a distance of $x_r = 30mm$ from the leading edge of the model. The resulting heat flux was non-dimensionalised using the modified Stanton number (C_h , more details on this can be found in Section 4.3.3). The temperature distribution thus obtained and the results of the various methods used to estimate the modified Stanton number can be seen in Fig.4.9.

As can be seen from the temperature map, the placement of zig zag strips has produced strong gradients in the span wise direction. Thus based on the arguments stated by various authors, this should have a large error in the convective heat flux estimates. However, because of the favourable thermal properties of Makrolon[®], the heat flux estimated by various methods (see

Fig.4.9) do not show any significant variation. The difference between various methods was calculated to be less than 2%. Based on these results, for this thesis, the simplest **Cook and Felderman (1966)** technique, applied onto a 1D semi infinite model was used for heat flux data reduction.

4.3.1 1D - Semi Infinite Model

For any short duration facility, the response time of any instrumentation used should be very fast. The model used will never have enough time to attain thermal equilibrium and hence we are limited by the transient heat response of the model surface due to the energetic air passing over it to calculate the heat transfer properties (**Arts and Camci, 1985**). The heat flux data reduction technique used in this part of the thesis is based on the one dimensional semi infinite model. The 1D heat conduction equation is applied on to the model surface through which the surface heat flux ($q_s(t)$) can be related to the transient surface temperature response. It is given by:

$$\frac{\partial T(y, t)}{\partial t} = \frac{k}{\rho c} \frac{\partial^2 T(y, t)}{\partial y^2} \quad (4.10)$$

where, the boundary conditions can be given by,

$$-k \frac{\partial T(0, t)}{\partial y} = q_s(t) \quad (4.11)$$

$$T(y, 0) = T_i \quad (4.12)$$

$$T(\infty, t) = T_i \quad (4.13)$$

where, T_i is the initial temperature, k is the thermal conductivity and c is the heat capacity of the wall. A solution to Eqn.4.10 corresponding to the boundary condition will provide the

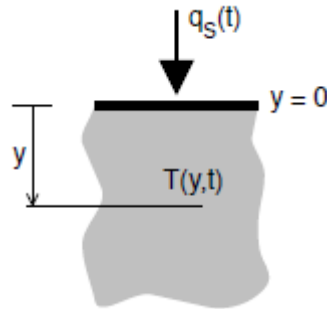


Figure 4.10: 1D semi-infinite model (**Schrijer, 2010**)

distribution of temperature as function of time, including the surface temperature. However, the surface transient temperature profile has already been measured by the IR camera and the unknown which is desired is the transient heat flux $q_s(t)$. This approach is known as the inverse problem, for which, the general solution for heat flux is given by **Schultz and Jones**

(1973) as:

$$q_s(t) = \sqrt{\frac{\rho ck}{\pi}} \int_0^t \frac{dT_s(\tau)}{\sqrt{t-\tau}} d\tau \quad (4.14)$$

Integrating this equation by parts with the boundary condition $T(\tau) = 0$ at $\tau = 0$, the heat flux can be directly related to the surface temperature by:

$$q_s(t) = \sqrt{\frac{\rho ck}{\pi}} \left[\frac{T_s(t) - T_{iw}}{\sqrt{t}} + \frac{1}{2} \int_0^t \frac{T_s(t) - T_s(\tau)}{(t-\tau)^{3/2}} d\tau \right] \quad (4.15)$$

where, T_{iw} is the initial wall temperature equal to $T_s(0)$. This equation successfully relates the transient heat flux to the surface temperature evolution with time. A more convenient form would be to write $\phi(t) = T_s(t) - T_s(0)$ such that Eqn.4.15 reduces to:

$$q_s(t) = \sqrt{\frac{\rho ck}{\pi}} \left[\frac{\phi(t)}{\sqrt{t}} + \int_0^t \frac{\phi(t) - \phi(\tau)}{(t-\tau)^{3/2}} d\tau \right] \quad (4.16)$$

4.3.2 Cook and Felderman Technique

While Eqn.4.16 provides the necessary relationship to calculate the transient heat flux, it poses a problem at $t = \tau$ where the integral tends towards infinity. Thus the application of any approximate numerical integration technique like the Simpson's or Trapezoidal becomes impossible. This problem was tackled by [Cook and Felderman \(1966\)](#), who provided a method by approximating $\phi(\tau)$ by a piecewise linear function of the form:

$$\bar{\phi}(\tau) = \phi(t_{i-1}) + \frac{\phi(t_i) - \phi(t_{i-1})}{\Delta t} (\tau - t_{i-1}) \quad (4.17)$$

with, $t_{i-1} \leq \tau \leq t_i$ and $i = 1, 2, 3, \dots, n$. Substituting this equation into Eqn.4.16 and after some mathematical operations (details of which can be found in [Schultz and Jones \(1973\)](#)), we get:

$$q_s(t_n) = \sqrt{\frac{\rho ck}{\pi}} \left[\frac{\phi(t)}{\sqrt{t}} + \sum_{i=1}^{n-1} \left\{ \frac{\phi(t_n) - \phi(t_i)}{(t_n - t_i)^{1/2}} - \frac{\phi(t_n) - \phi(t_{i-1})}{(t_n - t_{i-1})^{1/2}} \dots \right. \right. \\ \left. \left. \dots + 2 \frac{\phi(t_i) - \phi(t_{i-1})}{(t_n - t_i)^{1/2} + (t_n - t_{i-1})^{1/2}} \right\} + \frac{\phi(t_n) - \phi(t_{n-1})}{\sqrt{\Delta t}} \right] \quad (4.18)$$

Validation

In order to validate the implementation of this code into Matlab, a constant heat flux case can be assumed. If $q_s(t) = \text{constant}$ applied at $\tau = 0$, Eqn.4.15 reduced to the exact analytical expression:

$$T_s - T_{iw} = \frac{2q_s}{\sqrt{\pi}} \sqrt{\frac{t}{\rho ck}} \quad (4.19)$$

So, once the Matlab script to calculate the heat flux was written, it was tested against this constant heat flux case. The temperature profile needed was generated assuming an initial constant heat flux of $Q = 10MW/m^2$. The temperature profile thus obtained was proportional to the square root of time and is fed as input to the Cook and Felderman script. The heat flux calculated by the script matched exactly the initial heat flux assumption as can be seen in Fig.4.11.

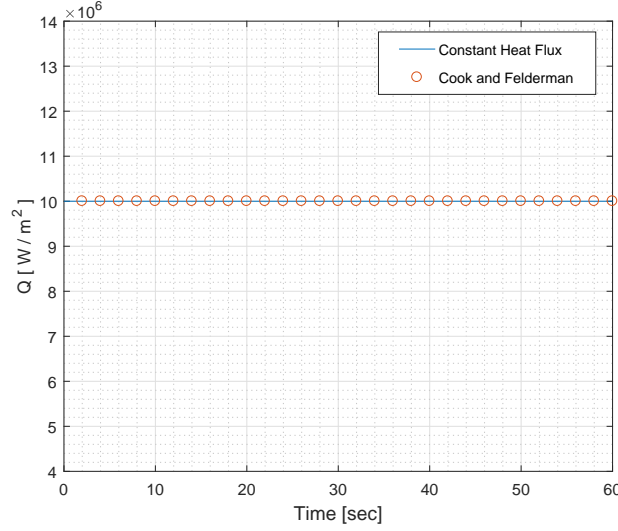


Figure 4.11: Validation of Cook and Felderman (1966) script

4.3.3 Heat Flux normalisation

The surface heat flux obtained by the Cook and Felderman (1966) technique can be non-dimensionalised using the Stanton number, defined as:

$$St = \frac{q_s}{c_p \rho_e u_e (T_{aw} - T_w)} \quad (4.20)$$

where, the parameters c_p , ρ_e and u_e correspond to the specific heat at constant pressure, density and velocity evaluated at the boundary layer edge properties respectively. In a short duration facility like the HTFD, the adiabatic wall temperature (T_{aw}) cannot be accurately measured and hence it is a common practise among researchers to adopt the modified Stanton number (C_h) by replacing T_{aw} in Eqn.4.20 with the total temperature (T_0).

$$C_h = \frac{q_s}{c_p \rho_e u_e (T_0 - T_w)} \quad (4.21)$$

While the Stanton number or the modified Stanton number signifies the absolute value of heat flux, sometimes it can be useful to normalise the convective heat flux that was measured with the local laminar heat flux at that position. This would provide a direct idea of the level of perturbation that the flow undergoes from the otherwise laminar state. The resulting normalised heat flux (q^*) can be given by:

$$q^* = \frac{q_s}{q_{laminar}} \quad (4.22)$$

where $q_{laminar}$ can be obtained by using the Reference Temperature method.

4.4 Experimental Configuration

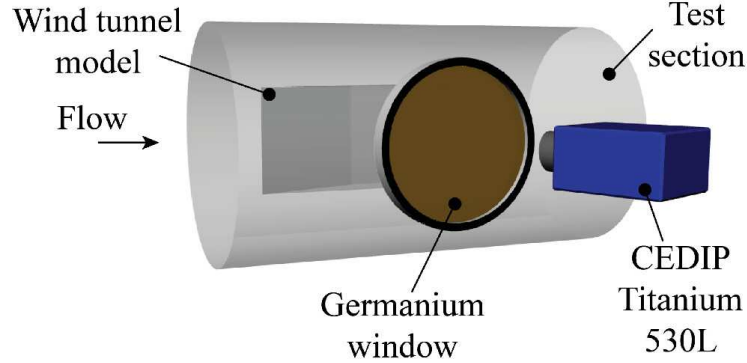


Figure 4.12: HTFD Experimental Setup (Avallone et al., 2016b)

Now that the wind tunnel models and the heat transfer data reduction techniques are discussed and established, the actual experimental procedure can be discussed. The CEDIP camera after calibration was placed in front of the test section of the HTFD. The optical access was provided by the Germanium window, which was earlier included in the calibration. As stated previously, the sensor of the camera was designed to cool down to a very low temperature to reduce thermal noise. Thus, when the camera is placed normal to the window, it will suffer from unwanted reflections off the Germanium window (Narcissus effect). To avoid this, the camera is placed at an angle of 15 degrees with respect to the window (Fig.4.12) and the distorted image was corrected and de-warped later using Direct Linear Transformation. The resolution of the camera depends on its distance from the model surface. On average, the resolution of the camera for this setup was equal to 1.79 px / mm.

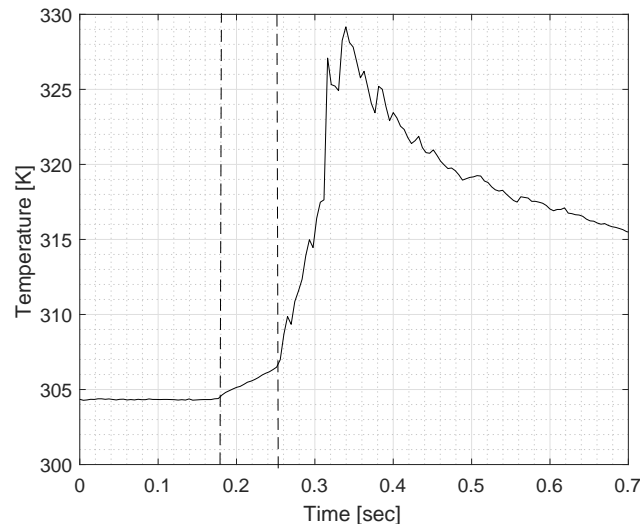


Figure 4.13: Transient Temperature response during a typical wind tunnel run

The data is collected at an acquisition frequency of 218Hz . A typical temperature evolution on a single pixel is shown in Fig.4.13. The region between the dotted lines correspond

to the wind tunnel run, which is approximately 0.07 seconds long and for this acquisition frequency, approximately 15 frames are considered to calculate the transient heat flux. The temperature calculated before the start of the wind tunnel run will correspond to the initial surface temperature necessary for the [Cook and Felderman \(1966\)](#) technique. The heat flux thus obtained is non-dimensionalised using the modified Stanton number described earlier.

A peak heating can be observed in the figure, after the end of the wind tunnel run. This peak heating in the image is caused because of the slow moving hot air after the closing of the valve, that passed over the model surface. The surface heats up because of this and also then gradually starts to cool down.

4.5 Error Sources

It was already observed in Section 4.3 that due to the adaptation of [Cook and Felderman \(1966\)](#) technique, data reduction scheme could result in an error of 2%. In addition to that, other possible error sources should also be identified to understanding the limitation of the results that will be presented in the next chapter.

One error source can correspond to the usage of Direct Linear Transformation for de warping the image. The DLT method, though accurate can result in some calibration or reconstruction error which can be associated to the deviation of the co-ordinates of the measured and reconstructed points.

$$\epsilon_{DLT,x} = x_m - x_i \quad (4.23)$$

$$\epsilon_{DLT,y} = y_m - y_i \quad (4.24)$$

$$\epsilon_{DLT} = \frac{1}{n} \sum_{i=1}^n \sqrt{\epsilon_{DLT,x}^2 + \epsilon_{DLT,y}^2} \quad (4.25)$$

Based on the measured calibration points and the ones computed by the reconstruction algorithm, the calibration error associated with DLT was estimated to be equal to 0.366%. In addition to this, an uncertainty in evaluating the location of the transition point can be attributed to the relatively low spacial resolution of the camera and can be equal to about $3 \pm 0.3\%mm$.

During a typical wind tunnel run, the surface temperature increase from the ambient conditions is in the range of $5K$ for the laminar boundary layer to a maximum of about $19K$ near the hot spots. The temperature increase observed are comparable to those obtained by [Tirtey et al. \(2011\)](#) who safely neglected any possible effects of this temperature rise owing to negligible effect of wall temperature in those condition. Following them, this effect is neglected in this study. In addition to boundary layer properties, the material properties are also subjected to changes with temperature. For the same temperature range considered above, the maximum change in the values of conductivity and specific heat capacity for a polycarbonate material (Makrolon[®]) was determined to be equal to 5% and 10% respectively ([Schrijer, 2010](#)).

[Cook and Felderman \(1966\)](#) is based on a 1D semi infinite model. Thus it neglects any lateral conduction that may possibly occur due to the temperature difference. However, when

estimating the local heat flux due to lateral conduction, based on the maximum temperature difference between two adjacent pixels and the pixel pitch, it was estimated that the conductive heat flux contribution is less than 3% of the local convective heat flux which is acceptable and hence can be neglected. The Cedip 630L IR camera, with an NETD of $0.025K$ also results in a small uncertainty in the temperature estimation. Thus the total uncertainty in the heat flux estimation was estimated to be within 6% using the method formulated by Moffat (1988). This value, coupled with the uncertainty in the free stream properties (see Section 4.1) and temperature measurements results in an overall uncertainty in the Stanton number estimation to be within 8%.

Chapter 5

Results and Discussions

In this chapter, the results of Quantitative Infra-red Thermographic investigation, pertinent to the laminar interactions are discussed. The undisturbed boundary layer is first assessed in Section 5.1 to ensure the presence of laminar boundary layer. This is followed by a description of the heat transfer topology and its association to the local flow features in Section 5.2. While Section 5.3 describes and compares the centreline Stanton number distribution, Section 5.4 takes advantage of the 2D heat transfer distribution around the cylinder and discusses the flow topology and wake evolution. Finally, in Section 5.5 a brief discussion of the upstream separation region is carried out.

5.1 Undisturbed Boundary Layer

Before entering into the discussing on the effect of the roughness element on the laminar boundary layer, the state of the boundary layer in the model surface has to be investigated. While no measurements were carried out specifically for the smooth flat plate case, it was observed that the boundary layer development far from the centre of the plate in the span-wise direction is mostly unaffected by the presence of the element. Hence one can safely study the development of Stanton number in that region as an assessment for the state of boundary layer in the undisturbed region. However to be sure, the off centre profile of the smallest element available is studied to minimise any potential effects.

Fig.5.1 shows the the variation of Stanton number along the stream wise direction on the flat plate for all the three Reynolds number case. The figure also shows the theoretical expected Stanton number distribution that was calculated using the reference temperature method (Eckert, 1956) (see Appendix A). It has to be noted that the reference temperature method provides an estimate of Stanton number non-dimensionalized by the adiabatic wall temperature (T_{aw}) while the measured profile is normalised by the modified Stanton number (C_h). Hence care has to be taken to properly account for this. On first sight, one can see that the distribution of Stanton number shows really good agreement with the theory except for a minor variation near the leading edge of the plate. The out of wake Stanton number also

tends to move away from the theory close to the end of the plate and this deviation intensifies with the reduction in the Reynolds number. A similar deviation was also observed by [Tirtety et al. \(2011\)](#) and [Avallone et al. \(2016b\)](#). However, the boundary layer is seen to remain under laminar condition, which is not surprising given that this wind tunnel model was specifically designed to have a laminar flow over it. As expected, the Stanton number is seen to decrease in the stream wise direction owing to the reduced heat transfer as the boundary layer develops along the length of the plate. Given that the overall trend of laminar profile over the model has been verified through the measurements for all the three Reynolds number case, the heat transfer on placing the roughness elements can be considered to be a result of interaction of the cylinder in a pure laminar boundary layer

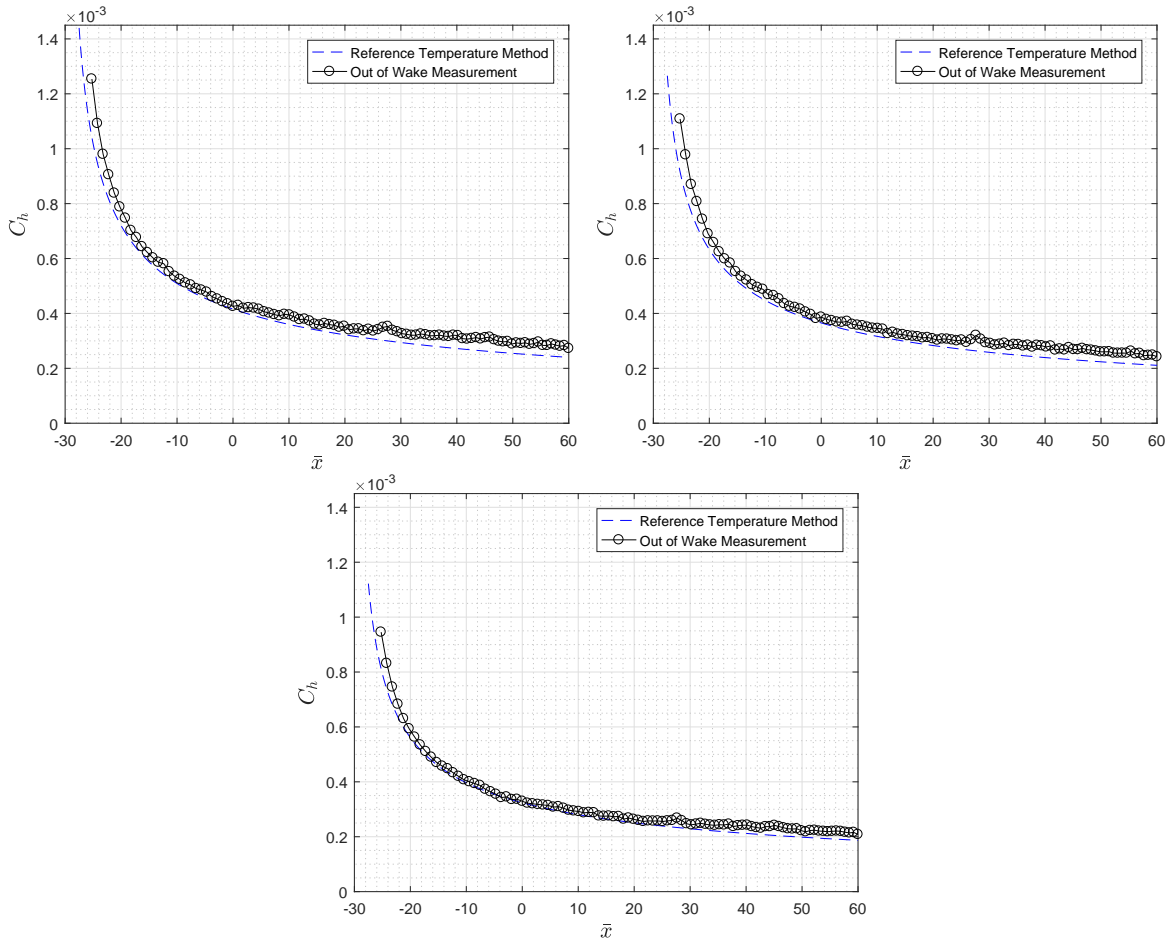


Figure 5.1: Undisturbed Boundary Layer corresponding to $Re = 8 \times 10^6 m^{-1}$ (Top left) $Re = 11 \times 10^6 m^{-1}$ (Top right) and $Re = 14 \times 10^6 m^{-1}$ (bottom)

5.2 Interpretation of Heat Transfer Topology

Before moving onto a detailed discussion of the heat transfer profiles for the various geometries, a good part of this section focuses on relating a typical heat transfer distribution to the flow topology near the surface of the flat plate. Various researchers have observed previously

that a roughness element in a laminar flow acts as a vortex generator generating a system of stream wise vortices downstream of the element (Danehy et al., 2009) (Tirtey et al., 2011). These stream wise vortices that are observed downstream are hypothesised to be the result of the horseshoe vortex that forms upstream of the roughness element and wraps around the element. The schematics depicting the symmetry plane and off symmetry plane vortices in the wake region is shown in Fig.5.2.

The stream wise vortices that are close to the symmetry plane at $\bar{y} = 0$ are the Symmetry Plane (SP) vortices while those that are generated far from the symmetry plane are Off Symmetry Plane vortices (OSP, OSP' or depending on the scenario). The rotation of these vortices are such that there exists a central up wash close to the symmetry plane. This drains the low momentum fluid close to the wall thus reducing the skin friction and hence the heat transfer in that region leading to the formation of low speed and low heat transfer streaks. However, the region between the SP and the OSP vortices experiences a central down wash forcing a jet of high momentum fluid towards the wall forming high speed and high heat transfer streaks

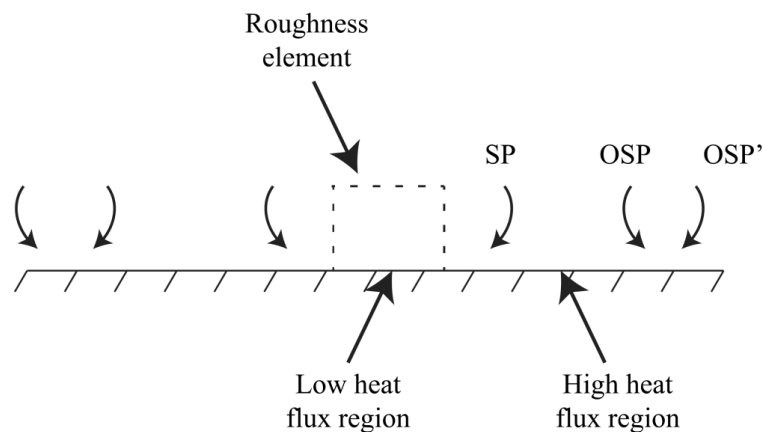


Figure 5.2: Nomenclature of vortices adopted from Iyer and Mahesh (2013). SP - Symmetry plate; OSP - off - symmetry plane

A typical Stanton number distribution is shown in Fig.5.3. Based on the discussion earlier, the major structures from the heat transfer distribution can be identified. Region 1 present upstream of the cylinder correspond to the high heat transfer region due to the formation of multiple system of vortices, the number of which is dependent on the geometry and flow conditions. The down wash from the vortices produces a peak in heat transfer and wraps around the cylinder which can also be inferred from the high heat transfer region wrapping around the front face of the cylinder. The upstream vortices as it moves downstream form into SP and OSP vortices causing a series of low and high heat transfer streaks along the span (regions 2 to 3). A local minimum in the heat transfer value along the centreline can be attributed to the central up wash due to the SP vortices. As one moves downstream from the centre, the high heat transfer streak due to the SP vortices, tends to move closer to each other due to the low pressure region that is formed just downstream of the roughness element (Iyer and Mahesh, 2013). Further downstream, the high heat transfer streak begins to lose its intensity due to decreased strength of the stream wise vortices and the lift up

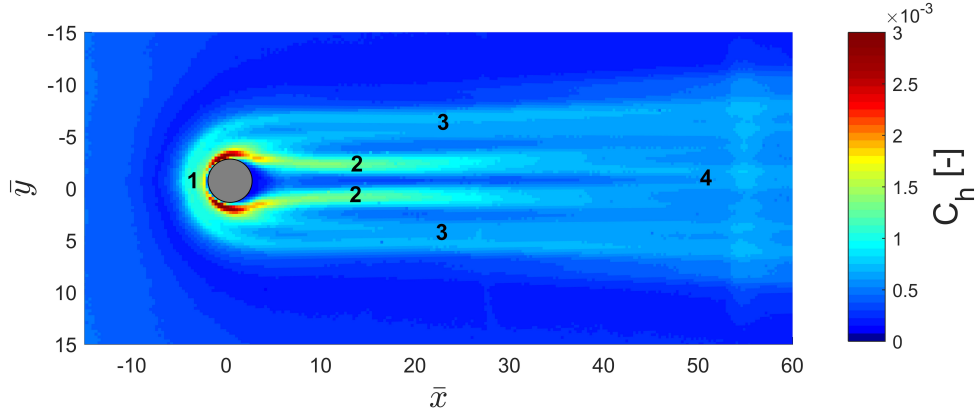


Figure 5.3: 2D Stanton number distribution for R14 D8 case showing the high heat flux due to upstream vortices (1), High heat flux due to central down wash (2), OSP vortex interactions (3), near uniform high heat flux region in the far wake (4). Flow is from left to right

mechanism of the SP vortex pair (Avallone et al., 2014). A span wise near uniform region of heat transfer can be observed close to the end of the plate (region 4), due to the intense mixing and breaking down of these vortices. That is also the region where the wall heat flux begin to diverge which many indicate the formation of turbulent wedge. A detailed sectional plots of all these features will be discussed in the following sections.

5.3 Centreline Stanton number Distribution

In the previous section, it was observed that, in a typical heat transfer distribution around a cylinder, the wake centreline is characterised by a low heat transfer region. However, to gain an idea about the general wake behaviour, the stream wise variation of the centreline heat transfer distribution is a good starting point. Fig.5.4 shows the Stanton number distribution along the centreline of all the four geometries. The theoretical expected laminar and turbulent Stanton numbers calculated using the reference temperature methods are also plotted for reference. Note that the horizontal coordinate x^* is the stream wise distance, scaled with the height of the cylinder, with origin at the trailing edge of the element (see Section 4.2).

The centreline Stanton number profiles gives a first indication of how strongly a roughness can affect an otherwise smooth laminar development. On comparing the Stanton number distribution for a given Reynolds number, it can be found that the profiles are very much dependent on the diameter of the element. In the near wake region, closer to the roughness geometry, the heat transfer is seen to be higher for the roughness of smaller diameter. For the same conditions, roughness of larger diameter will possess a stronger blockage to the incoming flow and hence will have a larger low pressure region in the near wake downstream. This dependency of Stanton number on the frontal area of the element evident from the Stanton number distribution in the near wake.

A local peak is observed immediately downstream of the element, for all diameters and Reynolds numbers, below $x^* = 10$. This may correspond to the reattachment of the flow downstream (Avallone et al., 2016a). The reattachment point location seems very much

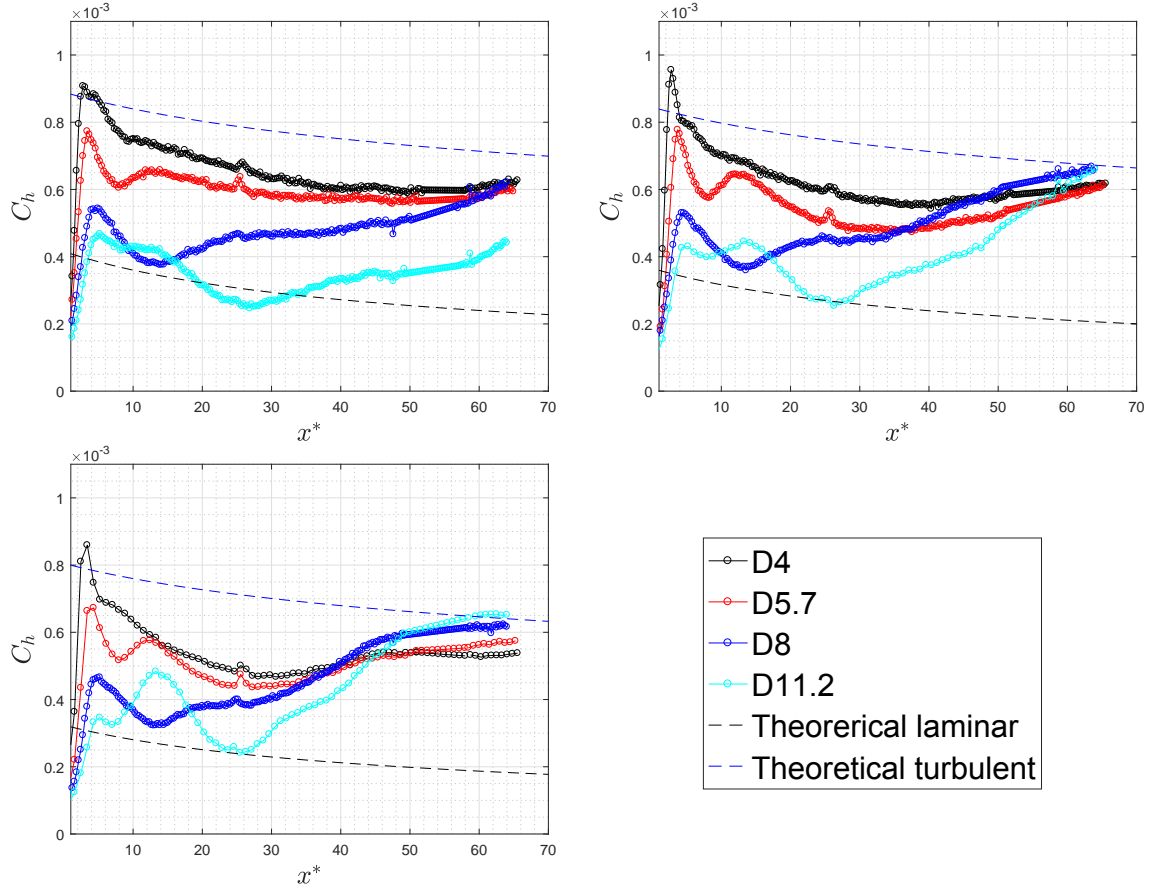


Figure 5.4: Centreline Stanton number profile corresponding to $Re = 8 \times 10^6 m^{-1}$ (Top left) $Re = 11 \times 10^6 m^{-1}$ (Top right) and $Re = 14 \times 10^6 m^{-1}$ (bottom left) for all the roughness geometries

invariant with the flow unit Reynolds number. It may also appear that with increase in diameter, the reattachment point moves downstream. Though this is true with respect to the centre of the roughness element, when measure from the trailing edge of the roughness element, as in this case, the reattachment point seems to remain constant with a value of $x^*_{reattachment} = 3.6 \pm 0.1$ making it quite independent of the diameter of the roughness element and scaling with height. However, measurements at other roughness element heights are necessary to have clarity.

In some cases, downstream of the reattachment peak, the Stanton number decreases and starts to increase again. The may be due to the acceleration of the flow due an expansion downstream increasing the skin friction and hence the Stanton number (Marxen et al., 2010) (Avalone et al., 2016a). After this expansion phase, the boundary later starts to develop again and that can be seen as a decrease in the local Stanton number profile. The heat flux then can be seen to rise again, that may indicate any transitional features (Avalone et al., 2016b) and eventual growth towards the turbulent heat flux region. The downstream wake measurements unfortunately were not long enough to capture the gradual settling down of the fully turbulent wake.

While the above few paragraph attempts to provide an overall picture of the Stanton number profile, it has to be noted that the profile is very much dependent on the flow Reynolds number and the geometry of the roughness element. The D4 and the D8 elements does not exhibit the expansion phase discussed above and are directly seen to experience a change of slope. For $Re = 8 \times 10^6 m^{-1}$, the variation in Stanton number profile between the D4 and D5.7 is prominent only in the near wake region and tends to align and grow when moving downstream.

Avallone et al. (2016b), in their study on the Stanton number variation along the centreline of roughness elements of various shapes reported observation of change of slope and rapid increase of Stanton number in a region where high turbulence intensity was observed in the Tomo-PIV data. Based on that, the authors associated that region as the location of transition. Looking at the Re14 case a similar trend can be observed for D11.2 case where the Stanton number reaches a minimum and starts to rapidly increase. However, some cases shows a gradual drop in slope followed by a more gradual increase in its value. While the trend remains the same, without any velocity information, it cannot be conclusively said these regions of change of slope correspond to the transition point.

While it was not possible to conclusively estimate the transition point from the centreline distribution, it is possible to study the effect of flow Reynolds number. It can be seen that, as the Reynolds number decreases, the flow take more length downstream to attain a fully turbulent state. For Re8 measurement, all the elements failed to attain a the turbulent Stanton number profile within the measurement domain, but are seen to tending towards that point. This effect is quite accelerated as the flow Reynolds number is increased. This is not surprising since as the Reynolds number is increased, the boundary layer thickness at the point of the roughness element is decreased. Hence for the same height, the roughness element is more 'effective' at tripping the boundary layer at higher Reynolds number than at lower Reynolds number. This can also be inferred from how the slope of the Stanton number profiles far downstream of the roughness elements (beyond $\bar{x} = 30$) tends to increase as the flow Reynolds number increase indicating possibly high turbulence and stronger mixing as the Reynolds number increases.

5.4 2D Heat Transfer Distribution

The main advantage of IR thermography is its ability to measure the temperature map and hence the heat transfer map of the entire 2D domain of interest. Hence in this section, a 2D study of the heat flux pattern behind roughness elements of various geometries will be carried out. The heat transfer maps for the D4 and D5.7 case are shown in Fig.5.5, while the heat flux maps of D8 and D11.2 are shown in Fig.5.6. In both these figures, cases (a,d), (b,e) and (c,f) correspond to a unit Re of $8 \times 10^6 m^{-1}$, $11 \times 10^6 m^{-1}$, $14 \times 10^6 m^{-1}$ respectively. The location of the roughness elements are coloured for reference.

As described earlier, a high heat flux is observed immediate upstream of the protuberance, for all the Reynolds number case. The height of the protuberance selected for this study is equal to or greater than the size of the local boundary layer height. These conditions are termed as supercritical in literature (*Estruch-Samper et al., 2010*), featuring a separated

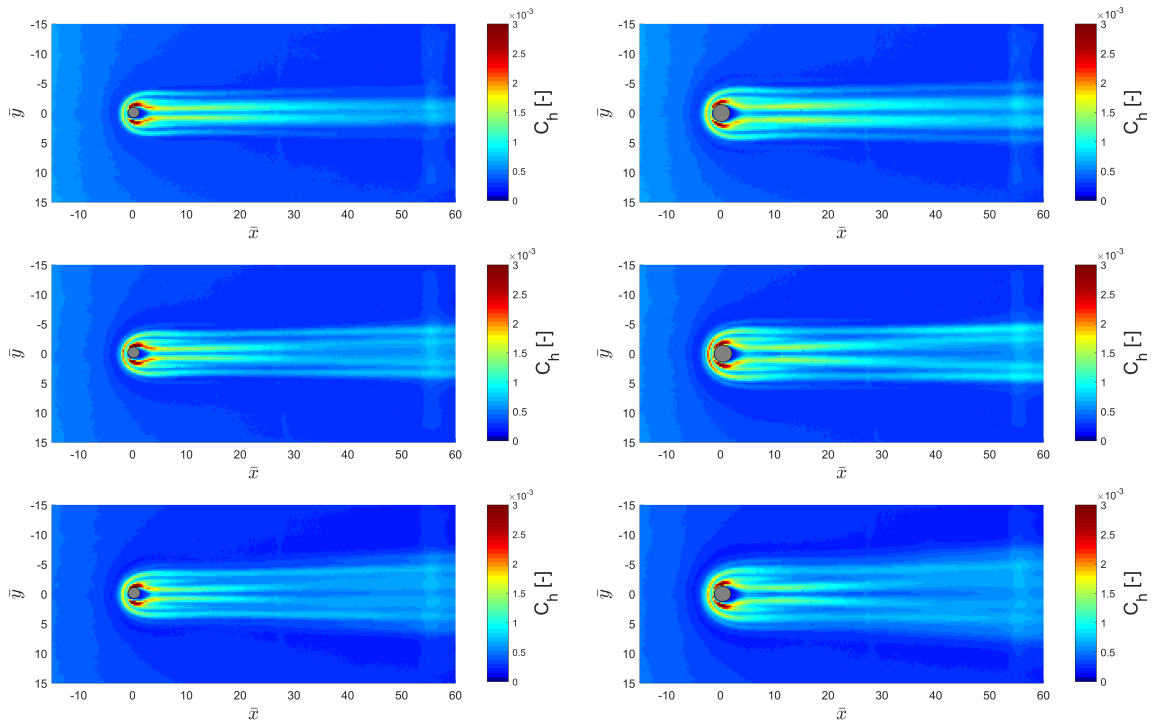


Figure 5.5: 2D Stanton Number distribution corresponding to D4 (left) and D5.7 (right) cases for all the three Reynolds number. Cases (a,d), (b,e) and (c,f) correspond to a unit Re of $8 \times 10^6 m^{-1}$, $11 \times 10^6 m^{-1}$, $14 \times 10^6 m^{-1}$ respectively

boundary layer and a large heat flux. The heat transfer peak can be associated with the vortex system upstream, where the down wash generated by the vortices correspond to the high heat transfer value observed. Further detailed investigation on the upstream separation region can be found in Section 5.5

Moving downstream, one obvious observation is that the width of the wake tends to be wider for roughness elements of larger diameter and this is also found to be consistent at all the three flow unit Reynolds number considered for this study. The near wake of the roughness elements are seen to possess a series of high and low speed regions, shown by a streaks of high and low heat flux regions. These streaks, as discussed earlier correspond to the down wash and up wash generated by the stream wise vortices that are generated downstream of the roughness element. It has already been observed that the roughness act as vortex generators and hence it would be interesting to know how the strength of the vortices correlate to the roughness geometry.

Fig.5.7 shows the spanwise variation of heat flux for the four roughness elements at a distance of $x^* = 10$ from the trailing end of the element. Note that, in this plot, the heat flux is normalised by means of q^* , which is the ratio of the test heat flux to the undisturbed laminar heat flux. The values away from the centre of the element is close to 1, denoting the undisturbed region. It was observed earlier that the wake width increased with the diameter of the element. Hence it can be logical to expect that it would scale with the diameter of the element. However, as seen in Fig.5.7, only the SP peak locations scale with the diameter of

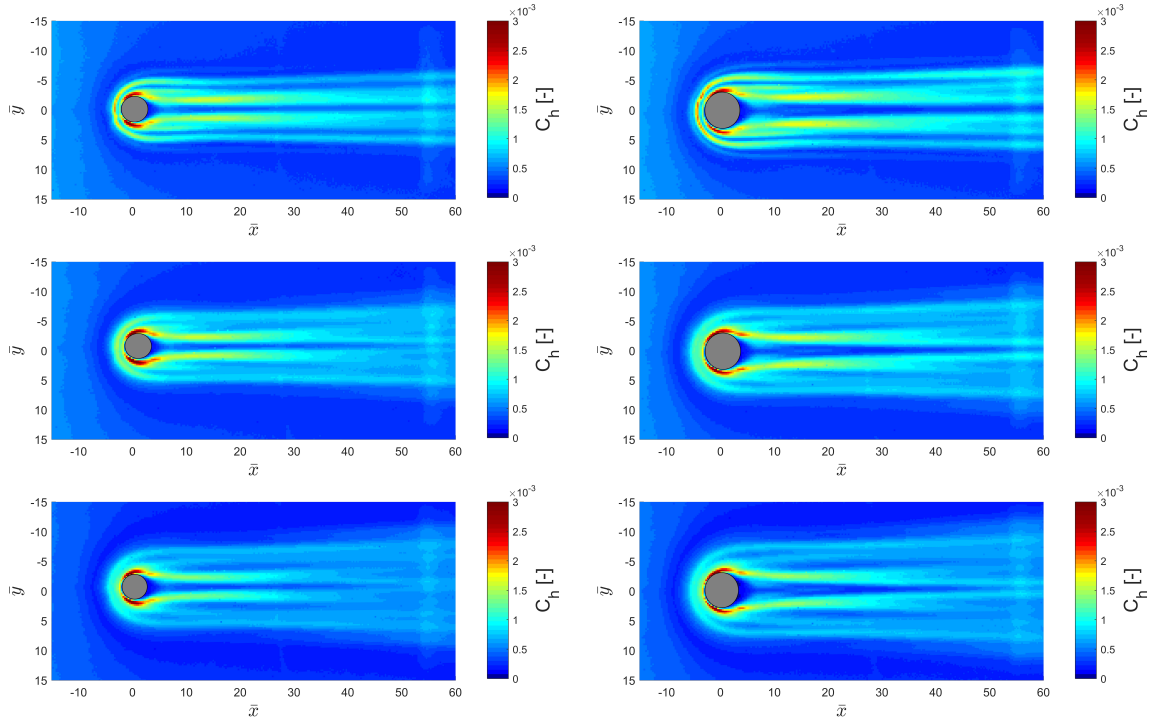


Figure 5.6: 2D Stanton Number distribution corresponding to D8 (left) and D11.2 (right) cases for all the three Reynolds number. ases (a,d), (b,e) and (c,f) correspond to a unit Re of $8 \times 10^6 m^{-1}$, $11 \times 10^6 m^{-1}$, $14 \times 10^6 m^{-1}$ respectively

the element. In order to study the strength of the stream wise vortex, the strength of the heat flux peak is observed. Notice that for a constant unit Reynolds number, the peak heat flux increases with increase in diameter of the element, though very subtle. These peaks are caused due to the down wash generated by the SP vortices. The observed heat flux behaviour provides possible evidence that the strength of these SP vortices increases with increase in diameter. One has to be careful here, since the peaks observed may not be true peaks owing to the low resolution of the camera. However, this was observed for measurements taken at the other two Reynolds number also, thus making it more plausible.

While the strength of these vortices seems to increase with diameter, it would be interesting to check their effect with changing Reynolds number. In Fig.5.8 the spanwise variation of the normalised heat flux is replotted for D4 and D8 cylinders at the lowest and the highest Reynolds number at which measurements were taken. Two observation can be make from the figures. It can be seen that increasing the unit Reynolds number increases the wake width. While this was earlier observed in the 2D maps of Stanton number, these figures portray the difference more clearly. Also, similar to the earlier case, only the SP peak locations scale with the diameter of the element, irrespective of the Reynolds number. Increasing the flow Reynolds number also increases the heat flux peak because of the vortices by 9.10% and 8.5% respectively for D4 and D8 cylinders. Interestingly, the positions of the heat flux peaks seems to be invariant with the flow Reynolds number. This means the rate at which the SP vortices tending to move closer to the symmetry plane is not affected by changing the Reynolds number, and may depend mainly on the span or diameter of the roughness element.

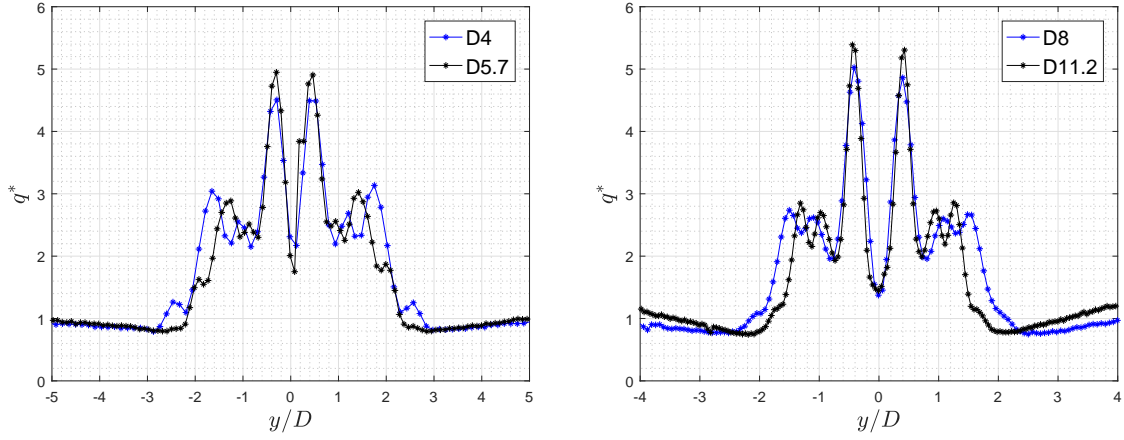


Figure 5.7: Spanwise variation of heat flux at $x^* = 10$ for D4, D5.7 (left) and D8, D11.2 (right) cases at unit $Re = 14 \times 10^6 m^{-1}$

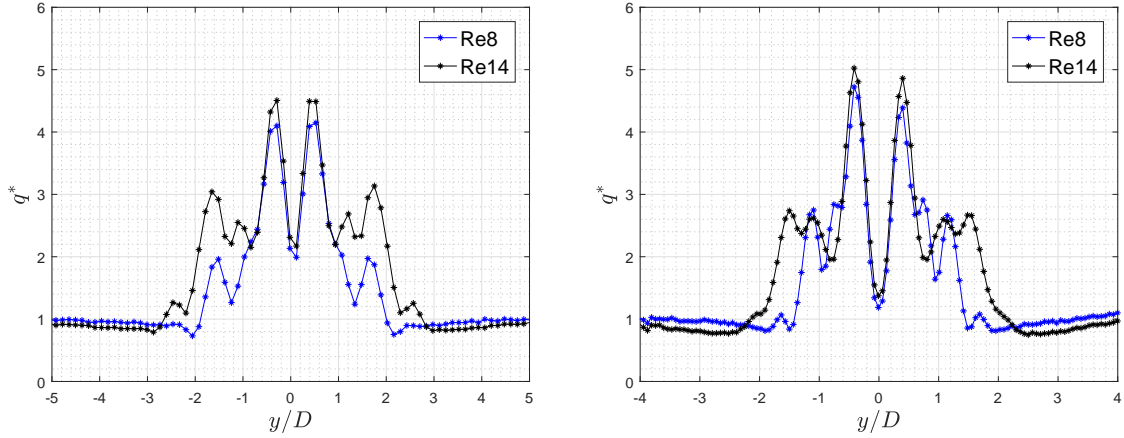


Figure 5.8: Span wise variation of heat flux at $x^* = 10$ for D4 (left) and D8 (right) cases at two unit Reynolds number

The high heat transfer streaks begins to reduce in intensity when moving downstream. Tomographic PIV measurements behind a cylindrical roughness element taken in the same facility by [Avalone et al. \(2014\)](#) show that the SP vortices tends to move up higher in to the boundary layer as it travels downstream. This could possibly explain the reduction in the heat flux intensity of the streaks near the centre plane. Far downstream, the heat flux map shows that the wake tends to be more uniform than the near wake region. A better understanding of the level of disturbance that a roughness element causes can be gained by plotting the streamwise variation of heat flux perturbation amplitude (A), which for a given stream wise location, can be defined as half of the difference between the Stanton number maximum and Stanton number minimum along the span ([Avalone et al., 2016b](#)):

$$A(x) = \frac{1}{2}(Ch_{max}(x, y) - Ch_{min}(x, y)) \quad (5.1)$$

This parameter will provide an idea about the level of flow perturbation exhibited by a given roughness element. For a theoretical laminar wake, this will be zero and for a fully turbulent

wake, this value will be proportional to the different between the corresponding turbulent and laminar Stanton numbers. Fig.5.9 shows the variation of this amplitude along the stream wise direction. The amplitude tends to fall when moving downstream which corresponds with the central high heat flux streak losing its intensity as it travels downstream. As observed in the sectional plot, the amplitude is larger for elements with larger diameters. Additionally, observing Re14 case, it can be seen that the elements with the higher diameter tends to take longer to settle down at the constant value. This could mean that indicated that the strength of the high heat transfer streaks stay longer in the wake for elements with larger diameter, which is also observed from the 2D heat transfer distribution shown earlier. A local overheating was observed for the D5.7 case at $Re = 11 \times 10^6 m^{-1}$, which is similar to what was obtained by [Avallone et al. \(2016b\)](#).

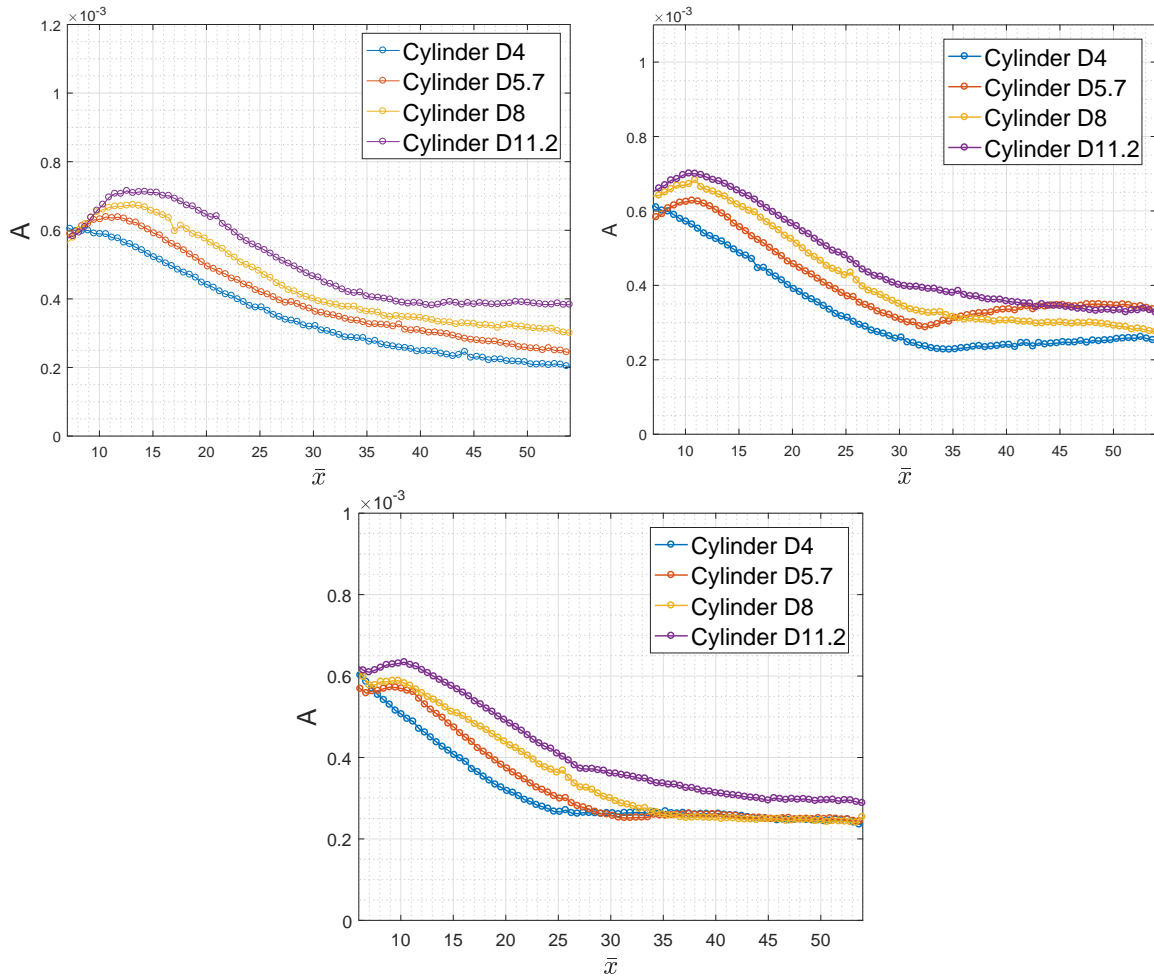


Figure 5.9: Heat flux perturbation amplitude for all elements corresponding to $Re = 8 \times 10^6 m^{-1}$ (Top left) $Re = 11 \times 10^6 m^{-1}$ (Top right) and $Re = 14 \times 10^6 m^{-1}$ (bottom)

In the previous section, it was attempted to try to indicate the onset of transition from the centreline Stanton number plots. However, it was not possible to conclusively point out the exact location of transition. Now that a 2D map is available, another widely used approach to locate the transition point can be followed. As the transition begins to occur, a spanwise spreading of the wake occurs forming a 'turbulent wedge'. This was widely studied in the low

speed experiments (Gad-El-Hak et al., 1981) and have also been reported to occur in high speed experiments (Ye et al., 2016) (Avallone et al., 2016b) (Tirtey et al., 2011).

Looking at Fig.5.5, the D4 and D5.7 cylinder seems to maintain nearly uniform width throughout the measurement domain for low and medium Reynolds number (Re8 and Re11). The high heat flux also maintains an appreciable level of intensity even toward the end of the measurement domain. However, as the centreline Stanton number profiles for these geometries did not tend to drop towards the laminar case (see Fig.5.4), it could be possible that transition and onset of turbulent wedge may happen far downstream from the measurement domain. However, for the highest Reynolds number case, a distinct turbulent wedge was seen to appear from $\bar{x} = 25$ and $\bar{x} = 22$ respectively for D4 and D5.7 cylinders. This portrays that the transition point moves upstream with the increase in flow Reynolds number. A similar observation was also made by Ye et al. (2016) where the transition moved upstream with roughness height based Reynolds number (Re_H). Since the height of all the roughness element considered in this investigation is the same, the trends can be compared and is consistent.

Moving on to the larger elements, the D8 and D11.2 cylinders shows evidences of slightly less intense yet distinct presence of streaks in the far downstream region at R8 case. The absence of a near uniform region may indicate that the flow has not yet reached a uniform turbulent state. As the Reynolds number increases, the span wise uniformity also tends to increase. The wake can be seen to diverge starting at $\bar{x} = 27$ for D8 cylinder and $\bar{x} = 30$ for D11.2. As observed in the amplitude plots, for a given Reynolds number, the strength of the stream wise vortices and hence the streaks is observed longer in the wake for elements of larger span / diameters.

Fischer (1972) collected data from various sources and studied the effect of the spreading angle with Mach number and observed that the lateral spreading angle was found to be exponentially reducing with Mach number. A spreading angle of $\phi \leq 3$ resulted from his investigations for a flow Mach number corresponding to 7. To have confirmation on whether the spreading observed here correspond to the onset of turbulent wedge, the values obtained can be compared with that data. The wake width at a given stream wise location was calculated as the span wise extent through which the surface heat flux was observed to be perturbed with respect to the off centre laminar heat flux. For the cases where a turbulent wedge was observed, the spreading angle varied between 2.06° and 3.61° which is consistent with the data of Fischer (1972). Note that, given the uncertainty owing to the low resolution of the camera and to the very low length of turbulent wedge available in the wake within the measurement domain, it was not possible to determine the wake width with a very high accuracy. Thus the estimates of wake angle was only made to assess the validity of turbulent wedge and comparative studies on the wake width evolution with geometry and Reynolds number was not made.

5.5 Upstream Separation Region

All the roughness elements tested had a height of $h = 2mm$ and the height ratio with respect to the local boundary layer thickness equals 1, 1.17, 1.33 corresponding to the R8, R11 and R14 cases respectively. Based on the work of Hung and Clauss (1980) and Hung and Patel

(1984), the roughness in this study can be classified as short protuberances (since $H < D$). It is true that D4 case does not strictly satisfy this criterion. However, there is no clear physical reasoning as to why this classification was made. Hence it would be interesting to see whether this geometry deviates from the descriptions and expectations of a short protuberance.

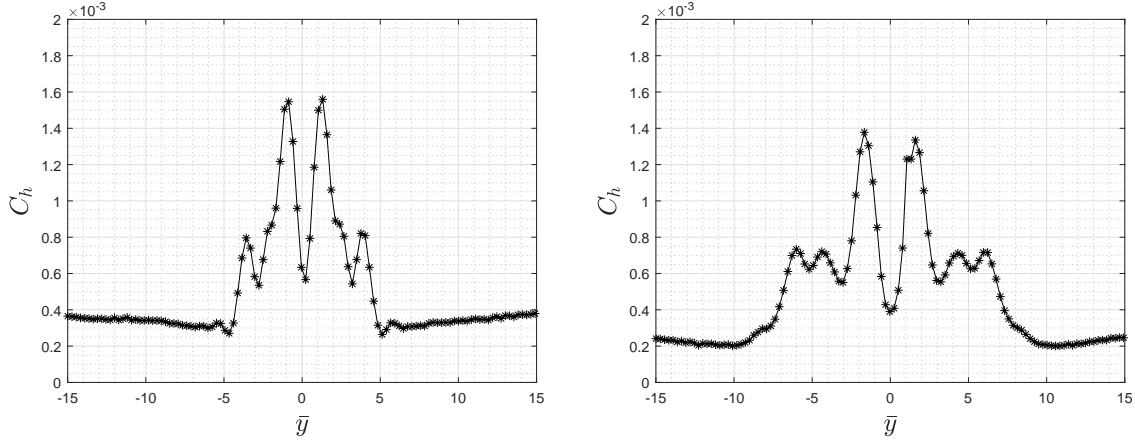


Figure 5.10: A 4 vortex system by D5.7 Cylinder at $Re = 8 \times 10^6 m^{-1}$ (left) and a 6 vortex system by D8 Cylinder at $Re = 14 \times 10^6 m^{-1}$ (right). Both span wise variations are plotted 3 diameters downstream of the cylinders

Because of their large height relative to the local boundary layer thickness, a small portion of the cylinder near the tip is exposed to the high momentum air. The large pressure gradient which the flow experience just upstream of the roughness element will lead to flow separation (Lighthill, 1953). The separated boundary layers will result in the formation of span wise vortices just upstream of the roughness elements resulting in flow reversal and recirculation. The presence of these system of vortices were observed earlier by researchers both in the subsonic (Baker, 1979) and supersonic / high speed regimes (Iyer and Mahesh, 2013) (Subbareddy et al., 2014). Baker (1979) reported the dependency of the number of unsteady system of vortices to the Reynolds number based on diameter and the ratio of diameter to the displacement thickness. Since the upstream span wise vortices wrap around the cylinder, studying the heat flux pattern in the near wake should provide evidence of the number of vortices that were formed upstream. Fig.5.10 shows an example of the 4 vortex and 6 vortex systems observed behind two of the roughness elements at lower and higher unit Reynolds number, which is consistent with the expectation from literature.

These *supercritical* elements, owing to the recirculation region upstream leads to a heat flux peak (Estruch-Samper et al., 2010). Fig.5.11 shows the typical Stanton number variation upstream of a supercritical roughness element along the centreline at $\bar{y} = 0$. Far upstream, the boundary layer development seemed unaffected by the presence of the element. This is evident from the Stanton number distribution which decreases as the boundary layer grows over the plate. This is the case till $\bar{x} = -10.72$, when the Stanton number curve begins to decrease and deviate from the theory. This marks the point of separation. After a local minimum at $\bar{x} = -7.53$, there is a steep increase in the Stanton number. A local maximum occurs at $\bar{x} = -3.74$ and an absolute maximum at $\bar{x} = -2.49$. At its maximum, the Stanton number recorded a value of 1.74×10^{-3} . which is much higher than the corresponding local

turbulent Stanton number.

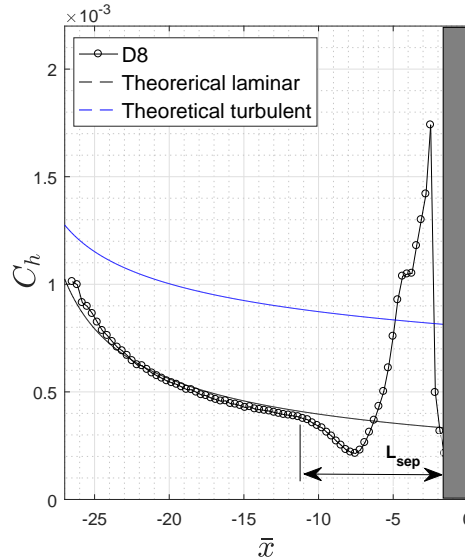


Figure 5.11: Peak heating and upstream separation region of D8 cylinder at $Re = 14 \times 10^6 m^{-1}$

Based on the work of [Avalone et al. \(2016a\)](#), it can be inferred that the presence of the local and the absolute peaks in the Stanton numbers correspond to the local down wash due to the span wise vortices upstream of the roughness element. A similar heat flux profile was observed for all the roughness elements - a normal boundary layer development, followed by a heat flux drop due to separation and then local and absolute peaks due to the span wise vortices.

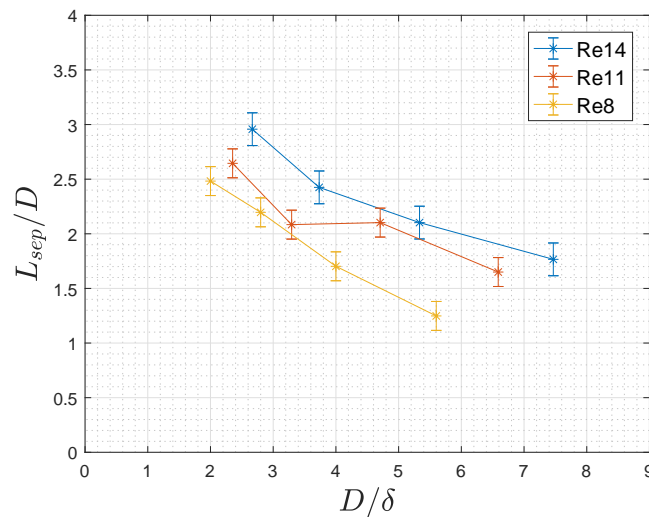


Figure 5.12: Variation of upstream separation length

[Kumar et al. \(2014\)](#) studied the length of upstream separation region for 3D roughness elements of various heights, based on which a rough correlation between the height of the roughness element to the upstream separation length (L_{sep}) was found. However, there was

no information on how the length of the upstream separation region could vary with the diameter of the element. In Fig.5.11, the length of the upstream separation region is defined. It is distance between the leading point of the protuberance to the point upstream where the Stanton number distribution starts to deviate from the laminar profile. Fig.5.12 shows the variation of the upstream separation length with the diameter of the elements for all the Reynolds number. The error in the estimates may originate from the low resolution of the camera.

It can be seen that as the diameter of the element increases, the length of the upstream separation, scaled with the diameter of the element decreases for all the three Reynolds numbers. However, there seems to be no perfect scaling of the separation length with the diameter of the roughness element. For a short protuberance, the following correlation for the upstream separation length can be given.

$$\frac{L_{sep}}{D} = 3.5 \left(\frac{H}{\delta} \right)^{0.7} \left(\frac{D}{\delta} \right)^{-0.435} \quad (5.2)$$

This relation is adopted and modified from the work of [Hung and Clauss \(1980\)](#). While their exact empirical co-relation did not match the current data set, this modified version provides a good fit. Since the correlation is not based on any physical mechanism, the reason behind this discrepancy is not surprising.

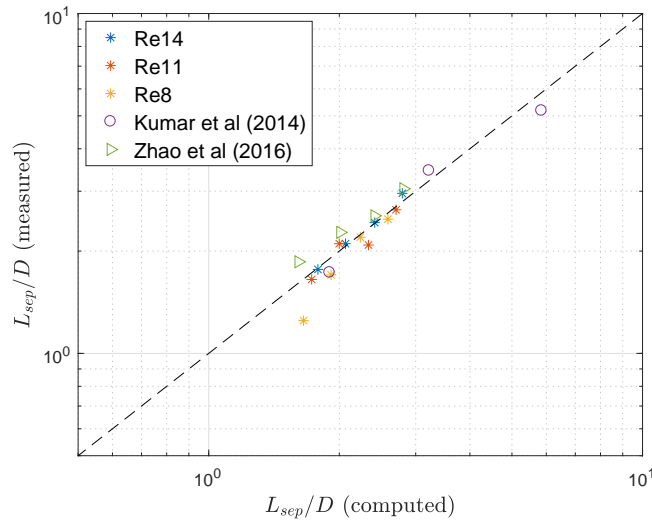


Figure 5.13: Empirical correlation predicting the upstream separation distance

Fig.5.13 shows the measured upstream separation lengths and its comparison with the empirical correlation shown in Eqn.5.2. The trends seems to agree the expectation. However, in order to have further confidence in the expression, the upstream separation length obtained from recent literature was also compared with this expression, which also seems to agree quite well. We already learned from literature that the upstream separation length could influence the magnitude of the heat flux peak in the recirculation region upstream. This correlation highlights the importance of the diameter of the protuberance in estimating the length of separation upstream, contrast to the study carried out in recent literatures, where the effect of the height was only considered. When carefully observed, some points from the current

study, corresponding to Re8 case tends to deviate from the curve. This could possible because of the local boundary layer length being exactly equal to the height of the protuberance, while all the other conditions correspond to the protuberance height greater than the heigh of the boundary layer. While this is quite satisfactory, in order to have clarity, experiments have to be conducted corresponding to L_{sep}/D near the lower and upper end of the curve to have better statistical convergence.

Part II

Effect of a Surface Protuberance in an Incoming Turbulent Boundary Layer

Chapter 6

Experimental Design

In the previous chapter, results of interaction of a cylinder with an incoming laminar boundary layer was discussed. While the effect of protuberance in a laminar boundary layer is interesting to investigate, majority of the boundary layers in present day high speed aircraft are turbulent in nature when they meet a surface protuberance. Thus, it is essential to gain an idea of such interactions as well. Hence experiments were conducted in the ST-15 facility of the high speed laboratory to investigate the effects of a cylindrical surface protuberance on an incoming turbulent boundary layer using High Speed Schlieren and Quantitative Infra-red Thermography. In this chapter, the flow facility and the data reduction methodology will be discussed and in Chapter 7, the results of the interaction will be analysed in detail.

6.1 ST-15 Supersonic Windtunnel

The ST-15 is a blow down type supersonic tunnel located in the High Speed laboratory of the Faculty of Aerospace Engineering, Delft University of Technology (see Fig. 6.1). By changing the nozzle block, each with their specific geometry, tests can be performed in a range of Mach numbers from $M = 1.5 - 3$, in steps of 0.5. All the experiments pertinent to this research were carried out at Mach 2 condition.

For a Mach 2.0 nozzle block configuration, the test section is present directly downstream of the diverging section of the nozzle. Optical access measuring a diameter 25.5cm is made available on either side of the test section to carry out PIV or Schlieren measurements. It is also possible to replace the optical windows with other suitable window types of same diameter to suit the measurements. Dry air is stored in an external reservoir of 300m^3 at 40 bars. The tunnel is operated by turning a valve, which directs the high pressure dry air from the reservoir to fill the settling chamber. In the settling chamber, wire meshes are made available to straighten the flow and reduce flow turbulence. The conditions inside the settling chamber are considered to be the stagnation conditions and hence a thermocouple is attached to the inside of the settling chamber to monitor the temperature. Any temperature measurements taken will thus correspond to the stagnation temperature (T_0). When the

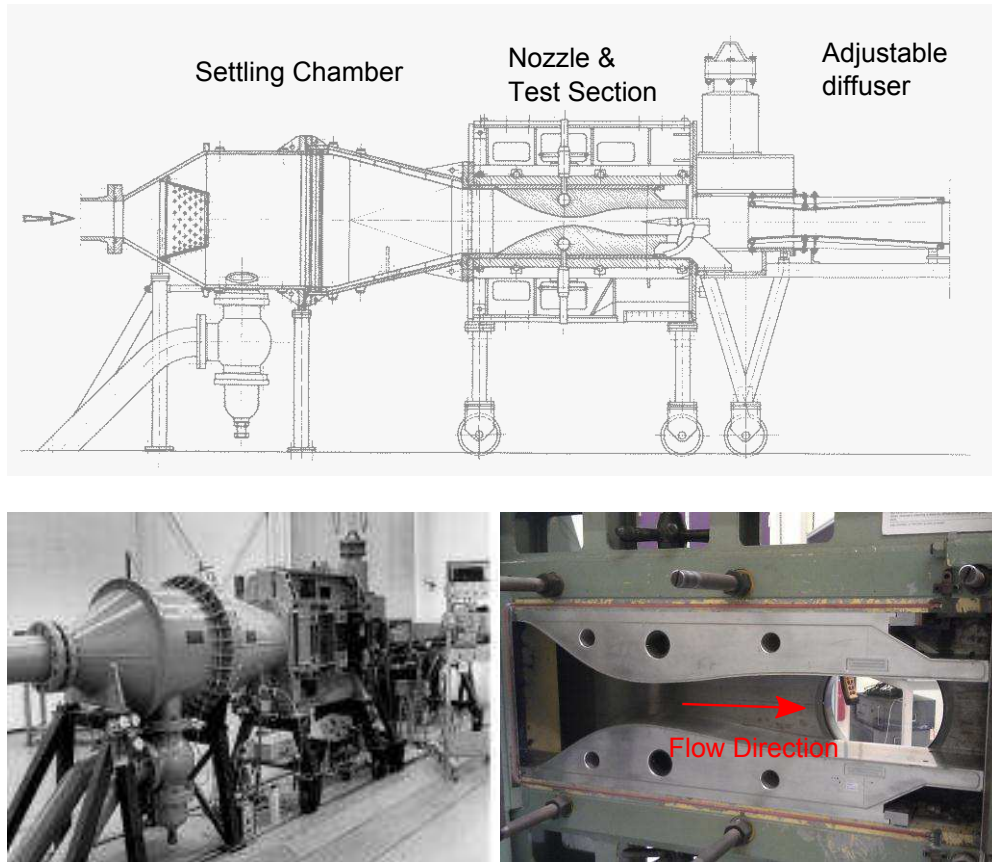


Figure 6.1: ST-15 Supersonic Wind tunnel - Schematic (top) and a view (bottom left). The picture on the bottom right shows the Mach 2.0 nozzle and the test section (redrawn from Sun (2014))

tank is completely charged, the ST-15 can run continuously at Mach 2.0 for approximately 18 minutes.

The boundary layer in the wall is turbulent in nature which originate around $1m$ upstream of the test section. Detailed flow assessment has been carried out by various researchers ((Giepmans et al., 2014), (Sun et al., 2012), (Tambe et al., 2017)), measuring the boundary layer profile using Particle Image Velocimetry (PIV). The free stream and boundary layer properties thus obtained can be found in the Table 6.1.

Table 6.1: Free stream and Boundary layer properties from the measurements of Giepmans et al. (2014)

Parameter	Quantity	Parameter	Quantity
M_∞	2.0	δ [mm]	5.2
U_∞ [m/s]	524	δ^* [mm]	0.63
P_0 [N/m ²]	3.2×10^5	θ [mm]	0.52
T_0 [K]	290	Re [1/m]	42.2×10^6

6.2 Roughness Geometries

Measurements were acquired, taking into advantage the turbulent boundary layer on the walls of the ST-15 test facility. The turbulent boundary layer in ST-15 test section wall is relatively thicker ($\delta_{99} = 5.2\text{mm}$) and hence a new set of roughness elements are manufactured with dimensions of the same order. While the ratio of roughness element height with respect to the local boundary layer thickness was varied by changing the flow Reynolds number in HTFD, the limitation of a single flow unit Reynolds number fixes the boundary layer thickness in the test section of ST-15. Hence the ratio is controlled by varying the height of the cylindrical roughness element in this investigation. Three different heights, each at three diameters were manufactured corresponding to dimensions shown in Fig.6.2.

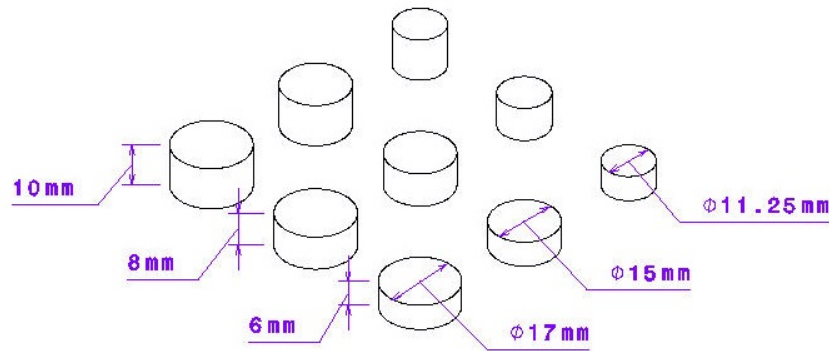


Figure 6.2: Roughness elements used in the Investigation of Turbulent interactions

For all the measurements taken, the roughness elements are attached to the wall using a high temperature resistance double sided adhesive tape, which introduces additional thickness of approximately 0.15mm . Similar to the laminar case, the roughness elements are also named based on their geometry. For instance, element H6D15 refers to the cylinder of height $H = 6\text{mm}$ and diameter $D = 15\text{mm}$. The complete protuberance geometries and the corresponding flow characteristics can be found in Table 6.2.

Table 6.2: Roughness element and Test characteristics

Parameter	H6			H8			H10		
	D1125	D15	D17	D1125	D15	D17	D1125	D15	D17
Diameter [mm]	11.25	15	17	11.25	15	17	11.25	15	17
Height [mm]	6 ± 0.15			8 ± 0.15			10 ± 0.15		
Re_θ	21944								
Re_H	253200 ± 6330			337600 ± 6330			422000 ± 6330		
H/δ	1.15 ± 0.025			1.54 ± 0.019			1.92 ± 0.015		

For the Schlieren campaign, the different geometries that needs to be tested were glued onto the bottom wall of the test section and the optical access on both the sides were utilised, while for the Oil Flow visualisation, the elements were glued onto the side wall and the opposite optical access was made use of to make any observation and record images. However this cannot be extended to Infra-red Thermography and hence a new test set-up designed by Voogt (2017) was used. It involves manufacturing a new wind tunnel door onto which a heated printed circuit board can be installed. The protuberances were glued on to this plate and measurements were taken through the optical access provided by a Germanium window on the other side of the test section. In the next section, a brief overview of the QIRT setup will be discussed.

6.3 QIRT Test Setup

The QIRT setup used in this experiment utilises a *Heated-thin-foil* sensor where ohmic heating is applied to a printed circuit board (PCB), providing precise knowledge of the heat flux distribution. By performing a complete energy balance at the steady state condition and by measuring the surface temperature of the sensor, the convective heat transfer coefficient can be computed (Astarita and Carlomagno, 2013). The principle elements of the active IRT setup used in the ST-15 facility are:

- A test plate consisting of a Printed Circuit board (PCB) and a Makrolon[®] insulation slab
- A cavity door onto which the test plate is mounted.
- CEDIP Titanium 530L IR Camera
- A thermocouple acquisition system to monitor the temperature
- A power supply to heat the test plate
- A Germanium window

A printed circuit board is one of the widely used heating elements in the heated thin foil approach to achieve the required specially uniform heating. The PCB used in the investigation consists of regularly arranged tracks of copper over a 1mm thick FR-4 base material, covering an area of 150mm × 178mm. The length of the copper tracks can be maximised by using a serpentine shape with the track positioned perpendicular to the incoming flow in order to minimise any conductive heat losses in the stream wise direction. The final design of the board with the copper tracks is shown in Fig.6.3. The access to the electrical connectors are provided in a single point, going right through the base material such that the current can be delivered from the rear of the PCB plate.

Uniform heating can be achieved by placing the tracks as close to each other as possible. The copper tracks are hence manufactured with a minimum track spacing of $s_{cu} = 0.1mm$ and a total length of $L = 31.22m$. The width of the copper tracks were set to $w_{cu} = 0.75mm$ and a design thickness of the tracks equals $t_{cu} = 0.035mm$. For a copper track of such dimensions,

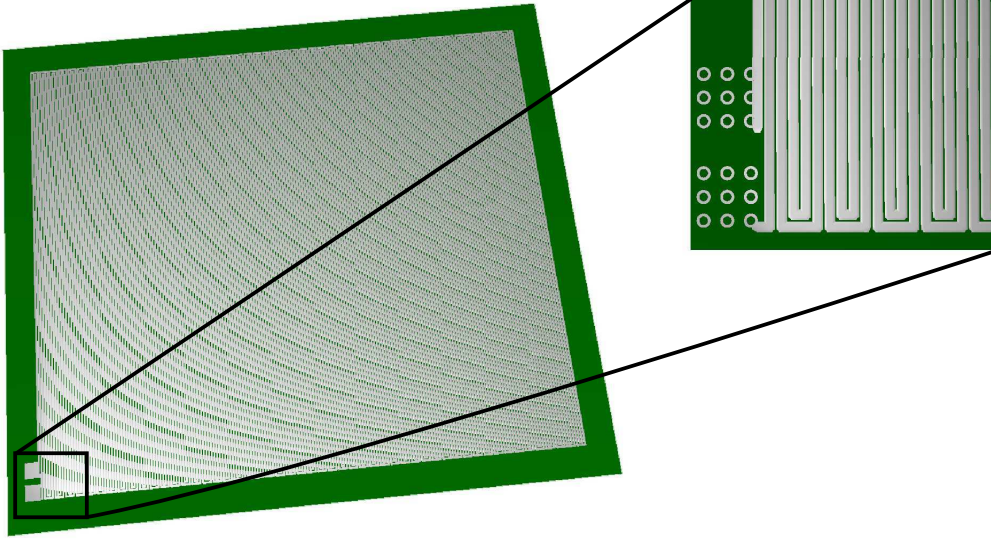


Figure 6.3: Printed Circuit board design showing the copper track arrangement (redrawn from Voogt (2017))

the electrical power generated can be given by Joule's heating as:

$$Q_{el} = I^2 R \quad (6.1)$$

In this equation, I is the current input to the PCB and R is the resistance offered by the copper tracks laid out on the PCB which in turn can be estimated using the equation:

$$R = \frac{\rho_{cu} L}{A} \quad (6.2)$$

where, L is the total length of the copper track, A is the cross sectional area and ρ_{cu} is the electrical resistivity of copper. The electrical resistivity is an intrinsic property of a material measured in Ωm which is dependent on the temperature of the material. The temperature dependency of resistivity can be approximated using the linear relation:

$$\rho_{cu} = \rho_{cu0} [1 + \alpha_{cu} (T - T_{ref})] \quad (6.3)$$

where, $\rho_{cu0} = 1.68 \times 10^{-8} \Omega m$ measured at the reference temperature of $T_{ref} = 20^\circ C$ and $\alpha_{cu} = 0.004041 K^{-1}$ is the temperature coefficient of resistivity for copper. Thus, by setting an appropriate input current, I through an external power supply the required heat input to the system can be achieved. The surface of the PCB is coated using a black solder mask to maximise its surface emissivity which was calculated to be equal to 0.87 by Voogt (2017).

An 8mm thick Makrolon[®] insulation slab (see Fig.6.4) is glued on to the other side of the PCB providing adequate insulation. Even though the Makrolon[®] slab is screwed onto the PCB plate, to ensure appropriate thermal contact throughout, an adhesive is essential. A Loctite bi-component epoxy based adhesive with a similar thermal properties as the PCB base material and Makrolon was used for this purpose. To improve adhesion, the surfaces are sanded and cleaned using ethanol. Glue is applied on to the PCB base and Makrolon which

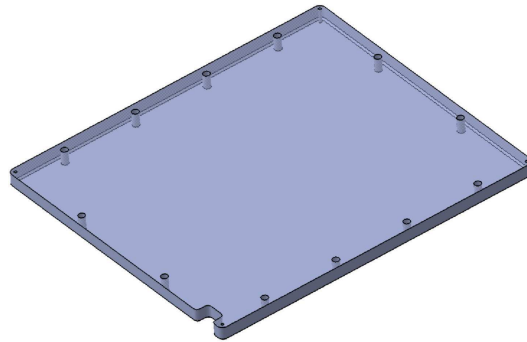


Figure 6.4: Makrolon® insulation slab (redrawn from Voogt (2017))

are then screwed and compressed using a beach vice. The glue is then allowed to cure for 24 hours thus ensuring proper contact.

The assembled test plate is mounted on to the custom built cavity door (see Fig.6.5) which then replaces one of the optical access of the ST-15 facility. The cavity door was milled from a single solid block of aluminium and acts as a thermal heat sink. The test plate, when bolted to the inside of the cavity door will form a uniform surface onto which the roughness elements can be attached. A 10mm hole was made available on the door through which electric power can be supplied to the test plate. The exact dimensions of the door can be found in Voogt (2017). While this door takes the place of one of the optical access, a Germanium window is attached to the other side of the test section, behind which the IR camera can be placed.

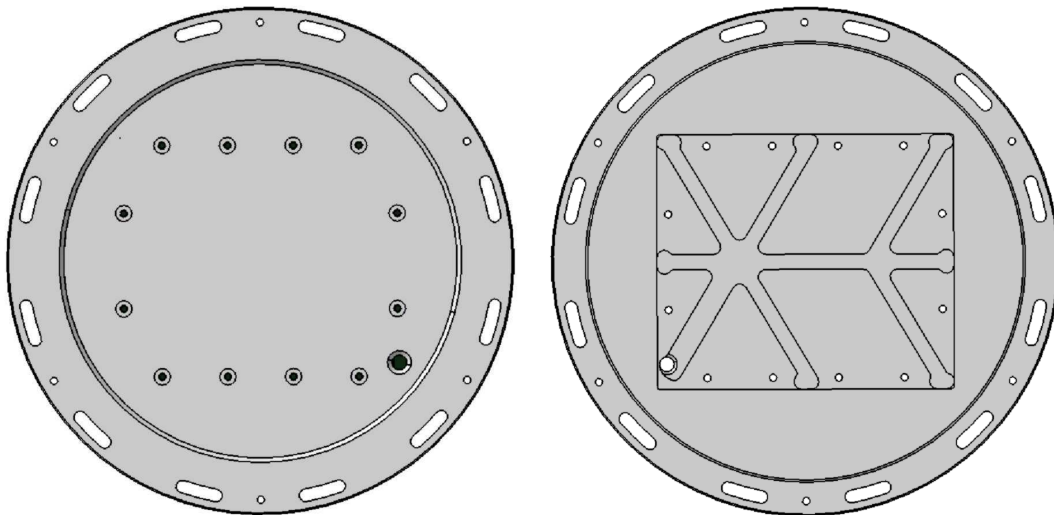


Figure 6.5: Cavity door outside (left) and inside (right) views (redrawn from Voogt (2017))

The CEDIP 530L IR camera was used to measure the temperature evolution on the model surface. However, since the dynamic range is different in this case, re-calibration of the camera with an integration time suitable for the expected range of temperature is necessary. An integration time of $205\mu\text{s}$ was set for this investigation with a camera acquisition frequency of 25Hz . Prior to a measurement, a Non-uniformity correction (NUC) and a bad pixel

replacement routine is carried out using the *Cirrus* software. Similar to the laminar case, the germanium window is also included in the calibration procedure to account for its reduced emissivity. For more details on the calibration procedure, refer Section 3.3.5

The electric power to the test plate was delivered by a Delta Elektronika SM600-10 laboratory power supply (see Fig.6.7) capable of delivering a maximum of 600V and 10A. To avoid overheating and cause any potential damage to the test plate, it was decided to deliver current to the test plate only during Tunnel ON condition. This was achieved by using an interlock connector inside the control room, so that the power supply can be switched on remotely after the tunnel is operated.

For each measurement, the wind tunnel is run for at least 45 seconds. While theoretically, the total temperature in the wind tunnel stays constant, because of the storage tank being located outside of the facility, small changes in the temperature occurs which needs to be accounted for. Thus during the wind tunnel run, the settling chamber temperature is recorded using a J-type thermocouple connected to a NI-9124 acquisition box at a frequency of $1Hz$. Both the IR and the temperature measurements were initiated simultaneously and hence a polynomial fit of the temperature data with time can be used for calculations of convective heat flux. The schematics of the QIRT experimental set-up is shown in Fig.6.6 and a picture of the same setup in the ST-15 facility is shown in Fig.6.7. The IR camera is placed on the other side of the tunnel and is hence not visible in the picture.

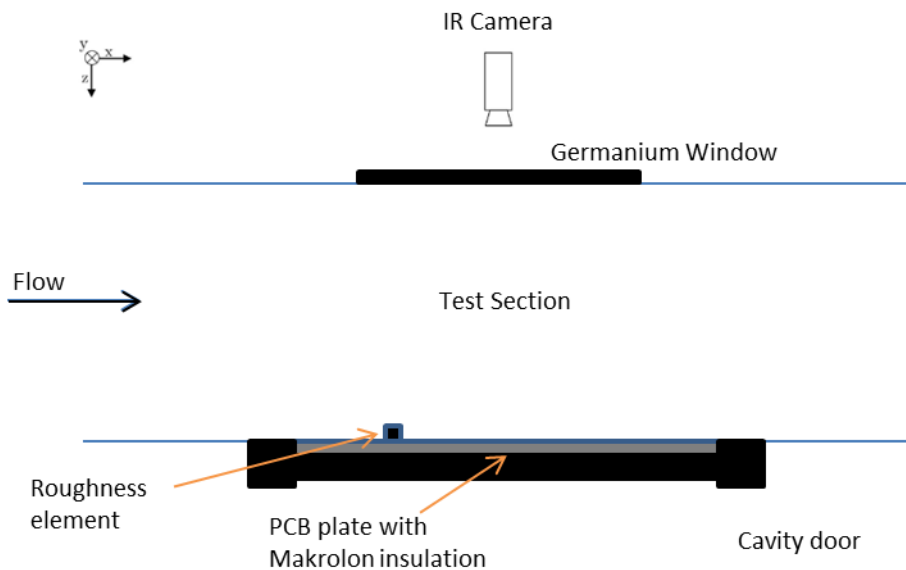


Figure 6.6: Schematic of QIRT Test Setup (Top View)

Unlike the previous campaign, the camera is placed at right angles to the Germanium window to cover the entire test plate within its field of view. To avoid any spurious reflections from any outside sources, the lens of the camera is covered with an aluminium cylinder and the entire camera is also covered with a black cloth. Also, to avoid any reflection from the metallic roughness elements onto the nearby regions, they were double coated with black paint. For the distance at which the camera was placed, an average resolution of $1.75 \text{ px} / \text{mm}$ was

obtained. Though relatively low, the discrete heat flux values obtained has a far greater spacial resolution when compared to the heat flux gauges used in literature. Even though the test plate is not viewed at an oblique angle, to have an accurate transformation of the coordinates, the DLT technique discussed in Section 3.4 was applied to all the processed images.

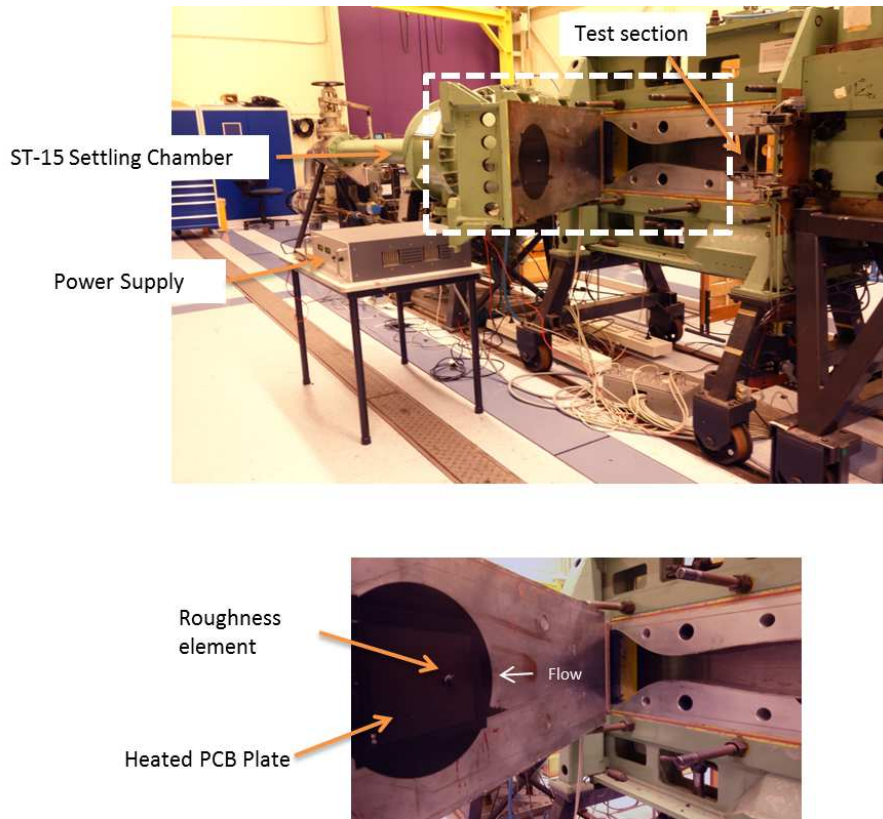


Figure 6.7: QIRT Test Setup in ST-15

6.4 Heat Flux Data Reduction

The heat flux data reduction technique utilised in the HTFD data, utilised the transient temperature data to calculate the heat flux through the [Cook and Felderman \(1966\)](#) technique. However, this requires the knowledge of the initial temperature of the test plate. The HTFD is a short duration facility where the measurement time is less than a second. Hence the initial temperature of the test plate will be equal to the ambient temperature of the environment. This may not be extended to the ST-15 because of its considerable long test duration, a substantial start-up time in addition to the inability to have a uniform initial temperature on the test plate during these phases. While it can be possible to cool the test plate to the adiabatic wall temperature to have a uniform initial condition, attempts to try to achieve that state failed even with a considerably long wind tunnel run time. Thus, the heat flux data reduction technique in use for this investigation makes use of the steady state condition of heat transfer.

6.4.1 Steady State Heat Transfer

The three dimensional transient heat conduction equation is given by:

$$\frac{\partial T}{\partial t} = \alpha \left(\frac{\partial^2 T}{\partial x^2} + \frac{\partial^2 T}{\partial y^2} + \frac{\partial^2 T}{\partial z^2} \right) \quad (6.4)$$

where, α is the thermal diffusivity of the material, equal to the ratio of the thermal conductivity (k) to the product of density (ρ) and specific heat capacity at constant pressure (c_p). However, if the system is under steady state condition, the temperature evolution will be independent of time and the Laplacian of the temperature will be equal to zero.

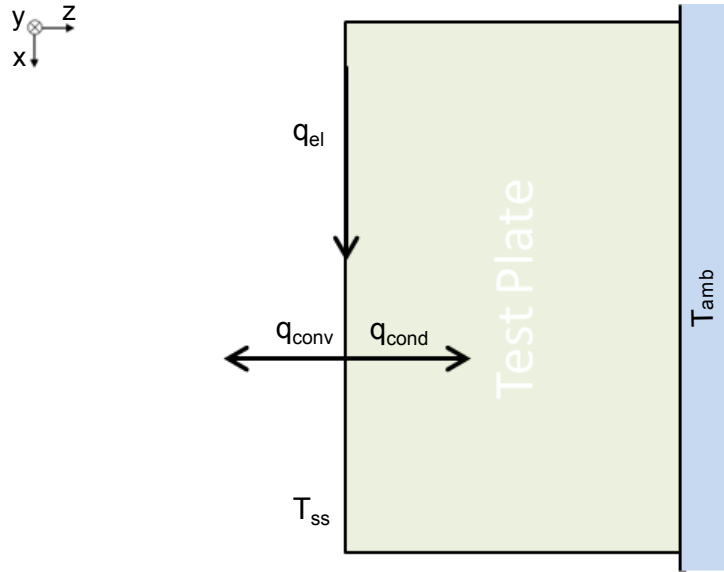


Figure 6.8: Schematics of steady state heat transfer problem

Fig.6.8 shows the schematic of the steady state heat transfer problem. The current input provided to the PCB generates heat due to Joule's effect. This heat is then dissipated through various means. Under steady state condition, there is a thermal equilibrium between the various heat transfer modes and hence, the thermal energy balance results in the expression:

$$q_{el} = q_{conv} + q_{cond} + q_{rad} \quad (6.5)$$

where, q_{el} , q_{conv} , q_{cond} and q_{rad} correspond to the heat flux due to electric heating, forced convection, conduction and radiation respectively. Rewriting Eqn.6.5, the convective heat transfer coefficient (h) can be directly calculated as:

$$h = \frac{q_{conv}}{T - T_{aw}} = \frac{q_{el} - q_{cond} - q_{rad}}{T - T_{aw}} \quad (6.6)$$

where, T and T_{aw} are the surface temperatures and adiabatic wall temperatures respectively. In the following sections, detailed discussion on the different steps carried out to determine the convective heat transfer coefficient will be carried out.

6.4.2 Image Preprocessing

For reasons to be discussed in the next section, it is essential that the field of view of the camera covers the entire flat plate, irrespective of the location of the roughness element. Thus it became necessary to place the camera normal to the germanium window and the test plate, causing unwanted reflection off the sensor of the camera (narcissus effect). An image preprocessing is hence carried out to reduce the effects of this reflection.

Prior to the measurements, there is no flow or heating of the test plate and hence, the test plate within the field of view is at equilibrium with the surrounding air. A set of frames are recorded in this condition, and will be called as the Unheated Empty Measurements (UEM). By subtracting the UEM with the heated measurement taken during the tests, the unwanted reflections from the sensors are mitigated. The frames before and after the application of the Image preprocessing routine can be shown in Fig.6.9. It can be seen that there is a substantial reduction in the severe camera reflection near the centre of the frame after the application of this routine. If this had not been applied, any data measured at the location would experience a reduction in its value, that cannot be corresponded to any flow phenomenon.

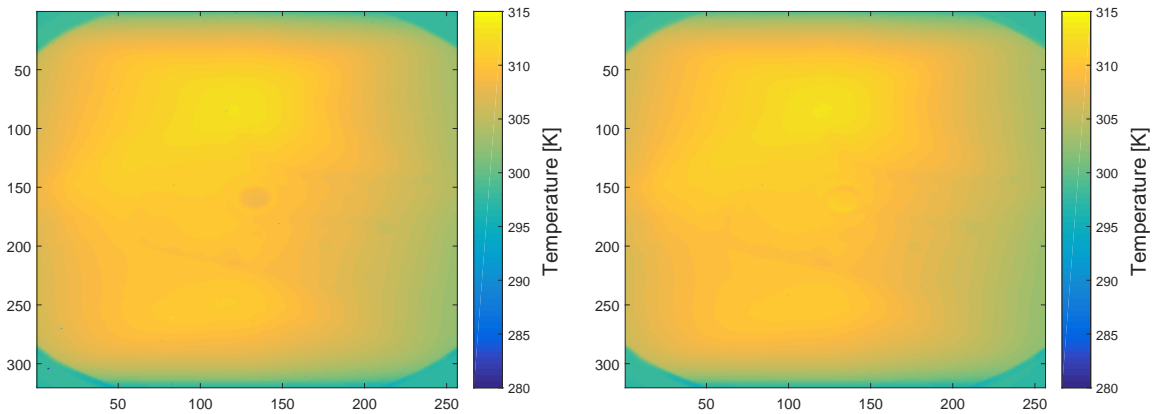


Figure 6.9: Frames before (left) and after (right) the application of Image Preprocessing Routine

6.4.3 Non Uniformity Heating Correction (NUHC)

The PCB used in the investigation consists of a FP-4 base material onto which a thin layer of copper tracks are laid. Due to faulty manufacturing technique and etching processes, the desired uniform copper thickness was never achieved and variations in copper thickness occurred. Since the resistance offered by the copper tracks is a function of the cross-section area, the non-uniform copper thickness across the board also results in a non-uniform heating when a current is passed through it. A perfect *heated thin foil* sensor should, in theory, experience uniform heating due to Joule's effect. Since, this was not the case with the printed circuit boards that were used in this analysis, a correction has to be applied to account for the non-uniform heating during the convective heat flux computation. This is calculated by monitoring the heated PCB in the absence of a forced convection (tunnel off condition) and these measurements will be known as Heated empty measurements (HEM).

Under a steady state condition in the absence of any forced convection, the same energy

balance equation discussed earlier can be applied, which is repeated here for convenience:

$$q_{el} = q_{conv} + q_{cond} + q_{rad} \quad (6.7)$$

If proper care was taken to avoid any forced convection, the only remaining way for the plate to lose heat from convection is by the process of natural convection, which for stagnant air under standard condition is a really small contribution when compared to the other heat transfer modes ($h_{natural} = 5W/m^2K$ for a vertical flat surface (Kreith and Manglik, 2016)). An order of magnitude analysis carried out by Voogt (2017) also revealed a negligible contribution of conductive heat transfer contribution for the same test setup. Thus, for the conditions discussed above, it can be said that:

$$q_{in} = q_{el} \approx q_{rad} \quad (6.8)$$

The above equation dictates that, in the absence of forced conduction, the ohmic heating applied on the plate is directly proportional to the radiation energy registered by the Infra-red camera. If the copper track thickness is considered to be a local property ($t_{cu}(i, j)$), then the local ohmic heating can be given by:

$$q_{el}(i, j) = R(i, j)I^2 \quad (6.9)$$

where the local resistance matrix $R(i, j)$ is equal to:

$$R(i, j) = \frac{\rho_{cu}L}{w_{cu}t_{cu}(i, j)} \quad (6.10)$$

The above expression provide the relationship between the ohmic heat energy and the thickness of the copper tracks. Combining them with Eqn.6.8, a direct relationship between the radiation intensity and the local copper thickness can be achieved:

$$q_{rad} \propto \frac{1}{t_{cu}} \quad (6.11)$$

Considering this relationship, the spacial variance in copper thickness can hence be evaluated by determining the spacial variance in the radiation energy registered by the IR camera. This correction matrix will later be applied to the electric heat flux to compensate during the convective heat flux determination.

The procedure carried out to determine this correction matrix is explained as follows.

- A small current was passed through the PCB under tunnel off conditions.
- The test section and the wind tunnel exit ports are sealed to make sure that there are no drafts convecting the heat away.
- Sufficient time is provided for the PCB to reach steady state condition. The steady state is verified by monitoring the transient temperature response from the IR camera.
- When steady state is reached, the radiation intensity distribution of the plate is recorded.

The non-uniformity heating correction (NUHC) is determined by first averaging the radiation intensity (E) over all the recorded frames. This makes sure that the inherent noise of the camera is mitigated. Once done, the spacial average of the radiation intensity over the entire surface area of the PCB board is computed (E_{avg}). The local scaling matrix is now the ratio of the specially averaged radiation intensity to the local radiation intensity.

$$NUHC(i, j) = \frac{E_{avg}}{E(i, j)} \quad (6.12)$$

This scaling matrix can now be used to convert the average copper track thickness (t_{cu}) into a local property ($t_{cu}(i, j)$) as follows:

$$t_{cu}(i, j) = t_{cu} \times NUHC(i, j) \quad (6.13)$$

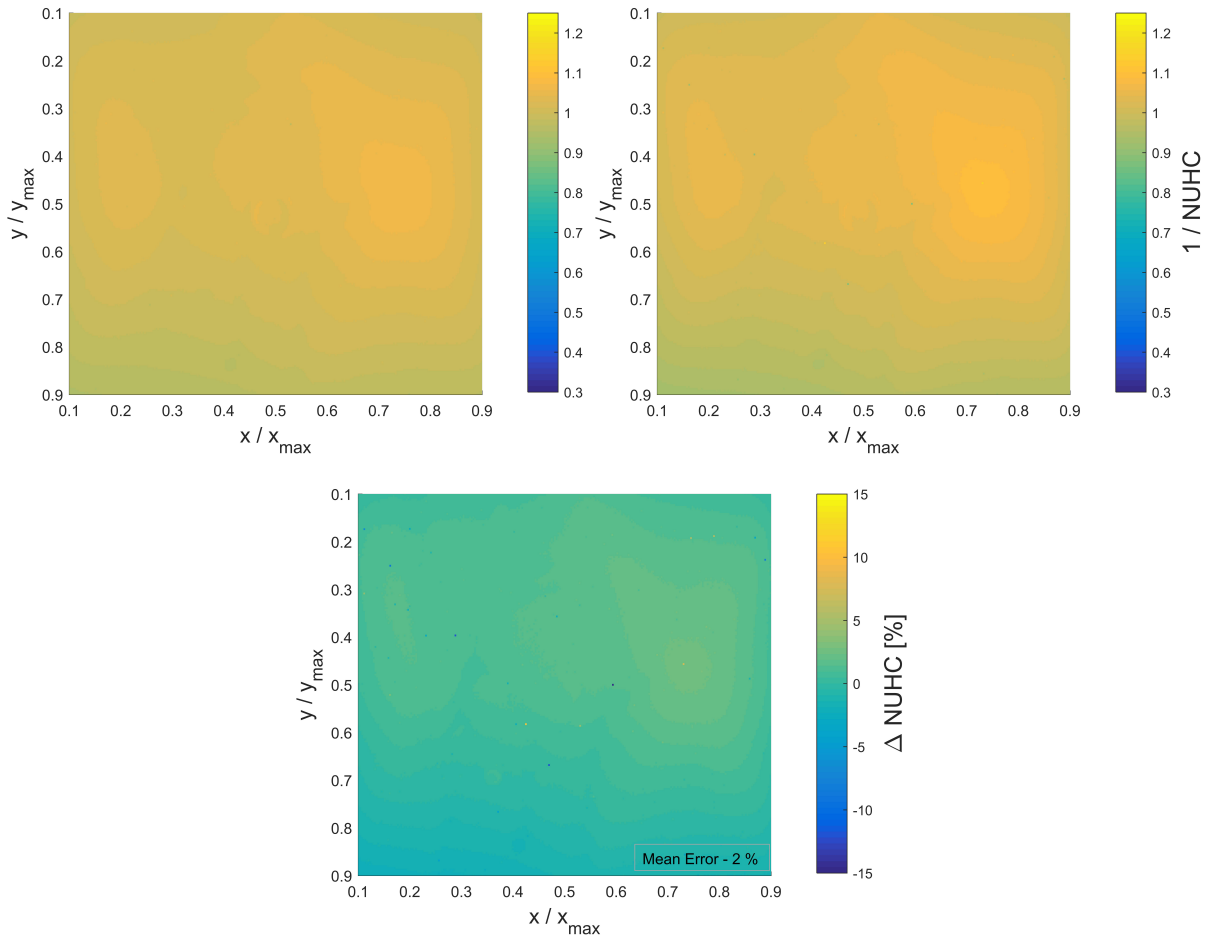


Figure 6.10: Non-uniform heating correction corresponding to $I = 0.7A$ (Top Left) and $I = 0.85A$ (Top Right) along with the spatial variance

To have an accurate estimate of the specially averaged radiation intensity, the entire test plate is required to be in the field of view. The NUHC matrix, computed for the test plate at two different input current levels is shown in Fig.6.10

While it is evident that the NUHC should be independent of the input electric heat, an analysis was carried out to verify the same. In Fig.6.10, the NUHC matrix corresponding to two different power settings are shown. It can be seen that the localised hot spots are the same in both the images. A mean variance of less than 2% was computed, revealing the negligible effect of the power setting on the correction matrix. Also, since the correction matrix is now computed and applied, these non-uniform heating effects will now become invisible in the convective heat transfer coefficient distribution.

6.4.4 Transient Temperature analysis

The energy balance equation stated in the previous section can only be applied when the system under consideration is in a steady state condition. So, before the different heat flux terms can be computed, the steady state frames of the test has to be extracted. Fig.6.11 (left) shows a sample temperature response for the entire duration of the run. The curves correspond to the temperature averaged over $5px \times 5px$ at different locations in the wake. The IR camera is triggered manually right before the start of the wind tunnel. After about 2 seconds, the wind tunnel is started, while leaving the power supply to the PCB turned off. This can be seen as a dip in the temperature due to the cooling of the board by the flow. The power supply is now turned on using the interlock and the temperature in the plate starts to increase tending towards the steady state condition. Towards the end of the test, the temperature eventually starts to dip because of the changes in the settling chamber temperature and drop drastically when the power supply is switched off.

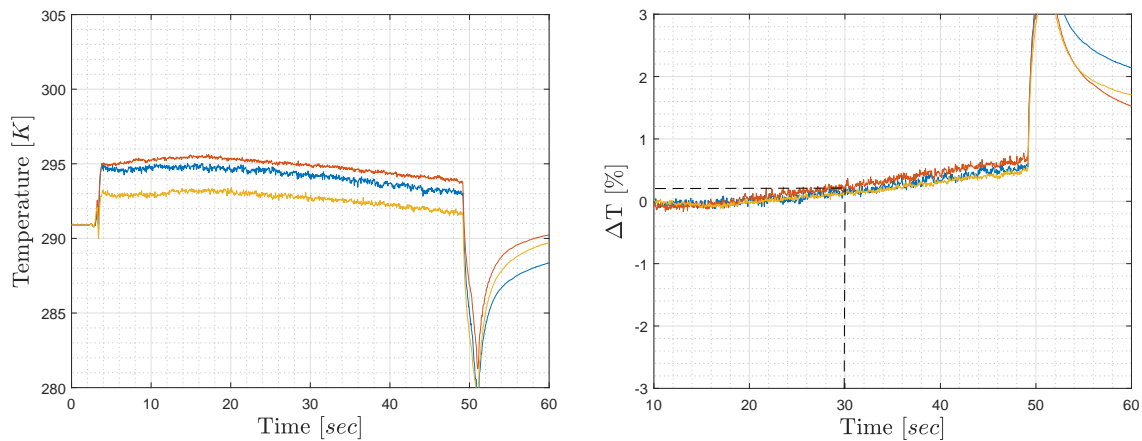


Figure 6.11: Transient temperature response at different locations on the PCB (left) and extraction of steady state frames (right)

The temperature variation from $t = 10s$ is also shown in Fig.6.11 (right) where one can see a negligible temperature increase in the initial part of the curve. Accepting an error of 0.2%, the corresponding steady state frames are extracted for the calculation of heat transfer coefficient. For all the measurements taken for this investigation, on average, the steady state condition was maintained for about 15 seconds, corresponding to about 375 frames out of the measured 2000 frames.

6.4.5 Heat flux computation

Now that the recorded frames are pre-processed, and the steady state frames are extracted, the heat flux terms in the energy balance equation can be determined.

Electric heat flux

The electric heat flux due to Joule's heating effect is given by

$$q_{el} = \frac{I^2 R}{A} \quad (6.14)$$

where, A and R are the surface area the resistance of the PCB respectively. While this simple relation is applicable for a perfect PCB, due to the inherent non-uniformities, the resistance has to be corrected and is given by,

$$R(i, j) = \frac{\rho_{cu}(i, j) \cdot L}{w_{cu} \cdot t_{cu}(i, j)} \quad (6.15)$$

where, the resistivity ρ_{cu} and the copper thickness distribution $t_{cu}(i, j)$ are given by:

$$\rho_{cu}(i, j) = \rho_{cu_0} [1 + \alpha_{cu}(T_{ss} - T_{ref})] \quad (6.16)$$

$$t_{cu}(i, j) = t_{cu} \times NUHC(i, j) \quad (6.17)$$

For the test plate used in this investigation, the room temperature average resistance was equal to 24.9Ω . However, due to the local variation in copper thickness, this measured average resistance cannot be applied to the entire PCB board and the NUHC has to be applied. The current I in Eqn.6.14 corresponds to the recorded value for each wind tunnel run from the power supply.

Conductive heat flux

The application of Infra-red Thermography, which provides a 2 dimensional temperature distribution has enabled the researches study the 2D effects which otherwise would have been quite tedious to estimate. For a heated thin foil for made of an isotropic material, the heat flux due to tangential conduction can be give by (Carlomagno et al., 2014):

$$q_{cond,s} = -sk_f \nabla^2 T_{ss} \quad (6.18)$$

where, s and k_f are the thickness and the thermal conductivity of the thin foil. This expression however, as stated earlier is application only for a thin foil made of an isotropic material, like a thin sheet of metal. For the PCBs use in this investigation, direct application of this expression may not be possible owing to the anisotropic natures on either direction of the board. Hence it is modified as:

$$q_{cond,s} = - \left(k_{xx} \frac{\partial^2 T_{ss}}{\partial x^2} + k_{yy} \frac{\partial^2 T_{ss}}{\partial y^2} \right) \quad (6.19)$$

where, k_{xx} and k_{yy} are the thermal conductivities of the PCB respectively along and perpendicular to the flow direction. The conductivities of this anisotropic material can be determined by following Astarita and Cardone (2000) and Voogt (2017) as described below.

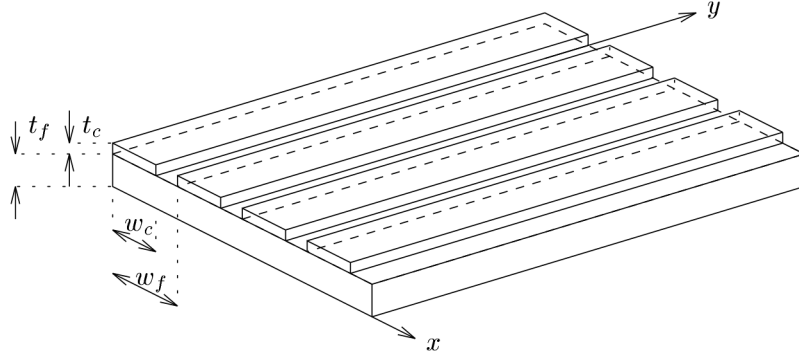


Figure 6.12: Sketch of the PCB (Voogt, 2017)

Fig.6.12 shows the sketch of the PCB with the copper tracks laid on top of the FR-4 base material. w_{cu} and w_f correspond to respectively the width of the copper tracks and FR-4 material, while t_{cu} and t_f are their respective thickness. For such a layout, the thermal conductivity in the y direction can be given by Astarita and Cardone (2000):

$$k_{yy} = \gamma^* t_{cu} k_{cu} + t_f k_f \quad (6.20)$$

where, $\gamma^* = w_{cu}/w_f$ is the ratio of copper track width to the FR-4 material width and k_{cu} and k_f are the thermal conductivities specific to the material. However along the x direction, which is perpendicular to the copper track direction, conduction alternates between the copper track and the FR-4 material. The resulting thermal conductivity is given by (Voogt, 2017):

$$k_{xx} = \frac{1}{\left[\frac{1-\gamma^*}{t_f k_f} + \frac{\gamma^*}{t_f k_f + t_{cu} k_{cu}} \right]} \quad (6.21)$$

The remaining unknown in Eqn.6.19 is the Laplacian of the temperature field. Approximate numerical differentiation methods can be employed to calculate the necessary partial differential terms. A fourth order central difference scheme applied to the temperature field, will yield the expression:

$$\left. \frac{\partial^2 T}{\partial(x,y)^2} \right|_{(x,y)_i} = \frac{-T_{i-2} + 16T_{i-1} - 30T_i + 16T_{i+1} - T_{i+2}}{12\Delta(x,y)^2} + \dots \quad (6.22)$$

where Δx and Δy correspond to the physical distance between adjacent pixels. While this expression provides the means to calculate the necessary heat flux, the infrared scanner used in this investigation suffers from temporal random noise which is unavoidable. When using the numerical integration schemes, these noises can be amplified (Carlomagno et al., 2014). In fact, such amplification was also visible in the extensive analysis carried out by Voogt (2017) using the same set-up where the heat transfer profiles of cavities in a supersonic flow was investigated. However, upon investigating the heat transfer coefficient profiles with and without the contribution of the surface conductivity, an average percentile change of 3.52% was observed along with discontinuities and non-physical heat transfer coefficient profiles. This difference was consistent with the estimates of Carlomagno et al. (2014) who expected an uncertainty of 4% for a printed circuit board design. Hence following the conclusions of

Voogt (2017), to avoid non-physical heat transfer coefficient profiles, the surface conductivity values are discarded from the calculations.

Because of the temperature difference between the surface of the PCB and the cavity door which acts as a heat sink, maintaining an ambient temperature, any heat flux though the test plate also needs to be evaluated. During his measurements, Voogt (2017) placed 17 reference thermocouples, distributed throughout the rear of the test plate and simultaneously recorded the temperature during the wind tunnel run. However, based on his final estimates, the conduction loss through the test plate contributed to only about $4.44 \times 10^{-5}\%$ of the total heat flux terms, which is negligible. Thus this term is not included in computing the convective heat transfer coefficient.

Radiative Heat Flux

Any object above absolute temperature loses energy in the form of radiation. Hence these terms also need to be taken into account in the energy balance. The radiative heat flux takes the form:

$$q_{rad} = \epsilon_{PCB} \cdot \sigma \cdot (T_{ss}^4 - T_{aw}^4) \quad (6.23)$$

where $\epsilon_{PCB} = 0.87$ is the emissivity of the printed circuit board and $\sigma = 5.670367 \times 10^{-8} \text{Wm}^{-2}\text{K}^{-4}$ is the Stefan-Boltzmann constant, while T_{aw} is the adiabatic wall temperature, evaluated using the expression,

$$T_{aw} = T_0 \left[\frac{1 + rM_e^2(\gamma - 1)}{1 + M_e^2(\gamma - 1)} \right] \quad (6.24)$$

It was observed previously that due prolonged runtime of the facility, the total temperature begins to drop. Hence, a separate thermocouple measurement was made, assessing the flow in the settling chamber at the same time the IR measurements were made. Thus the adiabatic wall temperature is not a constant quantify and is specific to the particular wind tunnel test. The recovery factor (r) in this expression correspond to the turbulent boundary layer and is equal to the third root of Prandtl number:

$$r = \sqrt[3]{Pr} \quad (6.25)$$

6.4.6 Heat flux Normalisation

Upon calculating the convective heat flux (q_{conv}) though the data reduction technique that was discussed in the previous section it can be normalised through the Stanton number, which is defined as:

$$St = \frac{h}{\rho_e u_e c_p} \quad (6.26)$$

with the convective heat transfer coefficient (h) equal to:

$$h = \frac{q_{conv}}{T_{ss} - T_{aw}} \quad (6.27)$$

The flow density (ρ_e), velocity (u_e) are evaluated using the knowledge of the measured temperature and pressure in the settling chamber, and the free stream Mach number. The specific heat at constant pressure (c_p) for air equals 1.004 kJ/kg.K and is quite invariant with temperature for the range considered here. However, following the literature, the convective heat transfer coefficients can also be normalised using h^* which is defined as:

$$h^* = \frac{h}{h_{turb}} \quad (6.28)$$

with h_{turb} equal to the local turbulent heat transfer coefficient. This way, the level of heat transfer with respect the reference turbulent case can be directly interpreted, providing a direct idea about the level of perturbation exhibited by the roughness element.

6.4.7 Uncertainty Analysis

A separate uncertainty analysis corresponding to the data reduction in this part of the thesis has to be carried out to understand the limitations of the results that will be presented in the next chapter. Reviewing the standard method of uncertainty of Moffat (1988), the uncertainty of a parameter Y can be given as:

$$\delta Y = \sqrt{\sum_{i=1}^N \left(\frac{\partial Y}{\partial X_i} \delta X_i \right)^2} \quad (6.29)$$

where, X_i are the independent variables that are used to derive the parameter Y, with δX_i being the uncertainty associated with their estimation. The possible sources of error in the data collected during the QIRT campaign include those involved with the measurement equipment and devices, an error in temperature estimation from calibration procedure due to inhomogeneity of the black body simulator and an error in heat flux estimation due to deviation in material and free stream properties.

The CEDIP IR camera, which was also used in this investigation has an NETD of 0.025K. During the calibration procedure, the temperature of the black body was measured using a National Instruments NI-9124 acquisition box with an uncertainty of 0.365K as specified by the manufacturer. In addition to this, the black body simulator exhibited an average non-uniformity of 0.294K during the course of the calibration procedure. Combining all these, an uncertainty in the temperature measurement during the calibration procedure is equal to 0.469K.

Similar to the laminar case, the property of the material could possibly vary due to the variations in temperature during the course of the measurement, which would result in an uncertainty in the heat transfer estimates. In his experiment, Voogt (2017) utilised reference thermocouple measurements to estimate the conductive losses and concluded that such losses account for a negligible contribution to the total heat flux. Thus any uncertainty in the conductive heat flux estimation with respect to material property variation can also be safely excluded from consideration.

The SM600-10 laboratory power supply has an uncertainty of 0.005A as reported by the manufacturer, while the Fluke 116 multimeter estimates the resistance of the PCB with

an uncertainty of 0.9%. Though the stagnation temperature was estimated real time to minimise any uncertainties in free stream properties, it is still limited by the uncertainty of the thermocouple acquisition box. Combining all these effects, the total uncertainty in the convective heat transfer coefficient was determined to be within 5.10%. This also includes the repeatability of the experiment, which was estimated to be 1.24% by Voogt (2017).

6.5 Schlieren Setup

The working of a simple Z-type schlieren technique was previously discussed in Section 3.1. In this section, the set-up of the Schlieren along with the technique used to detect the shock position will be discussed.

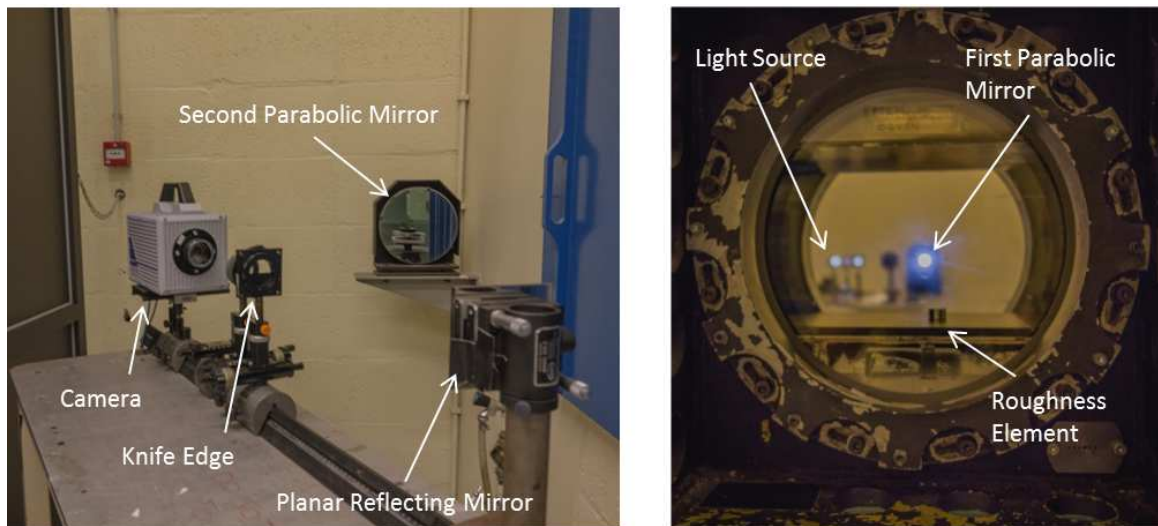


Figure 6.13: Schlieren setup in ST-15 showing the camera and knife edge (left) and a view through the test section with the light source in the background (right)

The arrangement of the Schlieren set-up at the ST-15 facility can be seen in Fig.6.13. A continuous light source was used at the maximum possible intensity, allowing measurement to be taken at very high acquisition rate and at a very fast shutter speed. A fast shutter is necessary since the shock system that was measured is very unsteady in nature. The light that is entering the camera is essentially averaged during the exposure time and hence a shorter time freezes the shock in place. A horizontal knife edge configuration was used such that the system is sensitive to the gradients in the vertical direction. The pin hole aperture was limited to 3mm . Though it was possible to go lower, it was decided to not use the smallest diameter since that makes the system extremely sensitive to even the slightest gradients. The pin-hole was also covered with a translucent tape to avoid the image of the lamp falling on the camera and to improve the quality of the obtained image.

Images were acquired using a Photron Fastcam SA1.1 which has a CMOS sensor with a pixel pitch of $20\mu\text{m}$ and capable of delivering a monochrome light sensitivity of 10,000. For all the roughness element, two measurements were taken - one covering the global field of view at 6250 fps with each frame exposed for $25\mu\text{s}$ and a second at a much higher frame rate of

62500 fps with an exposure time equal to $1.7\mu s$, focusing upstream of the cylinder. The first measurement set was necessary to gain an idea about the nature of the lambda shock system upstream and to choose the FOV for the second measurement set. To improve the contrast of the images, before every measurement, a *shading* or *Black Level* correction is applied using the PFV camera software which corrects for sensor bias. The details of both the measurement sets are summarised in Table 6.3.

Table 6.3: Detail of Schlieren Measurement Campaign

Parameter	Measurement Set 1 (Global)	Measurement Set 2 (Upstream)
Light source	Continuous	Continuous
Knife edge	Horizontal	Horizontal
Exposure time [μs]	25	1.7
Frame rate [fps]	6250	62500
Resolution [$px \times px$]	896×496	256×272
Resolution [mm/pixel]	0.205	0.213

6.5.1 Shock Position Detection

The shock system upstream of the cylindrical element is known to be extremely unsteady. Previous studies have attempted to study the unsteadiness of the shock system using wall-pressure measurement which is restricted to a single point and fails to capture the motion of the shock completely. In this investigation time resolved Schlieren, coupled with digital image precessing and computer vision techniques are employed to accurately detect the position of the shock and its oscillations with time.

Each upstream measurement was recorded at an acquisition rate of 62500 fps with a very small exposure time to avoid large scale blur due to the shock motion. This requirement reduced the quality of the image to a certain extent and hence the image first has to be improved before applying the shock detection algorithm. The summary of the procedures used is shown in Fig.6.14.

For each test image, a background image is recorded at tunnel off condition. 2D discrete fourier transforms are applied to both the images and subtraction is carried out as the first step to enhance the image and remove any background noise (Estruch-Samper et al., 2008). Once the image is transformed back to the spacial domain, by applying an inverse transform, further contrast enhancements can be achieved by stretching the intensity limits of the image such that, minimum and maximum intensity values in the image represent the lowest and the highest intensity limits in the scale. Upon application, one can see obvious improvements in the image contract. A 2D gaussian filter is applied to smooth out the image after which, the Sobel's edge detection algorithm (Gonzalez et al., 2009) was used to detect the sharp gradients, in this case the shock wave.

To make sure that only the large gradients are detected, a suitable threshold is applied to the Sobel's algorithm, which isolates the gradients of highest intensity and displays them in

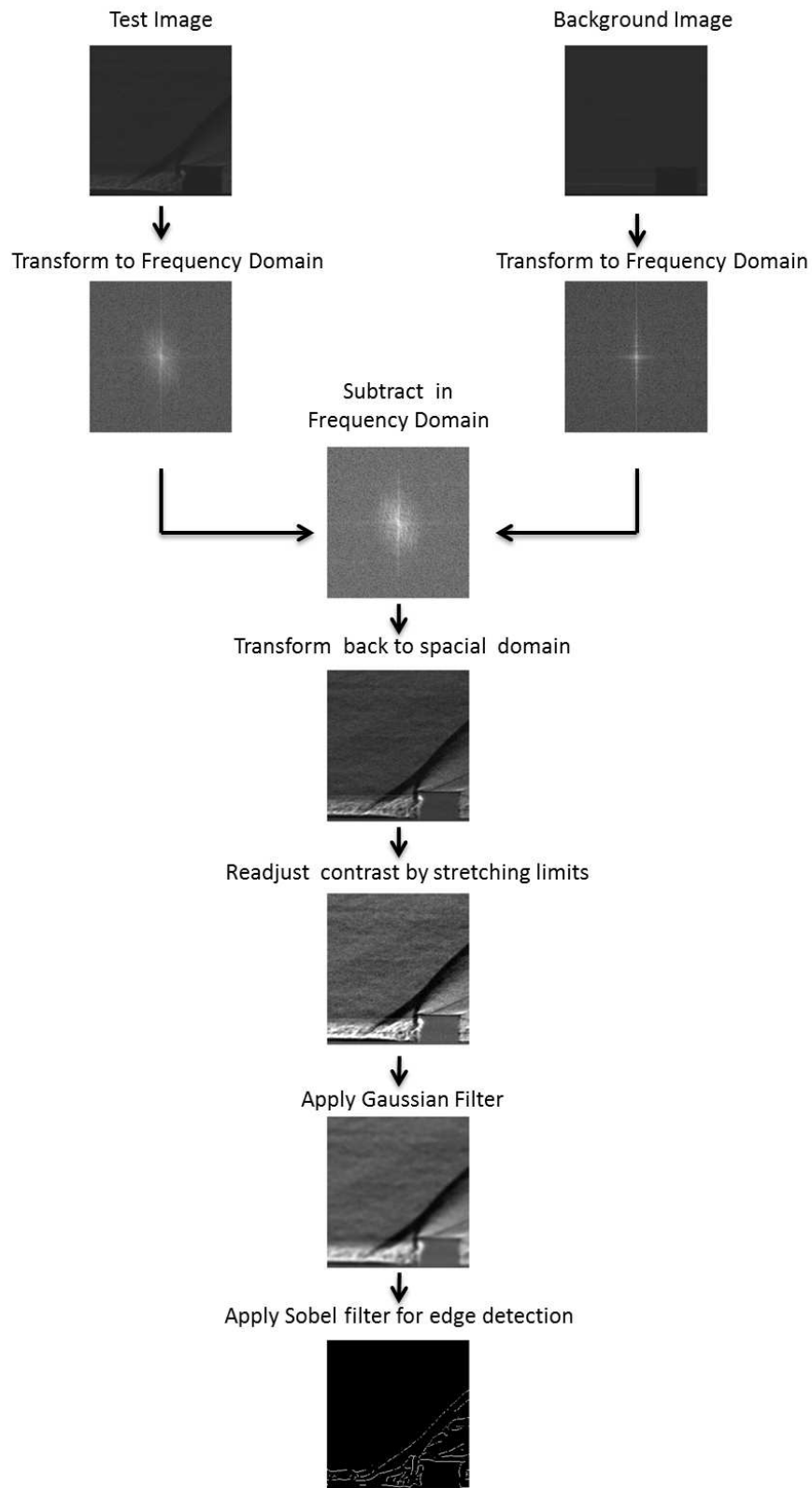


Figure 6.14: Image Processing Routine for Shock Detection

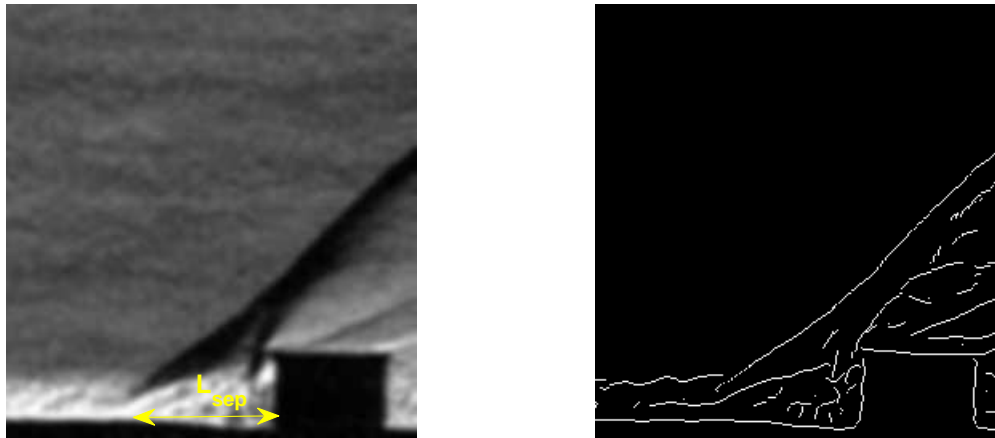


Figure 6.15: Processed Schlieren image (left) and the corresponding binary image (right)

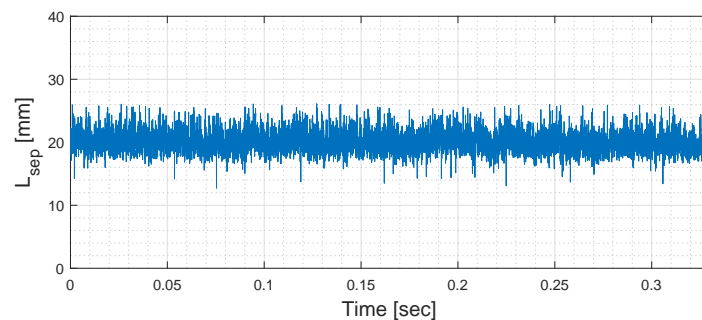


Figure 6.16: Sample position plot of the upstream separation region

binary form. Fig.6.15 shows the final processed image after subtraction and the corresponding binary image. Notice how the algorithm was able to smoothly track the upstream shock wave in the binary image.

The binary image once obtained can be used to track the location of the shock along every pixel, normal the wall of the test section. A linear regression can then be applied to determine the point at which the shock would hit the wall of the test section which determines the separation point. The horizontal distance between the separation point to the foot of the cylinder (see Fig.6.15) can then be directly estimated and tracked with time. A sample time resolved upstream separation distance (L_{sep}) is shown in Fig.6.16.

Chapter 7

Shock Unsteadiness and Surface Heat Transfer

In this chapter, the results pertinent to the interaction of the cylinder with the incoming turbulent boundary layer will be discussed. Similar to the laminar case, the undisturbed boundary layer is first discussed, followed by the 2D and sectional plots of heat transfer profiles. Finally, the results of shock unsteadiness is discussed along with an assessment of the upstream separation distance.

7.1 Undisturbed boundary layer

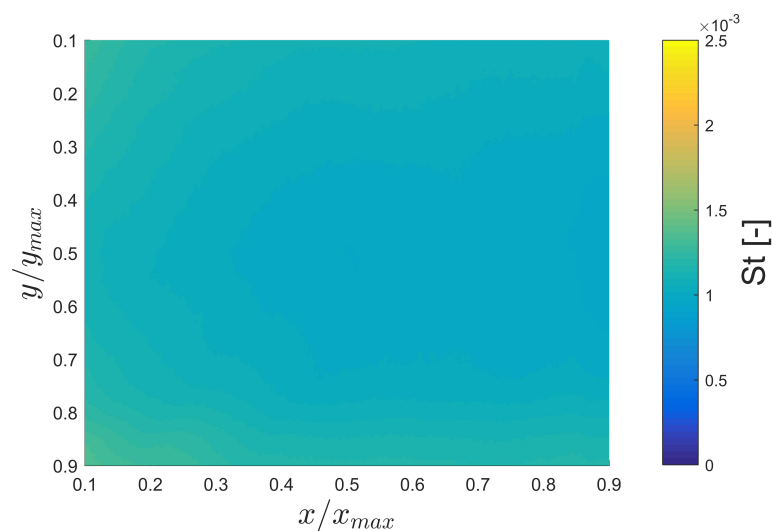


Figure 7.1: Flat plate Undisturbed Boundary Layer

Before the results of the interaction is presented, the undisturbed boundary layer is first assessed. Even though there was non uniform heating of the plate due to variation in copper

thickness, the incorporation of the NUHC should result in a near uniform Stanton number distribution across the area of the plate. Fig.7.1 shows the Stanton number distribution across the plate in the absence of any elements. x and y are the stream wise and span wise coordinates and are non dimensionalised with respect to the maximum length and breadth of the plate respectively. As expected, it can be seen from the figure that the distribution is nearly uniform with a mean value of $St = 0.00109$. Giepman et al. (2014) performed boundary layer assessment using PIV in the same facility and obtained estimates of surface skin friction coefficient (C_f). Modified Reynolds analogy can be used to relate the experimentally calculated skin friction coefficient to Stanton number as:

$$St = \frac{C_f}{2} Pr^{-2/3} \quad (7.1)$$

where, $Pr = 0.71$ is the Prandtl number. The streamwise variation of the Stanton number is plotted against the value obtained from this relation and is shown in Fig.7.2. A near uniform distribution can be seen with the exception of the leading section of the plate. This could be due to some small discontinuity in the junction between the test plate and the wind tunnel wall that may have disturbed the boundary layer locally. However, as the boundary layer settles down, the heat flux also tends to maintain its near uniform distribution. A 9% deviation was observed in the Stanton number values which could be due to possible deviation in the environmental conditions. While Giepman et al. (2014) reported a constant stagnation temperature of $T_0 = 290K$, in the present study the real time stagnation temperatures were recorded and included in the calculations.

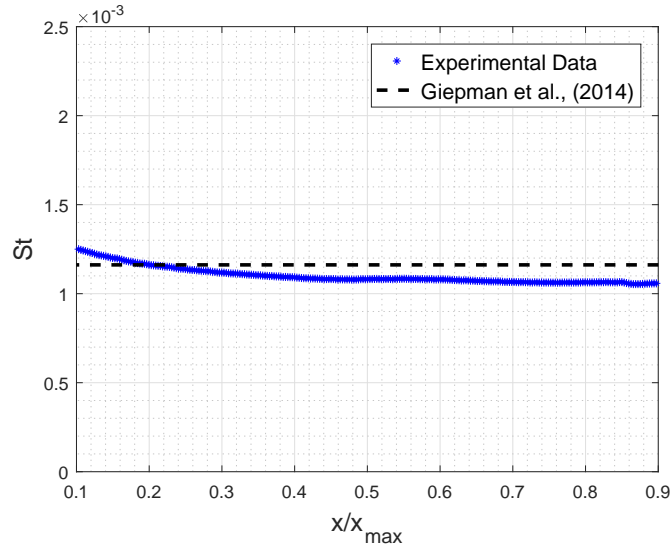


Figure 7.2: Flat plate Undisturbed Boundary Layer

Table 7.1: Comparison of mean undisturbed boundary layer Stanton number

	Current Study	Voogt (2017)	Giepman et al., (2014)	Tambe et al., (2017)
$St [-]$	0.00109	0.00111	0.00119	0.00119
ϵ_{St}	-	1.84 %	9.17 %	9.17 %

A summary of the comparison of the measured Stanton number with the literature is shown in Table 7.1. The Stanton number values from Giepman et al. (2014) and Tambe et al. (2017) are from PIV measurements coupled with Reynolds analogy, while data from Voogt (2017) had directly been measured from the same facility and experimental set-up. The Stanton number values compares very well with Voogt (2017) and is within the measurement uncertainty. This assessment and comparison provides validation of the measurement set-up and the data reduction routine.

7.2 Global Flow Features

Before entering into discussions on the effect of the cylindrical element on the heat transfer profile, a description of the global flow features around the cylinder is provided in the section. Fig.7.3 shows the Schlieren and Oil flow images taken for the H10 D15 cylinder. To have clarity, both the images are aligned with respect to the leading and trailing edges of the cylinder (labels 4 and 5 respectively). While the Schlieren images provides a *side view* visualisation of the features, the oil flow images shows the *top view* of the interaction region. Hence, when combined, the 3D flow topology could be interpreted.

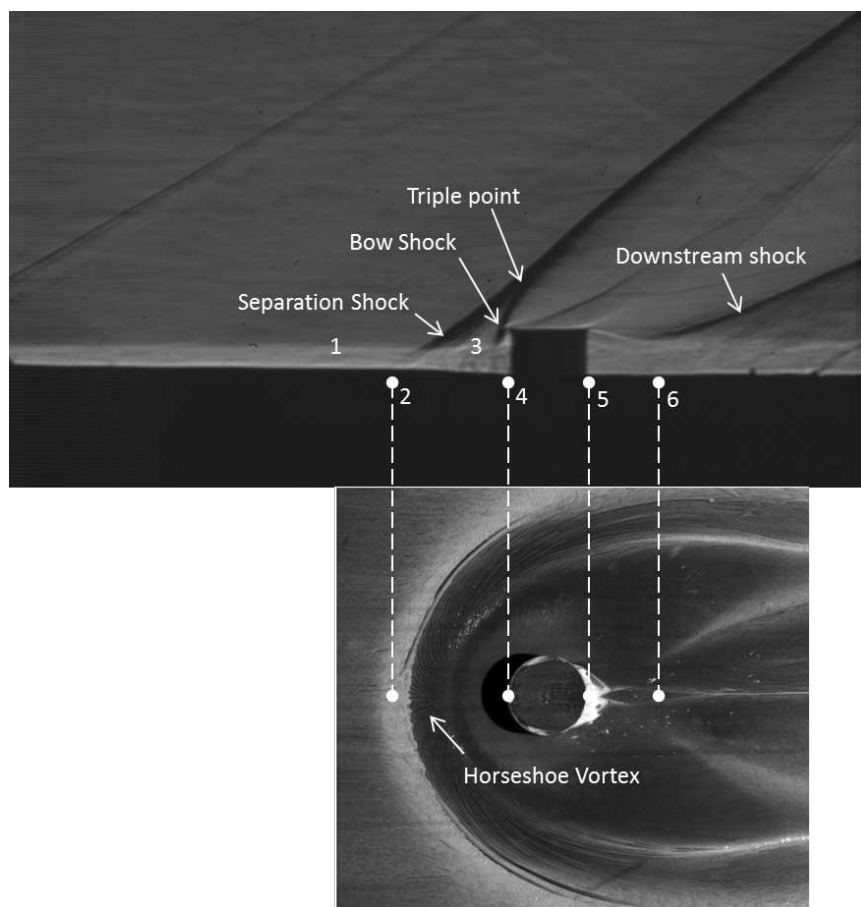


Figure 7.3: Global flow features for H10 D15 Cylinder. Images are from Schlieren (Top) and Oil Flow visualisation (Bottom). Flow is from left to right.

In the figure, the different flow features in the Schlieren and Oil flow images are labelled and align quite well. The incoming boundary layer is turbulent in nature and is visualised in the schlieren image as a bright band (1) close to the wall due to the higher density gradients when compared to the free stream air. Upon interacting with the cylindrical element, a system of shock waves are formed. First there is the separation shock, which is formed due to flow separation upstream of the element. Following the discussions of [Lighthill \(1953\)](#), when the undisturbed boundary layer first encounters the roughness element, it experiences an adverse pressure gradient due to which it starts to thicken. If the adverse pressure gradient is larger, as in this case, it may lead to separation of the boundary layer with the formation of the separation shock to deflect the streamlines upwards. The separation point is marked as (2) in the figure and corresponds with the separation point located in the oil flow image, which is represented by a thick bright line upstream of the cylinder. The thick bright line is formed because of oil tending to accumulate near separation. Since the schlieren image only shows a 2D image of the phenomenon integrated over the spanwise direction, the separation shock is seen to be a single line. However, in practice it is three dimensional in nature that curves around the cylinder as can be seen with the separation line in the oil flow image, wrapping around the cylinder.

With the height of the element greater than the local boundary layer thickness, a part of the element is exposed to high Mach number flows and hence results in a bow shock wave, just upstream of the front face of the cylinder. The bow shock wave curves downstream when moving in the wall normal direction and interacts with the separation shock at the triple point. The separation shock and the bow shock wave together form the lambda-shock system widely reported in literature.

Moving to the rear of the element, the flow tends to reattach to the wall after having been turned away from the wall by the element. A downstream shock wave is observed (6), which tends to deflect the streamlines and align the streamlines parallel to the wall ([Marxen et al., 2010](#)). The oil flow image also shows the surface features caused due to the presence of this shock wave.

In the region between the separation shock and the front face of the cylinder, a large recirculation region is observed (3). This region is characterised by a primary horseshoe vortex which is clearly visible in the oil flow image and is seen to wrap around the cylinder, similar to the laminar case. Also to be noted is that the resulting surface features are symmetric with respect to the centreline. Far downstream of the interaction region, the boundary layer is observed to be thicker than the incoming undisturbed boundary layer, indicating that the current measurement domain might not have been large enough for the perturbations from the interactions to settle down and recover to the initial conditions.

7.3 Surface Heat transfer

A study of heat transfer profile in the wake of the cylinder, due to its interaction with an incoming turbulent boundary layer will be carried out in this section. Similar to the laminar case, the 2D heat flux distribution will be discussed, assisted by the sectional plots in the stream wise and span wise directions. During the measurement campaign, the Delta Elec-

tronika SM600-10 power supply used to provide current to the PCB failed and no immediate replacement could be found. This resulted in failure to gather data for three of the 9 test cases that were planned originally. The missing data correspond to one case in H8 cylinder (H8 D1125) and two cases in H10 cylinder (H10 D1125 and H10 D15).

7.3.1 Centreline Stanton number variation

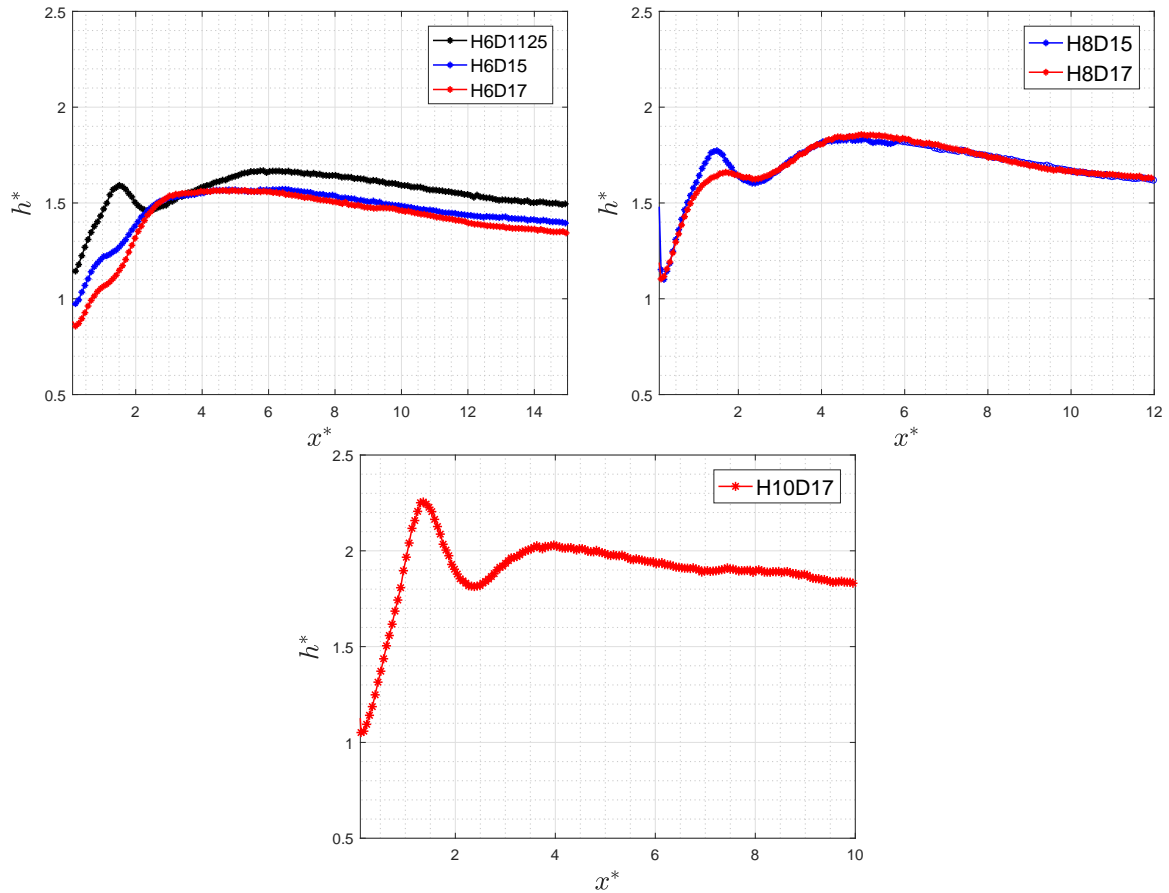


Figure 7.4: Centreline heat transfer variation for H6 (Top left), H8 (Top Right) and H10 (Bottom) Cylinders

Fig.7.4 shows the centreline heat flux distribution in the wake region downstream of the cylindrical elements of all the three heights. Similar to the laminar case, the coordinate x^* correspond to the streamwise distance scaled with height of the cylinder, with origin at the trailing edge of the element.

At first observation, it can be seen that the heat transfer in the wake of the cylindrical element is nearly 1.5 - 2 times the local reference turbulent heat transfer. The heat transfer values also in general tends to increase with height of the roughness element with a centreline maximum found for roughness geometries of height $H = 10mm$. Since these plots are normalised with respect to the local flat plate turbulent heat transfer, it can directly be interpreted to gain an understanding of what geometries induces higher perturbation in the flow because of the presence of the element. Given that the heat transfer is higher for the tallest cylinder, it can

be concluded that the highest cylinder is more effective in perturbing the flow. For the H6 case, the heat transfer variation with diameter is largely invariant except for the reattachment point. This is also observed for the H8 case for the tested diameters where the heat transfer profiles almost collapse into a single curve. Unfortunately, due to the unavailability of the data, the same couldn't be reported for the H10 cylinder.

A local peak is observed immediately downstream of the element for all the cases, this corresponds to the flow reattachment point and experiences relatively high heat transfer. The flow reattachment point aligns quite well for all the tested geometries, and seems to be invariant to the height and diameter of the cylinder when the stream wise dimension is scaled with height. This was something that was also observed in the laminar case. For the geometries that were reported in this investigation, the flow reattachment point remains constant with $x^* = 1.47 \pm 0.2$. For all the cases, the profile shows a downward slope towards the end of the measurement domain. This indicates that the flow begins to recover from perturbation. However, the measurement domain was not large enough to show complete recovery. This was also indicated in the Schlieren image, where the boundary layer downstream of the roughness element was thick and the measurement domain was not large enough to capture complete recovery from the perturbation.

In their investigation, [Avallone et al. \(2016b\)](#) concluded that the trend of the centreline Stanton number profile is dependent on the geometry of the roughness element. While that study focused on laminar interactions, a similar case is also observed in the current investigation. All the tested geometries here are cylindrical shaped and all of them show very similar variation in the centreline Stanton number profiles. This hints at a possibility of extension of the conclusions of [Avallone et al. \(2016b\)](#) to interactions in turbulent boundary layers as well. However, even though the trends seem to be invariant of the height or the diameter of the element, investigations at protuberance shape other than cylinders and at different flow Reynolds number has to be carried out to conclusively expect the trend of the profile to be dependent on the shape.

7.3.2 2D Heat transfer Distribution

While the centreline Stanton number profile provides a rough representation of the flow development downstream of the roughness element, a 2D heat transfer map on the model surface will provide a better understanding of the heat flux patterns around the cylinder. Figs. 7.5, 7.6 and 7.7 show the 2D heat transfer distribution around the cylinders H6, H8 and H10 respectively. In the figure, \bar{x} and \bar{y} correspond to the stream wise and span wise location scaled with the height of the cylinder, with the centre of the coordinate system located at the centre of the element for all geometries.

Directly upstream of the element, the high heat transfer region is observed. This corresponds to the recirculation region between the separation shock and the front face of the cylinder. This region is characterised by a large skin friction due to the recirculation and hence a higher than reference heat transfer is also observed. The high heat transfer region wraps around the cylinder and is seen to extend downstream, similar to what was observed in the laminar case.

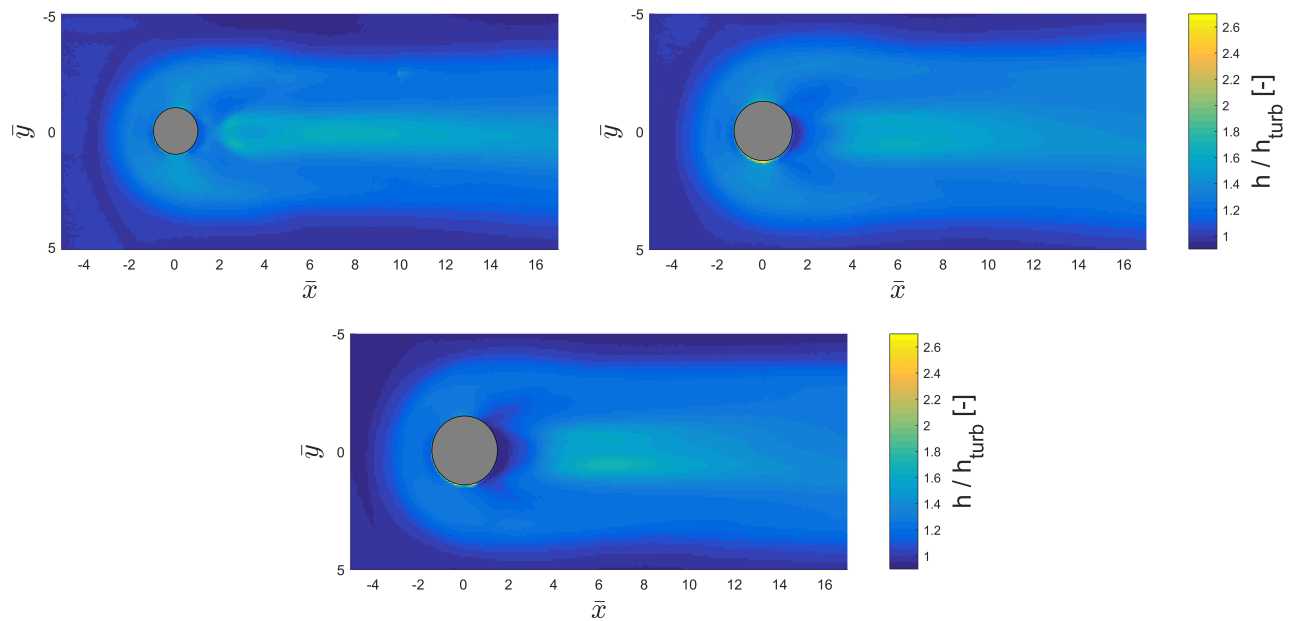


Figure 7.5: 2D Heat flux distribution around H6 cylinder for diameters D1125 (Top left) and D15 (Top right) and D17 (bottom)

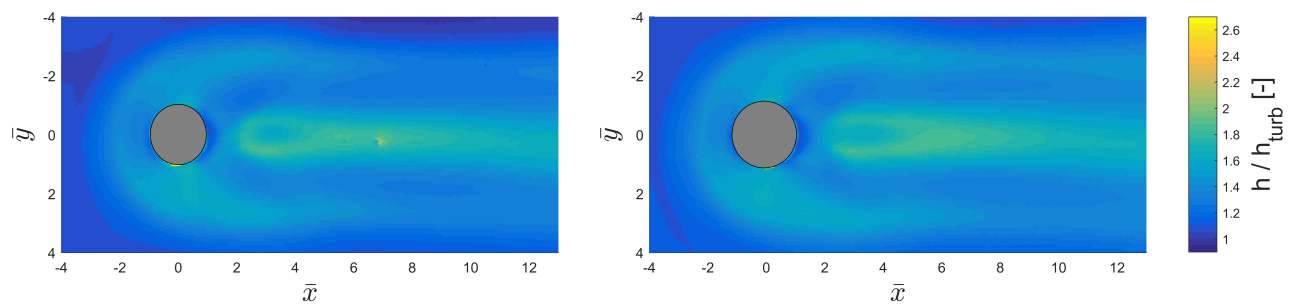


Figure 7.6: 2D Heat flux distribution around H8 cylinder for diameters D15 (left) and D17 (right)

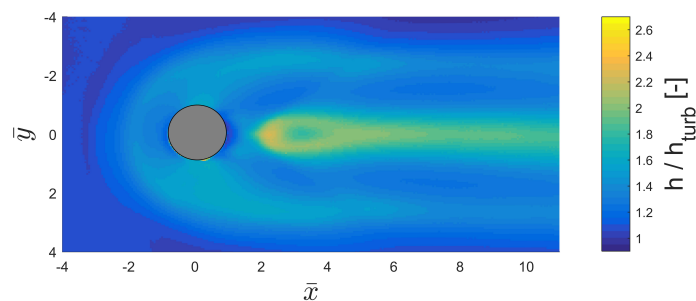


Figure 7.7: 2D heat flux distribution around H10 D17 cylinder

Downstream of the element, the centreline high heat transfer region can be clearly seen with clear dependency of the centreline maximum heat transfer on the height of the cylinder. The

wake of the cylinder is also characterised by a low and high heat transfer streaks across the span. The sustained low and high transfer streaks point to the possible existence of stream wise vortices which transfer high momentum fluid close to the wall resulting in a large heat transfer and vice versa. Thus the centreline high speed streak that was observed could be due to the presence of a central down wash from the counter rotating stream wise vortices.

Downstream of the H6 cylinder, instead of a single high heat transfer peak in the centreline, two faint high heat transfer regions are observed. This could be due to weak secondary vortices, however, a detailed investigation with additional geometries at this height has to be carried out before knowing for certain. This is however absent for the roughness elements of other two heights. where the heat transfer peaks merge to form a single central heat transfer peak. The high heat transfer in the centreline of elements of larger height tends to maintain its intensity till the end of the measurement domain, with an insubstantial drop.

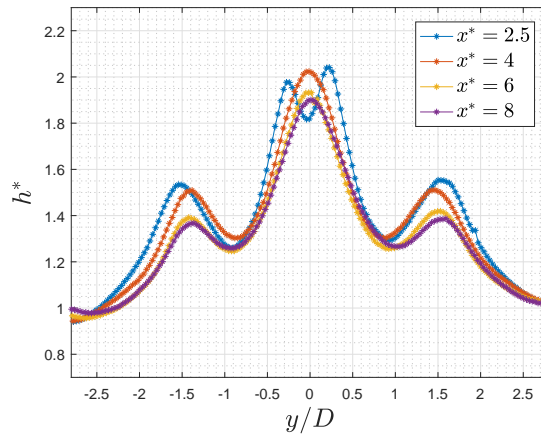


Figure 7.8: Spanwise distribution of heat flux at different stream wise location for H10 D17 cylinder

The span wise distribution of the heat transfer profiles at different stream wise locations downstream of the H10 D17 cylinder is shown in Fig.7.8. While the stream wise locations are again scaled with height based on the discussion provided earlier, the span wise coordinate (y) is scaled with the diameter of the element. Notice the twin heat transfer peaks that is visible in the near wake but disappearing in the downstream direction. Because of their location close to the near wake, the secondary vortices that are possibly causing this might also have formed upstream and wraps around the cylinder similar to the laminar case.

Two additional heat transfer peaks are observed at $y/D = \pm 1.5$, with their location largely invariant when travelling downstream. The wake observed hence does not diverge and is limited to a constant width within the measurement domain, this was the case for all the roughness elements.

To have an understanding on the effect of height of the element on the stream wise evolution of the wake a comparative study is made for D17 cylinders and is shown in Fig.7.9. In the figure, two stream wise locations are chosen, one in the near wake ($x^* = 3$) and one in the far wake ($x^* = 7.5$) and the span wise distribution of the heat transfer is shown for all the three heights.

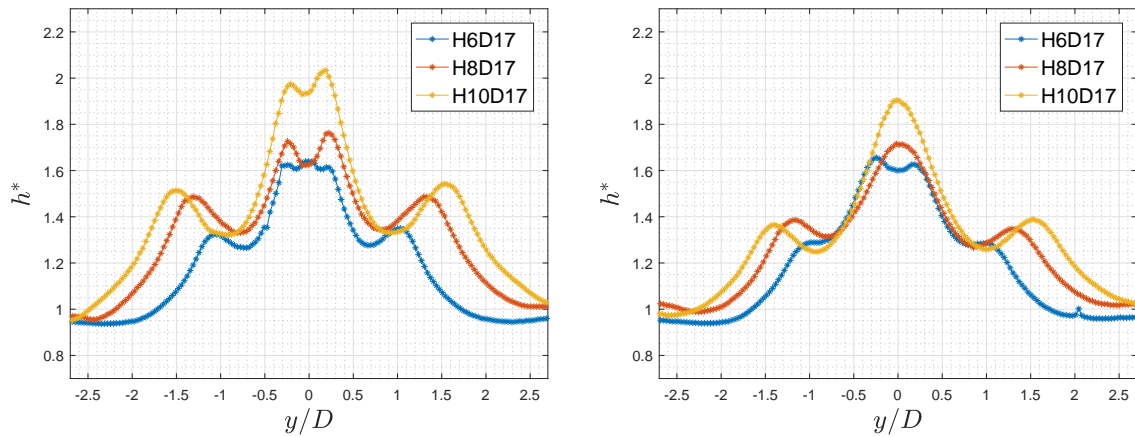


Figure 7.9: Effect of height on Span wise heat flux distribution. Plots correspond to $x^* = 3$ (left) and $x^* = 7.5$ (right)

Because of the constant wake width observed, it would be logical to expect these distribution scale with the diameter of the element. However, it was not observed to be the case. The wake tends to be larger for taller cylinders, both in the near and the far wake profiles. One possible reasoning that could explain this is that, as the height increases, it gets difficult for the flow to flow over the element and hence possible wraps around the cylinder, increasing the width of the wake. The central twin peaks are observed in the near wake profiles for all the heights and tends to disappear in the far wake only for taller cylinders while sustaining for the smallest height.

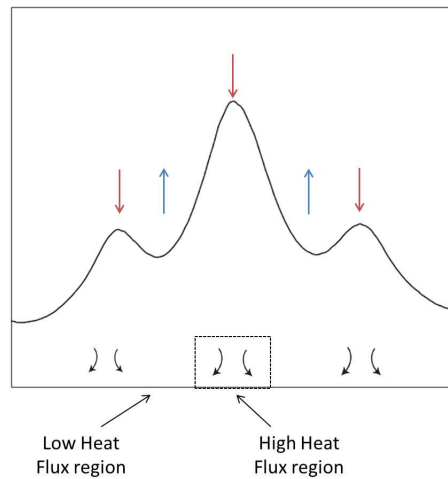


Figure 7.10: Schematics of the expected stream wise vortices in the wake. Red arrows denote the down wash and the blue arrows denote up-wash.

Since the heat transfer streaks are thought to be due to the presence of stream wise vortices in the wake, an interpretation of the possible vortex behaviour can be made. Fig.7.10 show a conceptual sketch of a typical span wise heat transfer profile along with the expected vortex rotation.

In the figure, the red arrows denote the down wash generated by the stream wise vortices while the blue arrow denote the central up wash. A counter rotating stream wise vortices with respect the centreline could hence possibly result in a central down wash and cause the observed high heat flux streaks. Same could be extended to the low and high heat flux streaks observed across the span.

7.4 Upstream Unsteadiness

The shock wave system generated upstream of the boundary layer have been reported to be extremely unsteady in literature (Clemens and Narayanaswamy, 2014). Early attempts to study this unsteadiness involved wall pressure measurements at fixed location which was mostly constrained to that location. With the recent advancements in optics and computer vision, an attempt to directly investigate the unsteadiness of the separation shock was carried out, the results of which will be presented in this section.

In the previous chapter, a detailed description of the technique followed to detect the separation shock and the upstream separation point was provided. Following the technique, the time resolved motion of the upstream separation point is shown in Fig.7.11 for the D17 cylinder corresponding to all the three heights.

A clear large scale oscillations can be visualised, confirming the unsteadiness of the separation shock. The bow shock wave on the other hand was seen to be very stable without any large scale oscillations. Attempts to capture the oscillation of the bow shock wave through the image processing routine proposed in the previous chapter resulted in spurious results, probably because of its closeness to the local boundary layer making it difficult for the routine to distinguish the gradient due to the shock. However, the relative stability of the bow shock wave was verified qualitatively from the Schlieren movie.

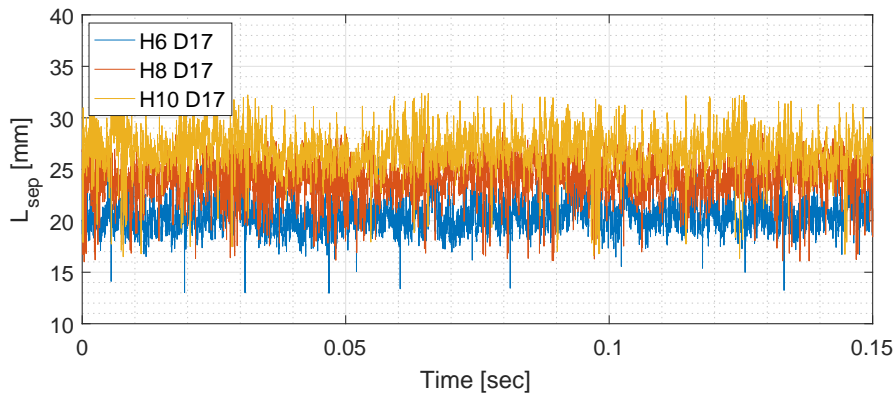


Figure 7.11: Upstream separation length for D17 cylinders

Analysing Fig.7.11, an upward shift in the upstream separation is observed, which is expected since a taller protuberance will impose a larger adverse pressure gradient, thus influencing the length of separation upstream. With this position data, a power spectral density can be constructed which could identify any dominant frequencies that may exist in the oscillations. However, no such dominant frequencies were observed (see Appendix B). A similar attempt

by Estruch-Samper et al. (2010) in a Mach 8.2 flow also resulted in the failure to isolate a dominant frequencies the reason for which could be due to the the shock oscillations being spread out in a wide range of frequencies.

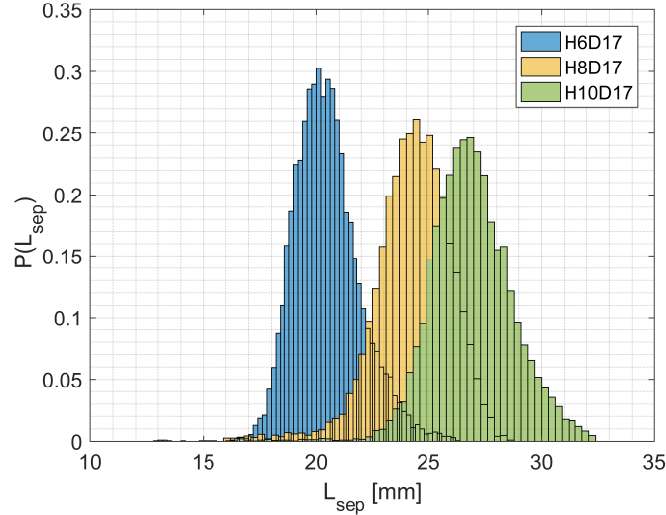


Figure 7.12: Probability density function of the upstream separation length for D17 cylinders

While a power spectral density did not yield any result, the distribution of the shock position can be studied by constructing a probability density function (PDF) of the shock oscillations. The PDF of the shock signals for the D17 cylinder is shown in Fig.7.12 where the x-axis represents the upstream separation length (L_{sep}) and the y-axis provides the probability that the shock position takes that value corresponding to the L_{sep} . A near normal distribution of the probability distribution is observed for all the three heights with the length of the upstream separation region increasing with increase in the height of the cylinder, which is consistent with what was observed from the shock position data. Previous investigation conducted by Gang et al. (2016) on a cylinder in a supersonic boundary layer indicated a normal distribution of the triple point height (h_{tp}). Since the bow shock wave is relatively stable, its possible that the separation shock and the separation point also exhibits a normal distribution.

The mean and standard deviation of the upstream separation region can be estimated from the PDF of the shock position data, With this knowledge, an investigation of the length of the upstream separation region can be conducted. With experiments performed by other independent flow visualisation and measurement techniques in addition to the Schlieren investigation, the estimates of the upstream separation length from the independently conducted experiments can be compared and verified.

Fig.7.13 shows a sample of the results from the three techniques, along the definition of the upstream separation region in each case. For the QIRT results, the upstream separation region can be considered to be the distance between the front face of the cylinder to the point where the heat transfer starts to deviate from the turbulent case along the centreline. A similar definition can be stated from for the images from the oil flow analysis where the the

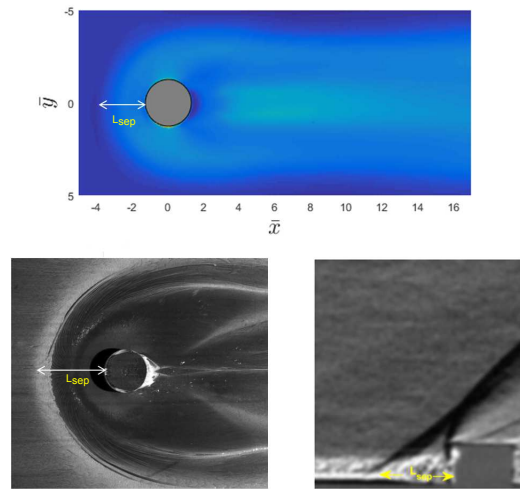


Figure 7.13: Definition of the upstream separation region in heat transfer profile (top), Oil flow visualisation (bottom left) and Schlieren (bottom right)

separation distance is the length along the centreline, between the front face of the cylinder to the upstream point of the bright separation line. For the schlieren analysis however, the PDF of the time resolved upstream separation distance is considered from which the mean and standard deviation of the shock position was estimated. The variation of the upstream separation distances for the different cylinders in this analysis is shown in Fig.7.14.

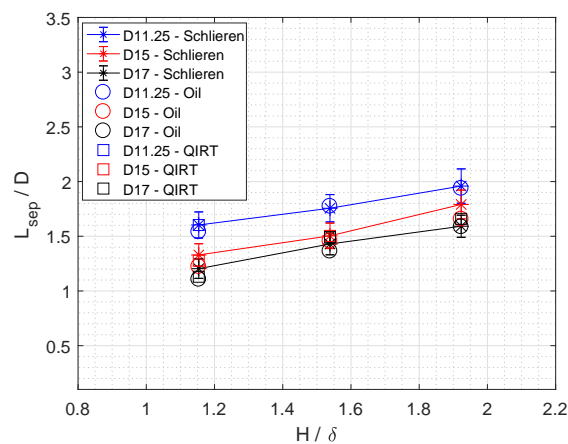


Figure 7.14: Variation of upstream separation distance

It can be seen from the plot that the upstream separation estimation from the different measurement techniques align quite well with each other, hence providing a validation of the techniques. However, there is no exact match of the data. The separation shock undergoes some curvature within the boundary layer due to the variation of Mach number and hence the true separation point might not have been estimated. In addition to this, according to [Squire \(1961\)](#), there could be a 5% ambiguity in the estimation of separation point through oil flow technique since the oil tends to accumulate not exactly at the separation point, but just upstream. Also, the low resolution of the QIRT setup might result in a $\pm 0.6mm$ error in

the exact estimation of the separation point. Yet, given that the estimated points fall within the large scale oscillations of the shock, given by the vertical bar in the Schlieren image, it can be said that the comparison data is a reasonably good match.

The increase in the upstream separation distance with the height of the cylinder is also seen. For all the heights considered here, the upstream separation distance was less than 2 cylinder diameters. Combs et al. (2016) estimated an upstream separation distance of 2.15 cylinder diameters for an asymptotic cylinder case in a turbulent boundary layer. This being a short cylinder, hence experiences lower separation, but tends towards the asymptotic case.

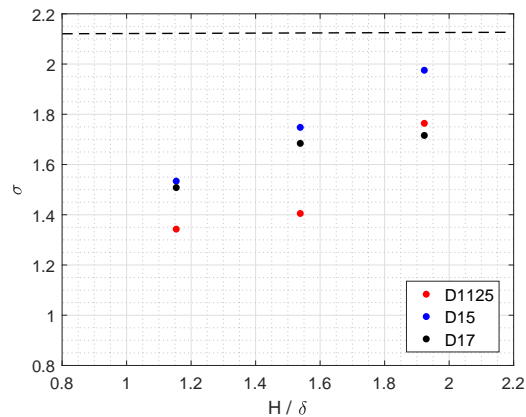


Figure 7.15: Standard deviation of the oscillating shock. Dash lines shows the asymptotic case of Lash et al. (2016)

What can also be observed from the PDF of the separation point (see Fig.7.12) is that the probability of the mean drops with increase in height of the cylinder and the function broadens, indicating that the oscillations sweeping a larger length. Thus, the standard deviation of the PDF function is a good measure to study the unsteadiness of the oscillating shock. Fig.7.15 shows the variation of the standard deviation of the separation point with the height of the cylinder. A clear increase in the standard deviation can be observed, indicating an increase in unsteadiness. For an asymptotic cylinder, Lash et al. (2016) observed a standard deviation of 0.15 cylinder diameters for a fully turbulent case. This is consistent with what was observed in this investigation, where the standard deviation when scaled with the cylinder diameters varies between 0.09 to 0.156. In general, both the mean standard deviation of the separation point increases with increase in height of the cylinder.

Part III

Conclusion

Conclusion and Recommendation

Accurate prediction of the effect of a large protuberance present in a boundary layer is essential to understand its influence on the flow topology and heat flux onto the surface of the high speed vehicle. In this Master thesis, the effect of such surface protuberances on an incoming laminar and turbulent boundary layer is investigated using Quantitative Infra red Thermography and high speed Schlieren, the results of which are summarised and concluded in the following sections.

8.1 Effect of a Surface Protuberance in an Incoming Laminar Boundary Layer

Laminar boundary layers on the surface of a body is beneficial owing to its less skin friction and heat transfer effects on the surface of the vehicle. Hence a large part of the research community has been actively involved in the flow *laminarization* to take advantage of its favourable effect. However, laminar boundary layers are affected even by a weak adverse pressure gradients and hence would affect the local aerodynamic and heat loads. Thus, in the first part of this thesis, the effect of a surface protuberances in a laminar boundary layer is investigated.

The heat transfer around cylindrical protuberances was investigated in a Mach 6.48 flow using non-intrusive Quantitative Infra-red Thermography. The cylindrical elements used as surface protuberances, were of the same heights but varied in diameter and were tested at three different unit Reynolds number. A 1D semi infinite model was used to estimate the surface heat flux through the [Cook and Felderman \(1966\)](#) technique. As a validation, the Stanton number variation of the undisturbed boundary layer in the off centre plane was estimated and compared with the theoretical expected values from the reference temperature methods and showed good agreement.

A series of high and low heat transfer streaks were observed in the wake of the elements, due to the presence of stream wise vortices with a series of high and low speed streaks, consistent

with what was observed in literature. The reattachment point along the centreline Stanton number profile scaled with the height of the cylinder showed insignificant variation with the diameter of the cylinder. On the other hand, a span wise distribution of Stanton number in the wake flow revealed that the location of primary heat transfer peak, that wraps around the cylinder, scaled with the diameter of the cylinder. However, under the same condition, the off symmetry plane peak locations showed significant deviation. The diameter of the element was seen to have an impact on the strength of the primary vortex downstream, with the magnitude of the heat flux peak caused due to the down wash from the primary vortex, increasing with diameter.

On studying the influence of flow unit Reynolds number on the span wise distribution of heat transfer profile, it was revealed that the wake is widest for the largest Reynolds number. Also, the location of the primary heat flux peak remained invariant with the Reynolds number and was dependent only on the diameter of the element. These results provides evidence for the dependency of the strength and location of the primary vortex pair on the diameter of the element.

Moving downstream, the strength of the heat transfer streaks fell with increase in the stream wise direction. This is due to the break down and lift up of the primary vortex pair as observed by previous researchers. The heat flux amplitude plot also revealed the dependency of the peak heating on the diameter of the element, with the amplitude of larger magnitudes exhibited by elements of larger diameters. The presence of a turbulent wedge was chosen to be means to identify the onset of transition point in this investigation. Observing the 2D Stanton number distribution, a turbulent wedge was observed for elements at the highest Reynolds number, while the wake width stayed nearly constant at lower Reynolds number. Since the height of all the elements are the same, this result adds to the conclusions from literature, where the transition location was expected to move upstream with increase in roughness height based Reynolds number.

A system of span wise vortices upstream of the element were also detected indirectly through the heat transfer peaks, whose number were consistent with that of Baker (1979). They tend to wrap around the cylinder and travel downstream causing low and high heat flux regions. The length of the upstream separation length was estimated from the heat transfer distribution in the centreline. While the literature focused mainly on the influence of the height of the element on the upstream separation length, the dependency of the diameter was also shown. An empirical correlation, adopted from Hung and Clauss (1980) and modified, was shown to have good agreement with the current estimates, along with the estimates from recent literature. The length of the upstream separation region is important parameter which influences the heating upstream of the protuberance. Hence this correlation highlights the importance of the diameter of the protuberance in estimating the length of separation upstream, contrast to the study carried out in recent literatures, where the effect of the height was only considered.

8.2 Effect of a Surface Protuberance in an Incoming Turbulent Boundary Layer

While the interaction of the cylinder with the laminar boundary layer is interesting and relevant to investigate, most boundary layer on high speed aircraft are turbulent in nature. Hence a separate part of this thesis project also focused on investigating the interactions of a surface protuberance with an incoming turbulent boundary layer.

The investigations were carried out in a Mach 2 environment, with QIRT being the primary investigative tool, assisted by Oil flow and Schlieren measurements. Since the height of the boundary layer stays constant in this flow facility, the effect of changing H/δ was achieved by designing protuberances of various heights (H), each at different diameters (D). An in-house designed heated printed circuit board was used, onto which the protuberances are attached using an high temperature resistant double sided adhesive tape. From the temperature measurements taken at the steady state condition, the convective transfer coefficient was evaluated. In order to mitigate the effects of non-uniform heating of the PCB plate due to varying copper thickness, a non-uniform heating correction was applied. The resulting heat transfer estimates on the undisturbed boundary layer showed good agreement with literature, validating the experimental procedure.

A separation and a bow shock wake was observed upstream of the element along with a strong recirculation region. Oil flow images also shows the existence of an horse shoe vortex upstream of the cylinder, wrapping around and travelling downstream. A peak heating was observed along the centreline in the near wake that corresponds to the reattachment point and similar to the laminar case, they scaled with the height of the cylinder. The centreline heat transfer profile also showed heating of 1.5 - 2 times the local turbulent case, indicating the importance of studying the wake behind a protuberance, in addition to the upstream region.

The 2D heat transfer distribution confirmed the presence of the centreline high heat transfer regions in the wake of the protuberance with the peak heating in the centreline also increasing with increase in height of the element. In addition to that, a series of high and low heat transfer streaks are observed indicating the possible existence of stream wise vortex structures that transport high momentum fluid close to the wall and vice versa. The width of the wake also remained constant for all cases until the end of measurement domain. A plot of the span wise distribution of heat transfer profiles at different stream wise locations indicated the existence of local peaks near the centreline and close to the protuberance, which could be due to secondary vortices in the near wake. The effect of height of the protuberance on the element was investigated by studying the span wise distribution of heat transfer profiles of elements of three different heights at two location in the stream wise direction. While the near wake profiles showed the existence of local peaks for all the three elements, it disappeared in the far wake profiles for taller elements. An interesting observation was the increase in the wake width of the element with the height, even at a constant diameter and flow Reynolds number. This could be because of the difficulty of the flow to go over taller protuberances and hence wraps around the cylinder and exhibiting wider footprint.

The upstream unsteady region was investigated using high speed time resolved Schlieren imaging where digital image processing and computer vision techniques were utilised to extract the shock structures. A linear regression was then applied to determine the time resolved upstream separation length for all the protuberance geometries. A probability density function was constructed which revealed a normal distribution of the location of the separation point. The resulting standard deviation was observed to be dependent on the height thus providing evidence that the upstream unsteadiness increases with the height of the cylinder. The statistical mean separation length obtained from the Schlieren analysis also showed good agreement with the measurements taken from the oil flow and Infrared thermography images. In general, it was observed that the both the mean and the standard deviation of the upstream separation length increase with increase in height of the cylinder.

8.3 Scope for Future work

Though the results of Infrared Thermography provided a 2D map of the temperature and heat transfer profiles, in order to increase accuracy, a separate investigation of the upstream separation region with a higher resolution could be conducted to make sure that the true high heat flux peak and its location is measured. This can also be extended to the wake measurements where multiple high resolution frames can be stitched together to make sure that the resulting image is both of high resolution and covers a larger section of the wake. Also, protuberances of different geometries could be tested to compare the upstream separation length with the correlation discussed in the first part of the thesis (Section 5.5) to understand its limitations and also to improve the statistical convergence.

In the second part of the thesis, an investigation on to the effect of surface protuberances on an incoming turbulent boundary layer was carried out. The presence of high and low heat transfer streaks indicates the possible existence of stream wise vortices. Particle Image Velocimetry can be carried out to understand the wake behaviour and to directly identify the existence of stream wise vortices that were hypothesised in this thesis. While this investigation was limited to cylindrical protuberances, additional QIRT measurement on geometries of different shapes (hemishpere, diamond etc.) can be carried out to understand the effect of shape on the heat transfer profiles.

While a time resolved Schlieren analysis was carried out in the turbulent case, due to time restrictions, this couldn't be extended to the laminar case. [Wheaton and Schneider \(2012\)](#) observed an instability of $21kHz$ in the wake of a cylinder in a Mach 6 flow. Further computational analysis provided a possible origin of this instability upstream of the roughness element. A similar time resolved Schlieren analysis can thus be carried out in the HTFD to try to provide an experimental confirmation of the same and also to identify a possible scaling based on geometrical and flow parameters.

Bibliography

- Y. I. Abdel-Aziz and H. M. Karara. Direct Linear Transformation from Comparator Coordinates into Object Space Coordinates in Close-Range Photogrammetry. In *Proceedings of the Symposium on Close-Range Photogrammetry*, pages 1 – 18, Urbana, Illinois, Jan 1971.
- J. D. Anderson Jr. *Fundamentals of Aerodynamics*. McGraw-Hill Education, fifth edition edition, 2010.
- J. D. Anderson Jr. *Hypersonic and High-Temperature Gas Dynamics*. AIAA Education Series. American Institute of Aeronautics and Astronautics, Inc, second edition edition, 2006.
- T. Arts and C. Camci. Short Duration Heat Transfer Measurements. von Karman Institute for Fluid Mechanics, 1985.
- T. Astarita and G. Cardone. Thermofluidynamic analysis of the flow in a sharp 180° turn channel. *Experimental Thermal and Fluid Science*, 20(3-4):188–200, Feb 2000.
- T. Astarita and G. M. Carlomagno. *Infrared Thermography for Thermo-Fluid-Dynamics*. Experimental Fluid Mechanics. Springer-Verlag Berlin Heidelberg, 2013. ISBN 978-3-642-29508-9.
- F. Avallone. *Application of non-intrusive experimental techniques to roughness-induced transition in hypersonic flows (PhD)*. Phd thesis, University of Naples Federico II, 2015.
- F. Avallone, Q. Ye, F. F. J. Schrijer, F. Scarano, and G. Cardone. Tomographic piv investigation of roughness-induced transition in a hypersonic boundary layer. *Experiments in Fluids*, 55(11), 2014.
- F. Avallone, C. S. Greco, F. F. J. Schrijer, and G. Cardone. A low-computational-cost inverse heat transfer technique for convective heat transfer measurements in hypersonic flows. *Experiments in Fluids*, 56(4), 2015.
- F. Avallone, D. Ragni, F.F.J. Schrijer, F. Scarano, and G. Cardone. Study of a supercritical roughness element in a hypersonic laminar boundary layer. *AIAA Journal*, 54(6):1892–1900, 2016a.
- F. Avallone, F. F. J. Schrijer, and G. Cardone. Infrared thermography of transition due to isolated roughness elements in hypersonic flows. *Physics of Fluids*, 28(2):024106, 2016b.

- C. J. Baker. The laminar horseshoe vortex. *Journal of Fluid Mechanics*, 95(02):347, 1979.
- S. A. Berry, S. A. Bouslog, G. J. Brauckmann, and J. M. Caram. Shuttle Orbiter Experimental Boundary-Layer Transition Results with Isolated Roughness. *Journal of Spacecraft and Rockets*, 35(3):241–248, May 1998.
- S. A. Berry, A. H. Auslender, A. D. Dilley, and J. F. Calleja. Hypersonic Boundary-Layer Trip Development for Hyper-X. *Journal of Spacecraft and Rockets*, 38(6):853–864, 2001.
- S. M. Bogdonoff. Some Experimental studies of the separation of supersonic turbulent boundary layers. Technical report, Princeton University, 1955.
- G. M. Carlomagno and G. Cardone. Infrared thermography for convective heat transfer measurements. *Experiments in Fluids*, 49(6):1187–1218, 2010.
- G. M. Carlomagno, L. de Luca, G. Cardone, and T. Astarita. Heat flux sensors for infrared thermography in convective heat transfer. *Sensors (Basel)*, 14(11):21065–116, 2014.
- L. Chen, C. W. Armstrong, and D. D. Raftopoulos. An investigation on the accuracy of three-dimensional space reconstruction using the direct linear transformation technique. *Journal of Biomechanics*, 27(4):493–500, 1994.
- M. Choudhari, F. Li, and J. Edwards. Stability Analysis of Roughness Array Wake in a High-Speed Boundary Layer. In *47th AIAA Aerospace Sciences Meeting, Orlando*. American Institute of Aeronautics and Astronautics, Jan 2009.
- M. Choudhari, F. Li, C. Chang, J. Edwards, M. Kegerise, and R. King. Laminar-Turbulent Transition behind Discrete Roughness Elements in a High-Speed Boundary Layer. In *48th AIAA Aerospace Sciences Meeting Including the New Horizons Forum and Aerospace Exposition*. American Institute of Aeronautics and Astronautics, Jan 2010.
- N.T. Clemens and V. Narayanaswamy. Low-Frequency Unsteadiness of Shock Wave/Turbulent Boundary Layer Interactions. *Annual Review of Fluid Mechanics*, 46(1):469–492, 2014.
- C. S. Combs, E. L. Lash, , and J. D. Schmisser. Investigation of a Cylinder-Induced Transitional Shock Wave-Boundary Layer Interaction using Laser Diagnostics. In *32nd AIAA Aerodynamic Measurement Technology and Ground Testing Conference*. American Institute of Aeronautics and Astronautics, Inc, 2016.
- W. J. Cook and E. J. Felderman. Reduction of data from thin-film heat-transfer gages - a concise numerical technique. *AIAA Journal*, 4(3):561–562, 1966. ISSN 0001-1452 1533-385X. doi: 10.2514/3.3486.
- L. M. Couch. Flow-field measurements downstream of two protuberances on a flat plate submerged in a turbulent boundary layer at mach 2.49 and mach 4.44. Technical report, NASA Langley Research Center, 1969.
- P. Danehy, B. Bathel, C. Ivey, J. Inman, and S. Jones. No plif study of hypersonic transition over a discrete hemispherical roughness element. In *47th AIAA Aerospace Sciences Meeting*. AIAA, 2009.

- D. S. Dolling and S. M. Bogdonoff. Scaling of interactions of cylinders with supersonic turbulent boundary layers. *AIAA Journal*, 19(5):655–657, May 1981.
- W.M. Doyle. The Development of Hiduminium-RR.58 Aluminium Alloy. *Aircraft Engineering and Aerospace Technology*, 41(11):11–14, Nov 1969.
- E.R.G Eckert. Engineering relations for heat transfer and friction in high-velocity laminar and turbulent boundary-layer flow over surfaces with constant pressure and temperature. *Transactions of the Americal Socociety of Mechanical Engineers*, 78(6):1273–1283, 1956.
- D. Estruch-Samper. Reattachment heating upstream of short compression ramps in hypersonic flow. *Experiments in Fluids*, 57(5), 2016.
- D. Estruch-Samper, N. J. Lawson, D. G. MacManus, K. P. Garry, and J. L. Stollery. Measurement of shock wave unsteadiness using a high-speed schlieren system and digital image processing. *Rev Sci Instrum*, 79(12):126108, 2008.
- D. Estruch-Samper, D. G. MacManus, J. L. Stollery, N. J. Lawson, and K. P. Garry. Hypersonic interference heating in the vicinity of surface protuberances. *Experiments in Fluids*, 49(3):683–699, 2010.
- Tyler T. Evans and Alexander J. Smits. Measurements of the mean heat transfer in a shock wave-turbulent boundary layer interaction. *Experimental Thermal and Fluid Science*, 12(1):87–97, 1996.
- M. C. Fischer. Spreading of a turbulent disturbance. *AIAA Journal*, 10(7):957–959, 1972.
- J. H. M. Fransson, L. Brandt, A. Talamelli, and C. Cossu. Experimental and theoretical investigation of the nonmodal growth of steady streaks in a flat plate boundary layer. *Physics of Fluids*, 16(10):3627–3638, Oct 2004.
- M. Gad-El-Hak, R.F. Blackwelderf, and J.J. Riley. On the growth of turbulent regions in laminar boundary layers. *Journal of Fluid Mechanics*, 110:7395, 1981.
- D. Gang, S. Yi, and L. He. Characteristics of the cylinder-induced shock wave and turbulent boundary layer interactions. *Journal of Visualization*, 19(4):581–585, 2016.
- H. A. Gebbie, W. R. Harding, C. Hilsum, A. W. Pryce, and V. Roberts. Atmospheric transmission in the 1 to 14 μm region. *Proceedings of the Royal Society A: Mathematical, Physical and Engineering Sciences*, 206(1084):87–107, 1951.
- R. H. M. Giepman, F. F. J. Schrijer, and B. W. van Oudheusden. Flow control of an oblique shock wave reflection with micro-ramp vortex generators: Effects of location and size. *Physics of Fluids*, 26(6):066101, Jun 2014.
- A. Goktepe and E. Kocaman. Analysis of camera calibrations using direct linear transformation and bundle adjustment methods. *Sci. Res. Essays*, 5(9):869–872, 2010.
- R.C. Gonzalez, R.E. Woods, and S.L. Eddins. *Digital Image Processing Using MATLAB*. Pearson Education, 2 edition, 2009. ISBN 9788177588989.

- R.M. Hicks and W. R. Harper. A comparison of spherical and triangular boundary-layer trips on a flat plate at supersonic speeds. Technical Report NASA-TM-X-2146, NASA Ames Research Centre, 1970.
- T. J. Horvath, D. M. Tomek, K. T. Berger, S. C. Splinter, J. N. Zalameda, Paul W. Krasa, S. Tack, R. J. Schwartz, D. M. Gibson, and A. Tietjen. The HYTHIRM Project: Flight Thermography of the Space Shuttle During Hypersonic Re-entry. In *48th AIAA Aerospace Science Meeting Conference*. American Institute of Aeronautics and Astronautics, Inc, 2010.
- F. Hung and J. Clauss. Three-dimensional protuberance interference heating in high speed flow. In *AIAA 18th Aerospace Sciences Meeting*. AIAA, Jan 1980.
- F. Hung and D. Patel. Protuberance interference heating in high-speed flow. In *AIAA 19th Thermophysics Conference*. AIAA, June 1984.
- P. S. Iyer and K. Mahesh. High-speed boundary-layer transition induced by a discrete roughness element. *Journal of Fluid Mechanics*, 729:524–562, 2013.
- A. L. Kistler. Fluctuating Wall Pressure under a Separated Supersonic Flow. *The Journal of the Acoustical Society of America*, 36(3):543–550, Mar 1964.
- P S Klebanoff, G B Schubauer, and K D Tidstrom. Measurements of the effect of the two-dimensional and three-dimensional roughness elements on boundary layer transition. *Journal of Aeronautical Sciences*, 22(11):803–804, Jun 1955.
- R. Krechetnikov and I. I. Lipatov. On upstream influence in supersonic flows. *Journal of Fluid Mechanics*, 539:167, Sep 2005.
- F. Kreith and R.M. Manglik. *Principles of Heat Transfer*. Cengage Learning, 8th edition, 2016. ISBN 9781337516921.
- C. S. Kumar and K. P. J. Reddy. Hypersonic interference heating on flat plate with short three-dimensional protuberances. *AIAA Journal*, 52(4):747–756, 2014.
- C. S. Kumar, T. Singh, and K. P. J. Reddy. Investigation of the separated region ahead of three-dimensional protuberances on plates and cones in hypersonic flows with laminar boundary layers. *Physics of Fluids*, 26(12):126101, 2014.
- E. L. Lash, C. S. Combs, P. A. Kreth, E. A. Beckman, and J. D. Schmisser. Developing an image-based analysis of the dynamics of transitional shock wave-boundary layer interactions. In *32nd AIAA Aerodynamic Measurement Technology and Ground Testing Conference*. American Institute of Aeronautics and Astronautics, Inc, 2016.
- A. S. Lau. The narcissus effect in infrared optical scanning systems. 107:57–62, 12 1976.
- P. Levesque, P. Brmond, J. L. Lasserre, A. Paupert, and D. L. Balageas. Performance of fpa ir cameras and their improvement by time, space and frequency data processing. *Quantitative InfraRed Thermography Journal*, 2(1):97–112, 2005.
- M. J. Lighthill. On Boundary Layers and Upstream Influence. I. A Comparison between Subsonic and Supersonic Flows. *Proceedings of the Royal Society A: Mathematical, Physical and Engineering Sciences*, 217(1130):344–357, May 1953.

- H Ludwig. "Der Rohrwindkanal, Zeitschrift für Flugwissenschaften. 3:206–216, 1955.
- O. Marxen, G. Iaccarino, and E.S.G. Shaqfeh. Disturbance evolution in a Mach 4.8 boundary layer with two-dimensional roughness-induced separation and shock. *Journal of Fluid Mechanics*, 648:435469, 2010.
- D. Masutti. *Ground Testing Investigation of Hypersonic Transition Phenomena for a Re-Entry Vehicle*. Phd thesis, Delft University of Technology, 2013.
- MathWorks. *MATLAM Optimisation Toolbox*, 2016.
- R. Mayer. Orientation on quantitative IR-thermography in wall shear stress measurements. Report LR-812, Delft University of Technology, 1996.
- D. J. Mee, H. S. Chiu, and P. T. Ireland. Techniques for detailed heat transfer measurements in cold supersonic blowdown tunnels using thermochromic liquid crystals. *International Journal of Heat and Mass Transfer*, 45(16):3287–3297, 2002.
- R. J. Moffat. Describing the uncertainties in experimental results. *Experimental Thermal and Fluid Science*, 1(1):3–17, 1988.
- M. V. Morkovin. Bypass transition to turbulence and research Desiderata. In *NASA. Lewis Research Center Transition in Turbines*, number (Document ID: 19850023120), Jul 1985.
- M. V. Morkovin. Critical Evaluation of Transition from Laminar to Turbulent Shear Layers with Emphasis on Hypersonically Traveling Bodies. Technical Report AFFDL-TR-68-149, Air Force Flight Dynamics Laboratory, Wright Patterson Air Force Base, Dayton, Ohio, 1969.
- A. E. Mudau, C. J. Willers, D. Griffith, and F. P. J. le Roux. *Non-uniformity correction and bad pixel replacement on LWIR and MWIR images*. IEEE, Apr 2011.
- T. Orzanowski. Nonuniformity correction algorithm with efficient pixel offset estimation for infrared focal plane arrays. *Springerplus*, 5(1):1831, 2016.
- Daniel C. Reda. Review and Synthesis of Roughness-Dominated Transition Correlations for Reentry Applications. *Journal of Spacecraft and Rockets*, 39(2):161–167, Mar 2002.
- E. Reshotko. Transient growth: A factor in bypass transition. *Physics of Fluids*, 13(5):1067–1075, May 2001.
- E. Reshotko. Transition Issues for Atmospheric Entry. *Journal of Spacecraft and Rockets*, 45(2):161–164, Mar 2008.
- E. Reshotko and A. Tumin. Role of Transient Growth in Roughness-Induced Transition. *AIAA Journal*, 42(4):766–770, apr 2004.
- E. Schmidt and E. Eckert. Über die richtungsverteilung der wärmestrahlung von oberflächen. *Forschung auf dem Gebiet des Ingenieurwesens A*, Jul 1935.
- S. P. Schneider. Summary of Hypersonic Boundary-Layer Transition Experiments on Blunt Bodies with Roughness. *Journal of Spacecraft and Rockets*, 45(6):1090–1105, 2008a.

- S. P. Schneider. Effects of Roughness on Hypersonic Boundary-Layer Transition. *Journal of Spacecraft and Rockets*, 45(2):193–209, 2008b.
- F. F. J. Schrijer and W. J. Bannink. Description and Flow Assessment of the Delft Hypersonic Ludwig Tube. *Journal of Spacecraft and Rockets*, 47(1):125–133, 2010.
- F.F.J. Schrijer. *Experimental investigation of re-entry aerodynamic phenomena - Development of non-intrusive Flow diagnostics in a Ludwig tube*. Phd thesis, Delft University of Technology, 2010.
- D. L. Schultz and T.V. Jones. Heat-transfer measurements in short-duration hypersonic facilities. AGARDograph AGARD-AG-165, University of Oxford, 1973.
- R. Sedney and C. W. Kitchens. Separation ahead of Protuberances in Supersonic Turbulent Boundary Layers. *AIAA Journal*, 15(4):546–552, apr 1977.
- G. S. Settles. *Schlieren and Shadowgraph Techniques*. Experimental Fluid Mechanics. Springer Berlin Heidelberg, 2001.
- N. S. Sharp. *Hypersonic Measurements of Roughness-Induced Transient Growth*. Phd thesis, Texas A & M University, 2014.
- N. S. Sharp and E. B. White. Roughness-Induced Transient Growth on a Hypersonic Blunt Cone. In *52nd Aerospace Sciences Meeting*. American Institute of Aeronautics and Astronautics, Jan 2014.
- L. C. Squire. The motion of a thin oil sheet under the steady boundary layer on a body. *Journal of Fluid Mechanics*, 11(2):161179, 1961.
- P.K. Subbareddy, M.D. Bartkowicz, and G.V. Candler. Direct numerical simulation of high-speed transition due to an isolated roughness element. *Journal of Fluid Mechanics*, 748: 848–878, 2014.
- Z. Sun. *Micro Ramps in Supersonic Turbulent Boundary Layers*. Phd thesis, Delft University of Technology, 2014.
- Z. Sun, F. F. J. Schrijer, F. Scarano, and B. W. van Oudheusden. The three-dimensional flow organization past a micro-ramp in a supersonic boundary layer. *Physics of Fluids*, 24(5): 055105, 2012.
- S. S Tambe, F. F. J. Schrijer, and B. W. van Oudheusden. Effect of geometry on the downstream flow topology of a micro ramp in a supersonic turbulent boundary layer: an experimental study. In *7th European Conference for Aeronautics and Space Sciences(EUCASS)*, Jul 2017.
- P. Tartabini, D. Bose, M. Thornblom, J. Lien, and J. Martin. Mach 10 Stage Separation Analysis for the X43-A. In *44th AIAA Aerospace Sciences Meeting and Exhibit*. American Institute of Aeronautics and Astronautics, Jan 2006.
- S. C. Tirtrey, O. Chazot, and L. Walpot. Characterization of hypersonic roughness-induced boundary-layer transition. *Experiments in Fluids*, 50(2):407–418, 2011.

- E. R. van Driest. Turbulent boundary layer in compressible fluids. *Journal of the Aeronautical Sciences*, 18(3):145–160, 1951.
- E. R. van Driest and W. D. McCauley. The Effect of Controlled Three-Dimensional Roughness on Boundary-Layer Transition at Supersonic Speeds. *Journal of the Aerospace Sciences*, 27(4):261–271, Apr 1960.
- E. R. van Driest, C. B. Blumer, and C. S. Wells. Boundary-layer transition on blunt bodies - effect of roughness. *AIAA Journal*, 5(10):1913–1915, oct 1967.
- N. Voogt. Investigation on upersonic, large wall roughness elements using QIRT and PIV. MSc Thesis, Delft University of Technology, 2017.
- D. Greg Walker and Elaine P. Scott. Evaluation of estimation methods for high unsteady heat fluxes from surface measurements. *Journal of Thermophysics and Heat Transfer*, 12(4):543–551, 1998.
- J. C. Westkaemper. Turbulent boundary-layer separation ahead of cylinders. *AIAA Journal*, 6(7):1352–1355, jul 1968.
- B.M. Wheaton and S.P. Schneider. Roughness-Induced Instability in a Hypersonic Laminar Boundary Layer. *AIAA Journal*, 50(6):1245–1256, 2012. ISSN 0001-1452 1533-385X.
- E. B. White, J. M. Rice, and F. Ergin. Receptivity of stationary transient disturbances to surface roughness. *Physics of Fluids*, 17(6):064109, Jun 2005.
- F. M. White. *Viscous Fluid Flow*. McGraw-Hill series in mechanical engineering. McGraw-Hill, 1991.
- A. H. Whithead. Flowfield and drag characteristic of several boundary layer tripping elements in hypersonic flow. Technical Report NASA TN-D-5454, Langley Research Centre, 1969.
- T. Wolf, M. Estorf, and R. Radespiel. Investigation of the starting process in a Ludwieg tube. *Theoretical and Computational Fluid Dynamics*, 21(2):81–98, Feb 2007.
- M. R. Wool. Final summary report: Passive Nosetip Technology (PANT). Technical Report TR-75-250, Aerotherm Division/Acurex Corporation, California, 1975.
- Q. Ye, F.F.J. Schrijer, and F. Scarano. Infrared thermography investigation of transitional flow over isolated roughness at high speeds. In *51st 3AF International Conference on Applied Aerodynamics*, Apr 2016.
- Q. Ye, F.F.J. Schrijer, and F. Scarano. Tomographic PIV Measurement of Hypersonic Boundary Layer Transition Past a Micro-ramp. In *AIAA AVIATION Forum 47th AIAA Fluid Dynamics Conference*. American Institute of Aeronautics and Astronautics, Inc., 2017.
- M. S. Yu, J. Song, J. C. Bae, and H. H. Cho. Heat transfer by shock-wave/boundary layer interaction on a flat surface with a mounted cylinder. *International Journal of Heat and Mass Transfer*, 55(5-6):1764–1772, 2012.

Appendix A

Reference Temperature Method

The Reference Temperature Method is an approximate engineering method for estimating the skin friction and heat transfer for both compressible laminar and turbulent boundary layers. This method involves the usage of expressions of skin friction from the incompressible flow theory, where the thermodynamic and transport properties are evaluated at a certain reference temperature, such that the classical expressions are "corrected" for the compressibility effect (Anderson Jr, 2006). In this section, the application of the reference temperature method used to estimate the flat plate laminar and turbulent Stanton number distribution is discussed.

For an incompressible laminar flow over a flat plate, the local skin friction coefficient for a laminar and turbulent boundary layer is given by (White, 1991):

$$c_{f_i, lam} = \frac{0.664}{\sqrt{Re_x}} \quad (A.1)$$

$$c_{f_i, turb} = \frac{0.0592}{\sqrt[5]{Re_x}} \quad (A.2)$$

where, Re_x is the Reynolds number based on the position on the flat plate. Now, according to the reference temperature method, this expression can be used to estimate the compressible counterparts, when the quantities are calculated at a certain reference temperature. If $*$ denote the quantities evaluated at the reference temperature, then:

$$c_{f_{lam}}^* = \frac{0.664}{\sqrt{Re_x^*}} \quad (A.3)$$

$$c_{f_{turb}}^* = \frac{0.0592}{\sqrt[5]{Re_x^*}} \quad (A.4)$$

with the quantities, $c_{f_{lam}}^*$, $c_{f_{turb}}^*$ and Re_x^* evaluated at a certain reference temperature T^* . The local skin friction coefficient for the laminar boundary and turbulent boundary layers

can be written as:

$$c_f^* = \frac{\tau_w}{\frac{1}{2}\rho^*u_e^2} \quad (\text{A.5})$$

where, τ_w is the corresponding wall shear stress for the laminar or turbulent boundary layers. Making use of this equation, the skin friction coefficient can be given in terms of known quantities through the following steps:

$$\begin{aligned} c_{f_{lam}}^* &= \frac{0.664}{\sqrt{Re_x^*}} & c_{f_{turb}}^* &= \frac{0.0592}{\sqrt[5]{Re_x^*}} \\ \frac{\tau_{w_{lam}}}{\frac{1}{2}\rho^*u_e^2} &= \frac{0.664}{\sqrt{Re_x^*}} & \frac{\tau_{w_{turb}}}{\frac{1}{2}\rho^*u_e^2} &= \frac{0.0592}{\sqrt[5]{Re_x^*}} \\ \frac{\tau_{w_{lam}}}{\frac{1}{2}\rho_e u_e^2} &= \frac{\rho^*}{\rho_e} \frac{0.664}{\sqrt{Re_x^*}} & \frac{\tau_{w_{turb}}}{\frac{1}{2}\rho_e u_e^2} &= \frac{\rho^*}{\rho_e} \frac{0.0592}{\sqrt[5]{Re_x^*}} \\ c_{f_{c,lam}} &= \frac{\rho^*}{\rho_e} \frac{0.664}{\sqrt{Re_x^*}} & c_{f_{c,turb}} &= \frac{\rho^*}{\rho_e} \frac{0.0592}{\sqrt[5]{Re_x^*}} \end{aligned} \quad (\text{A.6})$$

The parameter Re_x^* can also be re-written as follows:

$$Re_x^* = \frac{\rho^* u_e x}{\mu^*} = \frac{\rho^* \mu_e}{\rho_e \mu^*} Re_x \quad (\text{A.7})$$

Eqns.A.6and A.7 can be combined to give the skin friction coefficient for compressible laminar and turbulent boundary layers as:

$$c_{f_{c,lam}} = \left(\frac{\rho^* \mu^*}{\rho_e \mu_e} \right)^{1/2} \frac{0.664}{\sqrt{Re_x}} \quad (\text{A.8})$$

$$c_{f_{c,turb}} = \left(\frac{\rho^*}{\rho_e} \right)^{4/5} \left(\frac{\mu^*}{\mu_e} \right)^{1/5} \frac{0.0592}{\sqrt[5]{Re_x}} \quad (\text{A.9})$$

The reference parameters ρ^* and μ^* are evaluated at a certain reference temperature T^* , given the gas law and Sutherland's law respectively as:

$$\rho^* = \frac{p_e}{RT^*} \quad (\text{A.10})$$

$$\mu^* = \mu_0 \left(\frac{T^*}{T_0} \right)^{3/2} \left(\frac{T_0 + S}{T^* + S} \right)$$

where μ_0 is the viscosity evaluated at the temperature T_0 , S is the Sutherland's constant and R is the specific gas constant. A number of empirical correlation are available in literature to estimate T^* , which is a function of the boundary layer edge Mach number (M_e) and the flat

plate wall temperature (T_w). In this thesis, the following expression were used, respectively for laminar and turbulent case:

$$\left(\frac{T^*}{T_w}\right)_{lam} = 1 + 0.032M_e^2 + 0.58\left(\frac{T_w}{T_e} - 1\right)$$

$$\left(\frac{T^*}{T_w}\right)_{turb} = 1 + 0.035M_e^2 + 0.45\left(\frac{T_w}{T_e} - 1\right)$$

Finally, the estimated skin friction coefficient can be used to compute the Stanton number using the modified Reynolds analogy, given by the expression:

$$St = \frac{c_f}{2} Pr^{-2/3} \quad (\text{A.11})$$

where, Pr is the Prandtl number. Note that, the Stanton number estimated here is normalised with respect to the adiabatic wall temperature (T_{aw}). However the heat flux from the HTFD is normalised with respect to the total temperature of the free stream. Hence care has to be taken to properly account for this such that the modified Stanton number (C_h) is used for the comparative studies.

Appendix B

Spectral Analysis

In Section 6.5.1 the technique to extract the shock location from the Schlieren image was discussed. A linear fit of the separation shock position and evaluated at the wall for all the frames would result in the time resolved upstream separation length. A power spectral density (PSD) using the Welch's method can be computed for the resulting $x - t$ curve to determine which frequencies exhibit the largest magnitude. The result of the PSD for the upstream separation distance corresponding to the H10 D17 curve is shown in Fig.B.1.

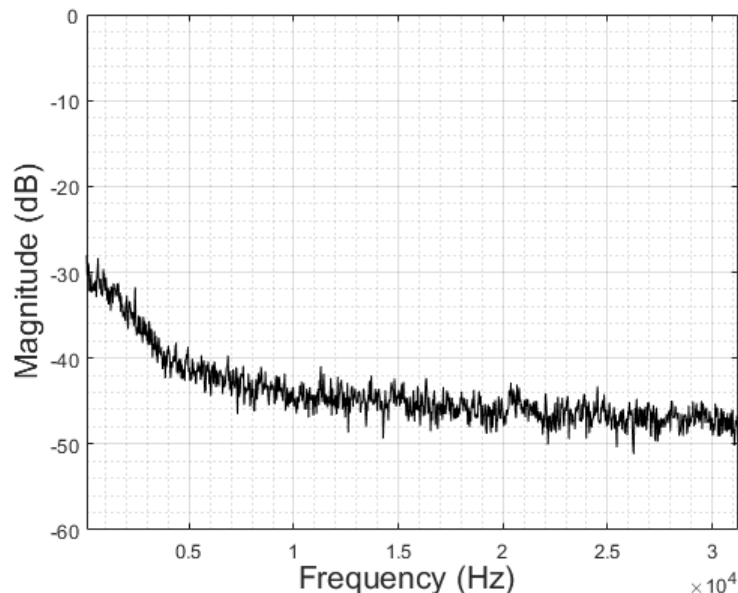


Figure B.1: Power spectral density of Shock oscillations upstream of H10 D17 cylinder

It can be seen that the resulting curve does not show any particular dominant frequencies and the PSD is spread out over the entire range of frequencies. Frequencies less than $5000 Hz$, are seen to exhibit higher power but the absence of any particular peak indicates quite a broad-

band nature of unsteadiness upstream of the roughness element. A similar result was also observed by [Estruch-Samper et al. \(2010\)](#) in their investigation upstream of a 3D protuberance in a Mach 8.2 Flow. Since a dominant frequency was not found, an approach involving the estimation of probability distribution of the upstream separation point was carried out (see Section 7.4) to investigate the upstream separation region and the inherent unsteadiness of the separation shock and hence the separation point.

